Spring 5-31-2011

Asymptotic and numerical analysis of time-dependent wave propagation in dispersive dielectric media that exhibit fractional relaxation

Matthew Frank Causley
New Jersey Institute of Technology

ABSTRACT

ASYMPTOTIC AND NUMERICAL ANALYSIS OF TIME-DEPENDENT WAVE PROPAGATION IN DISPERSIVE DIELECTRIC MEDIA THAT EXHIBIT FRACTIONAL RELAXATION

by
Matthew Frank Causley

This dissertation addresses electromagnetic pulse propagation through anomalously dispersive dielectric media. The Havriliak-Negami (H-N) and Cole-Cole (C-C) models capture the non-exponential nature of such dielectric relaxation phenomena, which is manifest in a variety of dispersive dielectric media. In the C-C model, the dielectric polarization is coupled to the time-dependent Maxwell's equations by a fractional differential equation involving the electric field. In the H-N case, a more general pseudo-fractional differential operator describes the polarization.

The development and analysis of a robust method for implementing such models is presented, with an emphasis on algorithmic efficiency. Separate numerical schemes are presented for C-C and H-N media. A straightforward numerical implementation of these models using finite-difference time-domain (FD-TD) techniques is expected to be second order accurate in both space and time. However due to the singular nature of the kernels appearing in the fractional convolution operators, the standard C-C implementation, produces first order accuracy in time. As we show, this method is equivalent to most approaches presented in the current literature, which implies that they are also first order. The desired accuracy is instead achieved by applying multistep methods to the fractional differential equation; however multistep methods are unnecessary in the H-N implementation to preserve the accuracy. Furthermore, the C-C model is a specific case of the H-N model and can therefore be constructed using the latter of these approaches.

The FD-TD methods are validated by evaluating the electric field for the signaling problem, using numerical quadrature to evaluate the integral form of the solution.

This is accomplished using the Green's function of the dispersive medium; in addition, the behavior of pulse propagation is studied asymptotically using the Green's function, which further validates the observed results of the numerical experiments.

ASYMPTOTIC AND NUMERICAL ANALYSIS OF TIME-DEPENDENT WAVE PROPAGATION IN DISPERSIVE DIELECTRIC MEDIA THAT EXHIBIT FRACTIONAL RELAXATION

by
Matthew Frank Causley

A Dissertation
Submitted to the Faculty of
New Jersey Institute of Technology and
Rutgers, The State University of New Jersey – Newark
in Partial Fulfillment of the Requirements for the Degree of
Doctor of Philosophy in Mathematical Sciences

Department of Mathematical Sciences, NJIT
Department of Mathematics and Computer Science, Rutgers-Newark

April 2011

APPROVAL PAGE

ASYMPTOTIC AND NUMERICAL ANALYSIS OF TIME-DEPENDENT WAVE PROPAGATION IN DISPERSIVE DIELECTRIC MEDIA THAT EXHIBIT FRACTIONAL RELAXATION

Matthew Frank Causley

Dr. Peter G. Petropoulos, Dissertation Advisor — Date
Associate Professor of Mathematical Sciences, New Jersey Institute of Technology

---

Dr. Gregory Kriegsmann, Committee Member — Date
Foundation Chair of Mathematical Sciences, New Jersey Institute of Technology

---

Dr. Jonathan Luke, Committee Member — Date
Professor and Associate Chairman of Mathematical Sciences, New Jersey Institute of Technology

---

Dr. Shidong Jiang, Committee Member — Date
Associate Professor of Mathematical Sciences, New Jersey Institute of Technology

---

Dr. Gerald Whitman, Committee Member — Date
Professor of Electrical and Computer Engineering, New Jersey Institute of Technology

BIOGRAPHICAL SKETCH

Author: Matthew Frank Causley

Degree: Doctor of Philosophy

Date: April 2011

Undergraduate and Graduate Education:

- Doctor of Philosophy in Mathematical Sciences,
  New Jersey Institute of Technology, Newark, NJ, 2011
- Bachelor of Science in Applied Mathematics,
  Kettering University, Flint, MI, 2006

Major: Mathematical Sciences

Presentations and Publications:

M. Causley, P. Petropoulos, S. Jiang, "Incorporating the Havriliak-Negami Dielectric Model in the FD-TD Method," *Journal of Computational Physics*, Vol 230, Number 10, 3884-3899, May 10 2011

M. Causley, P. Petropoulos, "On Numerically Solving the Cole-Cole Dielectric Model," *in progress*

G. Kepler et. al., "Cardiovascular events associated with oral and IV-administered antibacterial agents," workshop participation, *Fourteenth Industrial Mathematical and Statistical Modeling Workshop for Graduate Students*, Raleigh, NC, July 21-29, 2008.

M. Causley, P. Petropoulos, "A Numerical Method for Simulating EM Wave Propagation in Dielectrics that Exhibit Fractional Relaxation," Minisymposium, *SIAM Annual Conference*, Pittsburgh, PA, July 12-16 2010.

M. Causley, P. Petropoulos, "The Frequency-dependent Havriliak-Negami Dielectric Permittivity Model," Contributed Talk, *Frontiers in Applied and Computational Mathematics* (FACM 2010), Newark, NJ, May 21-23, 2010.

M. Causley, P. Petropoulos, "Stability and Error Analysis of the Cole-Cole Dielectric Model," Contributed Talk, *SIAM Annual Conference*, Denver, CO, July 6-10, 2009.

M. Causley, P. Petropoulos, "Numerical Analysis of the Havriliak-Negami Dielectric Model," poster presentation, *The Fifth Annual Graduate Student Research Day*, Newark, NJ, November 8, 2009.

M. Causley, P. Petropoulos, "Numerical Analysis of the Cole-Cole Dielectric Model," poster presentation, *Dana Know Research Showcase*, Newark, NJ, April 8, 2009.

I dedicate this work to my mother, and the loving memory of my father.

ACKNOWLEDGMENT

I would like to thank my advisor, Peter Petropoulos for the countless discussions in which he has given me invaluable insights, advice, and encouragement. As anybody who knows him could tell you, he is frank, and can be quite demanding; I have found these to be the attributes that have made him an excellent advisor. Peter is largely responsible for making me the researcher I am today. He encouraged me to continually improve myself, and passed along many anecdotes that made me both laugh, and contemplate my research more deeply. He not only asked me engaging and instructional questions, but he also instilled in me the discipline to find the answers. He is also wonderfully kind, and spared no effort in helping me find job opportunities, sending me to conferences, and doing everything in his power to ensure that I was prepared for my career after graduation.

I would like to thank Professor Kriegsmann for his helpful suggestions, which invariably led me to ask myself challenging questions that enriched my knowledge of mathematics and physics. Professor Kriegsmann is a very kind and approachable person, and I am very appreciative of all he has done for me.

Thank you to Professor Luke for instilling in me the mathematical rigor which has made me a better speaker, teacher, and mathematician. Professor Luke is one of the most giving faculty memebers in the Department of Mathematical Sciences, and I am grateful he was on my committee.

Thank you to Professor Jiang, for his helpful discussions on the fast solution of these fractional systems, and the method for obtaining quadratures. Professor Jiang's insight into numerical methods in modern mathematics has been very influential on my research interests, and I have found discussions with him to be illuminating.

Thank you to Professor Whitman for his stimulating questions regarding the application of mathematics to electrical engineering. These questions served as a

reminder that my work will only be valuable to others if I can explain it clearly in tractable language.

In addition to my committee, I would like to acknowledge the many graduate students at NJIT, with whom I have shared many wonderful, difficult and ultimately memorable experiences. In particular, I would like to thank Matt Malej, Jacek Wrobel, Dan Cargill, Daniel Fong, Jeff Pohlmeyer, Te-Sheng Lin, Brian Emmanuel, Oleksiy Varfolomiyev, Rashi Jain, and certainly Hetal Kapadia for their help, support and encouragement over the past 5 years.

I must also acknowledge Dr. Brian McCartin for his invaluable mentoring during my undergraduate career, and for encouraging me to pursue my doctoral degree at NJIT.

Having saved the best for last, I would like to thank my dearest love, Anjulie Tacey for all of the loving and supporting things, both small and large, that she has done to sustain me over the past 5 years. This includes the little things, like letting me read my thesis to her until she peacefully drifted off to sleep; and the big things, like being a wonderful cook and "forcing" me to partake in her delicious meals.

TABLE OF CONTENTS

TABLE OF CONTENTS
(Continued)

Chapter **Page**

LIST OF TABLES

Table **Page**

LIST OF FIGURES

LIST OF FIGURES
(Continued)

Figure **Page**

LIST OF FIGURES
(Continued)

Figure **Page**

LIST OF FIGURES
(Continued)

Figure **Page**

LIST OF FIGURES
(Continued)

Figure **Page**

CHAPTER 1

INTRODUCTION

The study of dielectric relaxation in materials has been the subject of theoretical and applied investigations for more than a century. The pioneering work of Debye [9] in this field has been expanded by Cole and Cole [6], Davidson and Cole [8], and Havriliak and Negami [17], to produce a hierarchical class of empirical dielectric models. The latter of these is given in the frequency domain by

$$\hat{\epsilon}(\omega) = \epsilon_\infty + \frac{\epsilon_s - \epsilon_\infty}{(1 + (i\omega\tau)^\alpha)^\beta}. \tag{1.1}$$

The Havriliak-Negami (H-N) model consists of five parameters, which describe the frequency-dependent nature of dielectric relaxation. The static or DC limit $\hat{\epsilon}(0) = \epsilon_s$, and the infinite-frequency limit $\hat{\epsilon}(\infty) = \epsilon_\infty$ of the permittivity satisfy $\epsilon_s > \epsilon_\infty \geq 1$. The transition region between these values occurs in the frequency domain, and is centered at $\omega_\tau = 1/\tau$; hence τ is the central relaxation time. The remaining fractional parameters α and β satisfy $0 < \alpha, \beta \leq 1$, and stretch the duration of the relaxation process.

The Debye model [9] is obtained by setting $\alpha = \beta = 1$ in (1.1), and corresponds to classical, or exponential dielectric relaxation. Whenever at least one of these parameters α and β is not unity, the behavior will be non-exponential, or anomalous. The important limiting cases are given by the Cole-Cole [6] ($0 < \alpha < 1, \beta = 1$) and Cole-Davidson [8] ($0 < \beta < 1, \alpha = 1$) models. Collectively these empirical models have been used to describe a host of complex heterogeneous materials when subjected to electric fields over a range of frequencies.

The H-N model constitutes a causal dielectric model for complex frequency $s = i\omega$, when the branch $-\pi < \arg s \leq \pi$ is taken. The H-N and related models are

empirical, in that the parameter values are obtained by fitting to data that is collected over several decades of frequencies. A fairly recent work by Kalmykov et. al [21] has offered a means to derive the H-N model from first principles. Their explanation considers the complex microstructure of spatially heterogeneous dielectrics. They have shown that the H-N model arises naturally by assuming that a collection of electrically noninteracting dipoles will be governed by Brownian motion, which rotate according to a fractal time random walk. This is an extension of Debye's original work, which assumed a discrete time random walk, and led to exponential relaxation. The only shortcoming of their approach is the lack of physical interpretation of the parameter β above; the parameter α is explained by the fractal dimension of the random walk that is assumed. Nevertheless, Kalmykov's analysis lends credence to many experimental observations (e.g., [1], [5], [13], [19], [24]), which indicate that anomalous relaxation is produced by the superposition of various relaxation processes that occur during overlapping time scales.

The development of broadband dielectric spectroscopy has made it possible to interrogate and characterize the complex permittivity of dielectric materials over a large range of frequencies (typically in the MHz to GHz range). As a result, the H-N and related models have been demonstrated to accurately describe the observed permittivity of various materials, over broadband frequency regimes. While typical H-N materials consist mostly of glassy materials [1], and amorphous polymers near the glass-liquid transition [13] phase, the Cole-Cole (C-C) model has been used in the characterization of soils [32], and even biological tissues [12]. In particular, Gabriel et. al to made extensive use of the C-C model in [12] to construct broadband approximations for the permittivity of many biological tissues. The Cole-Davidson (C-D) model has similarly been used to make exceptionally accurate fits to doped silicon [19]. Additionally, multi-pole Debye models have been used to describe aqueous and non-aqueous electrolyte solutions [5], [24].

Figure 1.1 Dielectric Spectrometer with high and low-frequency attachments. Source: Institute of Solid State Research

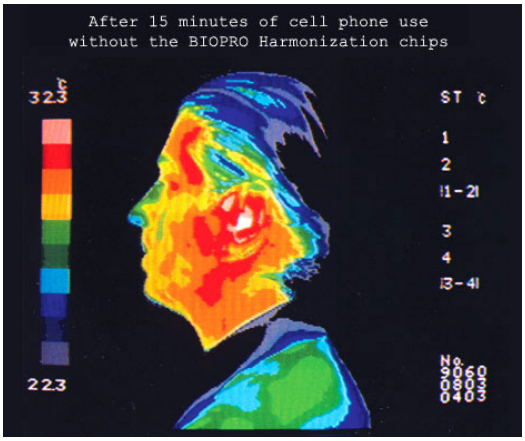

Figure 1.2 Thermal imaging of the human head showing the effects of electromagnetic radiation due to cell phone usage. Source: ewg.org

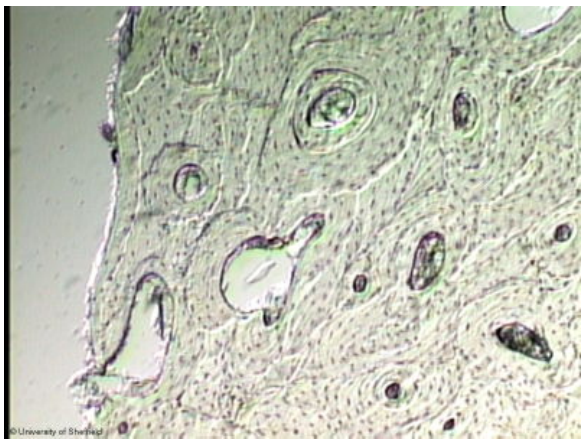

Figure 1.3 Microstructure of complex biological tissues, which obey the Cole-Cole dielectric model. Source: University of Sheffield Archaeology

The simulation of electric pulse propagation through such materials is therefore of great use in a variety of technological applications. The H-N and C-D models could be used in the study and development of semiconductor components. Similarly, simulation of propagation through C-C materials play a key role in the discovery of oil in heterogeneous soils [32]. Perhaps most importantly though is the ability of the C-C model to increase our understanding of the transient nature of electromagnetic radiation in the human body [7], [23] [12]. Recent developments have made possible the generation of fast rise-time electric pulses which contain ultrawideband (UWB) spectra and low power densities, which make them safe for human exposure. This has made millimeter wave technologies a feasible alternative to various older technologies, including X-ray, radar and other related imaging techniques. This alone makes the need for simulations of pulse propagation in dispersive dielectric media imminent.

In the ensuing chapters, we will consider for simplicity a model problem, which consists of a source-free medium contained in a half-space $x > 0$, whose dielectric permittivity is given by equation (1.1), and whose magnetic permeability is that of free space, $\mu = \mu_0$. In the absence of surface charges, the time-dependent Maxwell's equations are then given as

$$\frac{\partial \mathbf{B}}{\partial t} = -\nabla \times \mathbf{E} \tag{1.2}$$

$$\frac{\partial \mathbf{D}}{\partial t} = \nabla \times \mathbf{H}, \tag{1.3}$$

where the magnetic flux vector is given in terms of the magnetic field by the constitutive relation $\mathbf{B} = \mu_0 \mathbf{H}$, and the electric displacement vector will be similarly defined in the frequency domain as

$$\hat{\mathbf{D}}(\mathbf{x}, \omega) = \epsilon_0 \hat{\epsilon}(\omega) \hat{\mathbf{E}}(\mathbf{x}, \omega). \tag{1.4}$$

We will follow the convention of defining the the permittivity in terms of the complex susceptibility, and the displacement vector in terms of an induced polarization field;

thus

$$\mathbf{D} = \epsilon_0 \epsilon_\infty \mathbf{E} + \mathbf{P} \tag{1.5}$$

where

$$\mathbf{P}(\mathbf{x}, t) = \epsilon_0 \int_{-\infty}^{t} \chi(t - t') \mathbf{E}(\mathbf{x}, t') dt', \tag{1.6}$$

and where the dielectric susceptibility $\chi(t)$ is given as

$$\chi(t) = \mathcal{L}^{-1} \left\{ \frac{\epsilon_s - \epsilon_\infty}{(1 + (s\tau)^\alpha)^\beta} \right\}, \tag{1.7}$$

where $\mathcal{L}^{-1}\{\cdot\}$ is the inverse Laplace transform, and $s = i\omega$ is the complex frequency. Without loss of generality, we will assume that all fields are zero for $t \leq 0$. At this time, the medium is excited by a normally incident incoming electric pulse at the air-medium interface, $x = 0$. The resulting plane wave geometry reduces the magnetic and electric field vectors to scalar field quantities $\mathbf{H} = H_y \hat{\mathbf{y}}$ $E = \mathbf{E}_z \hat{\mathbf{z}}$ which are uniform in the y and z directions. Thus, the reduced Maxwell system is comprised of the coupled scalar equations

$$\frac{\partial}{\partial t} (\mu_0 H) = \frac{\partial E}{\partial x}, \tag{1.8}$$

$$\frac{\partial}{\partial t} (\epsilon_0 \epsilon_\infty E + P) = \frac{\partial H}{\partial x}, \tag{1.9}$$

$$E(0, t) = f(t), \quad t > 0. \tag{1.10}$$

The polarization field $\mathbf{P} = P_z \hat{\mathbf{z}}$ is similarly expressed by equation (1.6) in a suitably scalar form.

In Chapter 2, we will solve this model problem with signaling data to study pulse propagation through H-N (and related) dielectrics. As part of this discussion, we will develop a means to obtain the electric field using the inverse Laplace transform, which will be used to validate the finite difference computations. Additionally, we will also

explore the nature of the impulse response at the wave front in an H-N material, using asymptotic approximations for short and large depths.

Dielectric permittivity models are typically implemented using the finite-difference time-domain (FD-TD) [35]. In the case of the Cole-Cole model, one approach is to determine P through an auxiliary fractional differential equation that is forced by the electric field,

$$D_t^\alpha P + P = \epsilon_0(\epsilon_s - \epsilon_\infty)E, \tag{1.11}$$

where D_t^α is the fractional time derivative of order α. Previous works have used auxiliary (ordinary) differential equations for the Debye [26] and Cole-Cole [16] dielectric models. In Chapter 3, we will address the numerical evaluation of fractional derivatives and fractional differential equations, and the FD-TD implementation of the Cole-Cole dielectric model.

In the case of the H-N model, this fractional differential equation is formally a fractional pseudo-differential operator

$$(\tau^\alpha D_t^\alpha + 1)^\beta P = \epsilon_0(\epsilon_s - \epsilon_\infty)E, \tag{1.12}$$

which cannot be incorporated into the FD-TD method in a straightforward manner. An alternative approach, which we develop in Chapter 4, is to incorporate the H-N dielectric model into Ampere's Law by determining the polarization field P via convolution in time of the electric field (1.6) and the time-domain susceptibility $\chi(t)$ (1.7). A straightforward implementation of this convolution is computationally prohibitive due to the non-exponential nature of $\chi(t)$, which is singular at $t = 0^+$ and decays algebraically for $t > 0$. While we will develop this approach in the FD-TD setting, the methods are general, and can be applied to any computational electromagnetics code that solves the time-domain Maxwell system in its differential

form. This latter approach also possesses the advantage that the C-C and C-D models can be treated, with no additional augmentations required.

In each of Chapters 3 and 4, we provide a detailed analysis of the convergence of the numerical schemes, where great care is taken to preserve the second order accuracy in space and time that is inherited from the FD-TD scheme. The stability and phase error of the numerical solutions is also analyzed in each case.

CHAPTER 2

THE MODEL PROBLEM AND ITS ASYMPTOTIC ANALYSIS

2.1 Analytical Solution

The electric field for a given incident pulse $f(t)$ can be obtained in terms of the Green's function for the H-N medium. We first combine the first order system of PDEs (1.8) into a single second order equation, by cross differentiation and elimination of the magnetic field

$$\frac{\partial^2}{\partial t^2}\left(\epsilon_0\epsilon_\infty E + P\right) = \frac{1}{\mu_0}\frac{\partial^2}{\partial x^2}E, \quad x > 0, \quad t > 0, \tag{2.1}$$

$$E(0,t) = f(t), \quad t > 0, \tag{2.2}$$

where the polarization is still given in terms of the electric field by (1.6). Elimination of P is then possible by taking the Laplace transform of equation (1.6), so that $\hat{P}(x,s) = \chi(s)\hat{E}(x,s)$, where $\hat{E}(x,s) = \mathcal{L}\{E\}$ denotes the Laplace transform, and $s = i\omega$ is the frequency. Thus

$$\left(\frac{s}{c(s)}\right)^2 \hat{E} = \frac{\partial^2 \hat{E}}{\partial x^2}, \quad x > 0 \tag{2.3}$$

$$\hat{E}(0,s) = F(s), \tag{2.4}$$

where

$$\frac{1}{c(s)} = \sqrt{\mu_0\epsilon_0\left(\epsilon_\infty + \frac{\epsilon_s - \epsilon_\infty}{(1+(s\tau)^\alpha)^\beta}\right)}. \tag{2.5}$$

The associated Green's function $\Psi(x,t)$ is obtained by solving the above problem, with $F(s) = 1$ and imposing the condition that $\hat{\Psi}(x,s)$ remain bounded as $x \to \infty$, which yields

$$\hat{\Psi}(x,s) = e^{-sx/c(s)}. \tag{2.6}$$

This will thus be the impulse response for an H-N medium, and so the electric field resulting from an incident pulse $f(t)$ will be given as

$$\begin{aligned} E(x,t) &= \mathcal{L}^{-1}\left\{F(s)\hat{\Psi}(x,s)\right\} \\ &= \frac{1}{2\pi i}\int_{\zeta-i\infty}^{\zeta+i\infty}\left[F(s)e^{-\frac{sx}{c_\infty}q(s\tau)}\right]e^{st}ds, \quad t \geq \frac{x}{c_\infty} \end{aligned} \tag{2.7}$$

where $c_\infty = 1/\sqrt{\mu_0\epsilon_0\epsilon_\infty}$, $F(s) = \mathcal{L}\{f(t)\}$, and $q = c_\infty/c(s)$ is a scaled expression of the frequency-dependent inverse wave speed

$$q(s\tau) = \sqrt{1 + \frac{r-1}{(1+(s\tau)^\alpha)^\beta}}, \quad r = \frac{\epsilon_s}{\epsilon_\infty}. \tag{2.8}$$

When $F(s) = 1$, equation (2.7) will produce the time domain representation of the impulse response $\Psi(x,t)$. Equation (2.7) can be studied asymptotically, as well as approximated numerically using a suitably deformed Bromwich contour in the complex s domain. The region of analyticity of $\hat{\Psi}$ will be independent of α and β. In particular, the square root introduced by equation (2.8) produces a branch cut along the negative real axis, and so the region of analyticity will be s for which $-\pi < \arg s < \pi$. Thus, we can deform the Bromwich contour to be any curve that begins at $s = \infty$ in the third quadrant, passes to the right of the singularities of F, and terminates at $s = \infty$ in the second quadrant. Once a suitable contour is chosen, we construct the N quadrature points (w_k, s_k), where each s_k is on the contour; we then apply the mapping $s = z/t$, so that the impulse response is approximated as

$$\Psi(x,t) \approx \sum_{k=1}^{N}\frac{w_k}{t}\exp\left(\frac{s_k}{t}\left[t - \frac{x}{c_\infty}q(s_k\tau/t)\right]\right). \tag{2.9}$$

If $F(s)$ is known, then E can be computed directly with this method, by replacing w_k with $w_k F(s_k/t)$. Otherwise, we can obtain $\Psi(x,t)$, and convolve in the time domain with the pulse $f(t)$. Of course, the choice of the contour will determine the accuracy of the approximation, and will determine the number of points N required to obtain

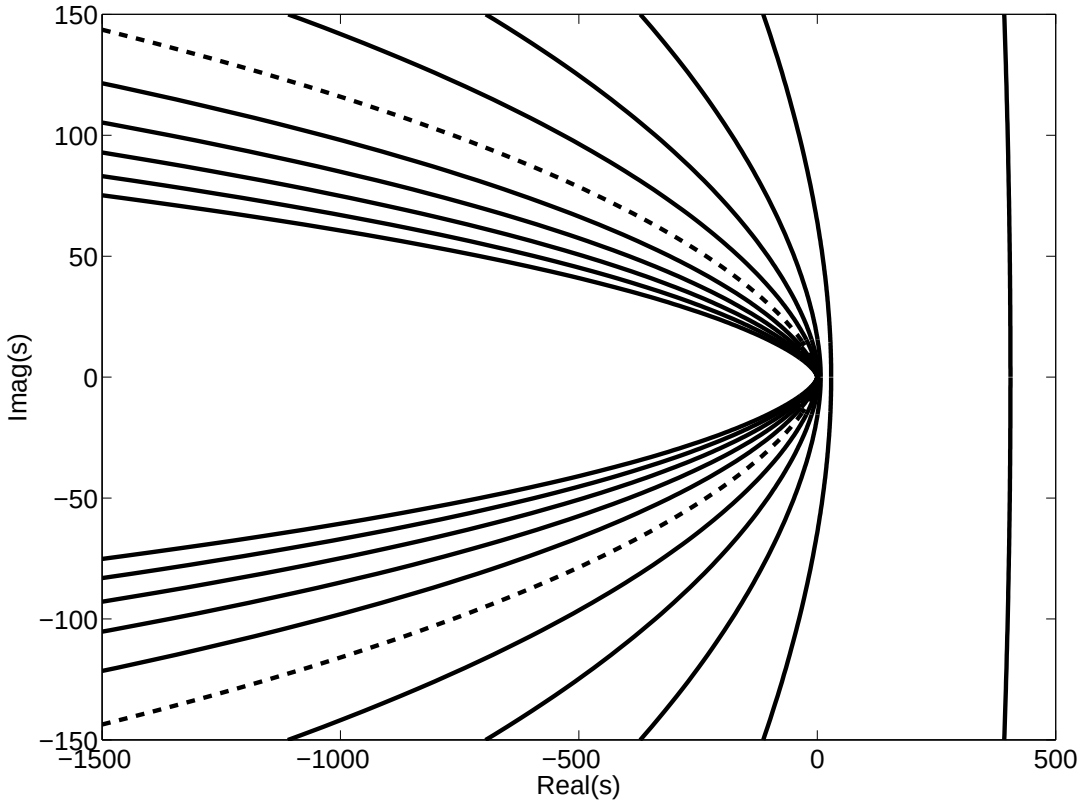

Figure 2.1 Numerically determined steepest descent contours for the H-N impulse response. The contour moves to the left as the parameter $\theta = \frac{c_\infty t}{x}$ increases, and the saddle point moves into the origin when $\theta = \frac{c_\infty}{c_s}$ (dotted line). For $\theta > \frac{c_\infty}{c_s}$, the contour forms a cusp at the origin.

a desired accuracy. Ideally a steepest descent contour would be determined, which will pass through a saddle point, and along which the imaginary part of the phase $\phi = s\left[t - \frac{x}{c_\infty} q(s\tau)\right]$ is constant. The saddle point satisfies $d\phi/ds = 0$, which yields the expression

$$\begin{aligned}
\theta &= q(s\tau) + s\tau q'(s\tau) \\
&= \frac{1}{q(s\tau)} \left((q(s\tau))^2 - \frac{\alpha\beta(s\tau)^\alpha}{2(1+(s\tau)^\alpha)} ((q(s\tau))^2 - 1) \right) \\
&= \frac{1}{\sqrt{1 + \frac{r-1}{(1+(s\tau)^\alpha)^\beta}}} \left(1 + \frac{r-1}{(1+(s\tau)^\alpha)^\beta} - \frac{\alpha\beta(r-1)(s\tau)^\alpha}{2(1+(s\tau)^\alpha)^{\beta+1}} \right)
\end{aligned} \tag{2.10}$$

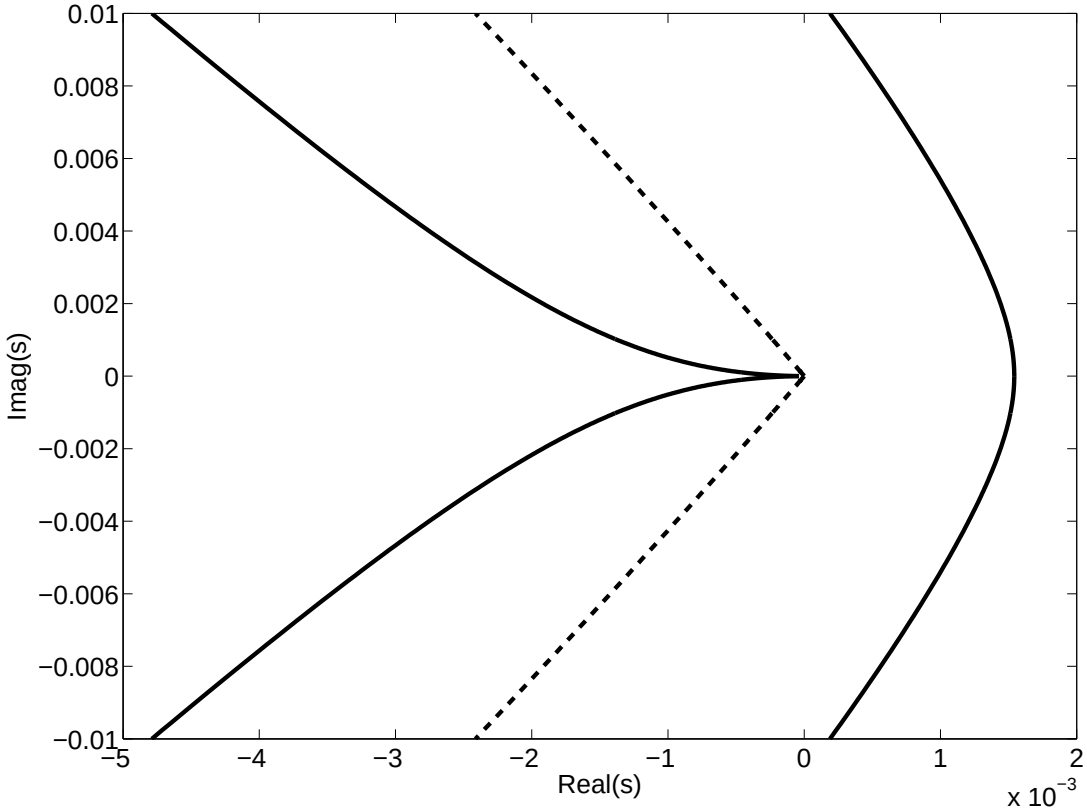

Figure 2.2 Behavior of the contour near the origin. The behavior of the contours for $\theta > \frac{c_s t}{x}, \theta = \frac{c_s t}{x}$ and $\theta < \frac{c_s t}{x}$ are shown.

where $\theta = \frac{c_\infty t}{x}$; note that the saddle point does not depend on x and t individually, but only on their ratio. In addition, due to causality, we restrict ourselves to $\theta \geq 1$, which corresponds to the characteristic ray $t = x/c_\infty$. Unfortunately, this unwieldy expression is a nonlinear equation, that can be rationalized into a polynomial (of degree 4) in s^α only when $\beta = 1$; otherwise the equation is transcendental. Instead of seeking a closed form solution, we find real s that satisfies this expression using Newton's method. In terms of the parameter θ, the saddle point moves along the real line, decreasing from $s(1) = \infty$, to $s(\theta^*) = 0$, where $\theta^* = \sqrt{r} = \frac{c_\infty}{c_s}$ corresponds to the subcharacteristic ray $t = x/c_s$. For $t > x/c_s$, no real-valued saddle point will exist, and the steepest descent contour will develop a cusp at the origin. This is illustrated

in Figures 2.1 and 2.2 for the H-N model with a representative set of parameters, with x fixed, and increasing θ. When the saddle point exists, the contour passes through it vertically ($\arg s = \pm\frac{\pi}{2}$). Although Figure 2.1 is useful to examine, it falls short of providing a parametric representation of the equation from which s (and thus, ds) can be obtained explicitly. This approach will become more useful in the asymptotic estimates for the impulse response below. Instead, we proceed in evaluating $\Psi(x,t)$ by choosing a hyperbolic contour, as used in [38] to perform numerical inverse Laplace transforms. This contour is given by

$$s(u) = \mu\left(1 + \sin\left(iu - a\right)\right), \quad -\infty < u < \infty, \tag{2.11}$$

and provides a means to construct the weights and nodes (w_k, s_k). Specifically, we set

$$s_k = \mu\left(1 + \sin\left(iu_k - a\right)\right), \quad w_k = \frac{\mu}{2\pi}\cos\left(iu_k - a\right), \quad -\frac{N}{2} \le k \le \frac{N}{2} \tag{2.12}$$

where $u_k = kh$, with an appropriate step size h. As shown in [38], selection of the parameters h, μ and a can be made by asymptotic balancing of the error terms. There will be two sources of error in the approximation: the truncation error, which arises when the infinite limits $-\infty < u < \infty$ are truncated to $-Nh < u < Nh$; and the discretization error, or quadrature error due to approximation of the integral with a finite sum.

This construction of the impulse response $\Psi(x,t)$ will be shown below to validate the asymptotic behavior of the wavefront at short and large depths, and in Chapters 3 and 4 to validate the FD-TD solutions of the electric field. Solutions obtained using this hyperbolic contour are further validated by computing the impulse response independently. The alternative method follows from folding the Bromwich curve on the branch cut, $s = ue^{\pm\pi i}$, $0 < u < \infty$. The integral is discretized in this case with

Gauss-Legendre quadrature, with an excessively large number of nodes (3 to 4 times as many as those used in the hyperbolic contour) to ensure sufficient convergence.

It is noteworthy that such computations can be performed at a given (x, t) location, $t \geq x/c_\infty$, independently with no information required at neighboring locations. This is in stark contrast to time-stepping schemes, in which the electric field can only be obtained at time level $t_n = n\Delta t$ after all previous time levels have been computed. Unfortunately, it is not clear a priori what choice of N is required to ensure convergence to within a given precision, which is one of the drawbacks to this method. For a value of N that is too large, evaluation of the impulse response over many values of (x, t) will be time-consuming. Additionally, we have found in practice that it is helpful to scale the quadrature nodes by either time $s = z/t$, or by the delayed time $s = z/(t - t_\infty)$, where $t_\infty = x/c_\infty$ is the arrival time of the wavefront. The correct choice of both N and the method of scaling is determined by the size of x, and the range of time over which the solution is to be computed.

2.2 Asymptotic Behavior

We now present an asymptotic investigation of the electric field (2.7) at the wavefront for both short and large depths into the H-N medium. The results will be presented for the general (H-N) case, but are also valid for the limiting cases of the Cole-Cole and Cole-Davidson models.

2.2.1 Short-depth Behavior

We will first ascertain the nature of the wavefront after a short depth into the H-N medium, which is characterized by $t \approx x/c_\infty \ll \tau$, where $x = O(c_\infty \tau)$ is referred to as the time-domain skin depth [33]. We will also refer to this asymptotic regime in terms of $\theta = c_\infty t/x$, which satisfies $\theta \approx 1$ near the wavefront. If in equation (2.7) we substitute $s = z/t$, and assume $t \ll \tau$, we see that the phase of the wavefront

behavior will be determined by the infinite-frequency approximation for $q(s\tau)$, which is given by retaining the first term of the expansion of (2.8) for large $s\tau$, as

$$q(s\tau) \approx 1 + \frac{r-1}{2}(s\tau)^{-\alpha\beta} + O\left((s\tau)^{-\alpha(\beta+1)}\right), \quad (s\tau) \gg 1. \tag{2.13}$$

This approximation is inserted into equation (2.7), and upon setting $F(s) = 1$ we obtain the leading order behavior of the impulse response at the wavefront

$$\Psi(x,t) \approx \Psi_\infty(x,t) = \frac{1}{2\pi i}\int_{\zeta-i\infty}^{\zeta+i\infty} e^{s\left(t-\frac{x}{c_\infty}\right)} e^{-Ax(s\tau)^{1-\alpha\beta}} ds, \tag{2.14}$$

with $A = \frac{(r-1)}{2c_\infty \tau}$. The representation shown has been deliberately written in a factored form, to distinguish between two prominent features of the early impulse response. The argument of the first exponential factor is a hyperbolic term, which shows that the wavefront will propagate with the infinite frequency speed c_∞. The additional exponential factor will act as a smoothing operator on the incoming pulse. Notice that the parameters α and β only appear as a product $\alpha\beta$ in this approximation; thus the behavior of the electric field in the skin depth cannot be discerned as that of a Cole-Cole, Cole-Davidson, or Havriliak-Negami medium.

To elaborate on the smoothing effects of the early impulse response, we compute the early wavefront response for the electric field due to an incident pulse $f(t)$ by first defining an effective pulse $g(x,t)$, which in the Laplace domain is given as

$$G(x,s) = F(s)e^{-Axs^{1-\alpha\beta}}. \tag{2.15}$$

Now, since $\mathcal{L}^{-1}\left\{\exp -sx/c_\infty\right\} = \delta(t - x/c_\infty)$, we see that the short depth electric field satisfies $E(x,t) \approx g(x, t - x/c_\infty)$. Furthermore, differentiation of (2.15) with respect to x shows shows that $G_x + As^{1-\alpha\beta}G = 0$, so that $g(x,t)$ satisfies a fractional-order wave equation

$$AD_t^{1-\alpha\beta} g + g_x = 0, \quad x > 0, \quad t > 0, \tag{2.16}$$

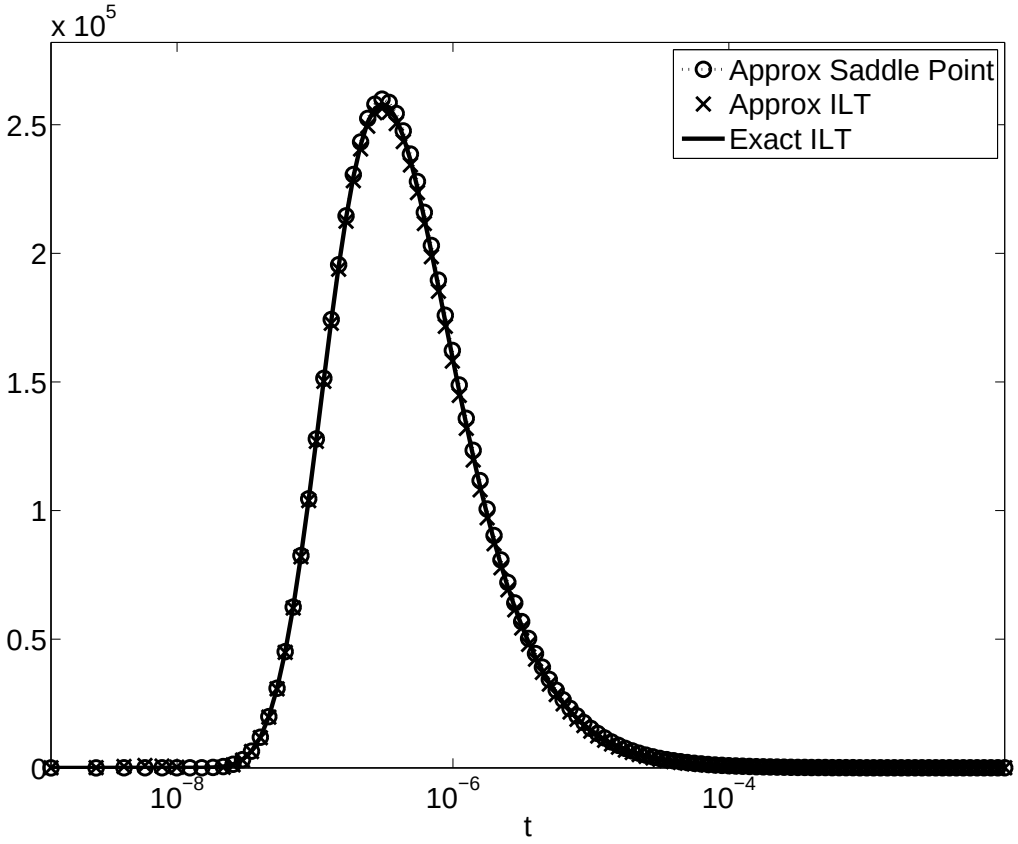

Figure 2.3 Validation of the infinite-frequency approximation of the Havriliak-Negami impulse response, at $x = 0.0002 c_\infty \tau$ and $\alpha = 0.6$. The time is translated, so that the origin is at $t = \frac{x}{c_\infty}$.

with boundary condition $g(0,t) = f(t)$. A precise definition of the fractional derivative $D_t^{1-\alpha\beta} g$ is deferred to Chapter 3. The effective pulse $g(x,t)$ will be infinitely smooth for $\alpha\beta < 1$, as can be seen by

$$\lim_{t\to 0} \frac{\partial^n g}{\partial t^n} = \lim_{s\to+\infty} s^{n+1} G(x,s) = \lim_{s\to+\infty} F(s) e^{-Axs^{1-\alpha\beta}} = 0, \quad n > 0. \tag{2.17}$$

This result was shown in [30] to hold for the C-C model, and now can be seen to generalize to the H-N model. In the limit $\alpha\beta \to 1$, the behavior in a Debye medium is recovered, and the solution to (2.16) will be $g(x,t) = f(t)e^{-Ax}$ (hence, $E(x,t) \approx f(t - x/c_\infty)e^{-Ax}$), which shows $E(x,t)$ will not be infinitely smooth, but will instead inherit any discontinuities in the signal $f(t)$.

In contrast to the exact impulse response, the short-depth approximation Ψ_∞ can be successfully computed using the method of steepest descents. This is due to the simpler expression for the phase, which can be used to obtain a closed form representation of the contour. The saddle point is obtained by setting $d\phi/ds = 0$, where $\phi = s(t - x/c_\infty) - Ax(s\tau)^{1-\alpha\beta}$ is the phase of equation (2.14). This results in

$$s^* = \frac{1}{\tau}\left(\frac{(1-\alpha\beta)Ax}{t - x/c_\infty}\right)^{\frac{1}{\alpha\beta}} = \frac{1}{\tau}\left(\frac{r-1}{2}\frac{(1-\alpha\beta)}{\theta - 1}\right)^{\frac{1}{\alpha\beta}} \tag{2.18}$$

Notice that we have a moving saddle point, as it is inversely proportional to $(\theta - 1)$; thus we first make the change of variables $s\tau = z\lambda$ in equation (2.14), where $\lambda = (\theta - 1)^{-1/\alpha\beta}$ will be a large positive parameter (recall that $\theta = c_\infty t/x \approx 1$ at the wavefront). This will ensure that the main contribution of the integral will remain localized near the saddle point, which is now given as $z^* = ((1-\alpha\beta)(r-1)/2)^{\frac{1}{\alpha\beta}}$ and is now stationary. Making this change of variables in equation (2.14) produces

$$\Psi_\infty(x,t) = \frac{\lambda}{2\pi i\tau}\int_{\zeta-i\infty}^{\zeta+i\infty} \exp\left[\lambda\left(\frac{t}{\tau} - \frac{x}{c_\infty\tau}\right)\left(z - \frac{r-1}{2}z^{1-\alpha\beta}\right)\right]dz. \tag{2.19}$$

After substituting the second order approximation of the phase about $z = z^*$,

$$\phi \approx \lambda\left(\frac{t}{\tau} - \frac{x}{c_\infty\tau}\right)\left(-\frac{\alpha\beta}{1-\alpha\beta}z^* + \frac{\alpha\beta}{2z^*}(z - z^*)^2\right) + O\left((z-z^*)^3\right) \tag{2.20}$$

we integrate the resulting expression to obtain the leading order term of the asymptotic series

$$\Psi_\infty \approx \frac{1}{\tau}\sqrt{\frac{z^*\lambda c_\infty\tau}{2\pi\alpha\beta(c_\infty t - x)}}\, e^{-\frac{\alpha\beta}{1-\alpha\beta}z^*\lambda(t-\frac{x}{c_\infty})}\left(1 + O\left(\frac{1}{\lambda}\right)\right). \tag{2.21}$$

Figures 2.3 and 2.4 show the saddle point approximation for $x = 0.0002c_\infty\tau, r = 75$, and $\alpha\beta = 0.6, 0.8$ respectively, compared to the exact impulse response, obtained using the hyperbolic Bromwich contour (2.11). We also show the result of directly evaluating (2.14) along the steepest descent contour, which is detailed below. Note

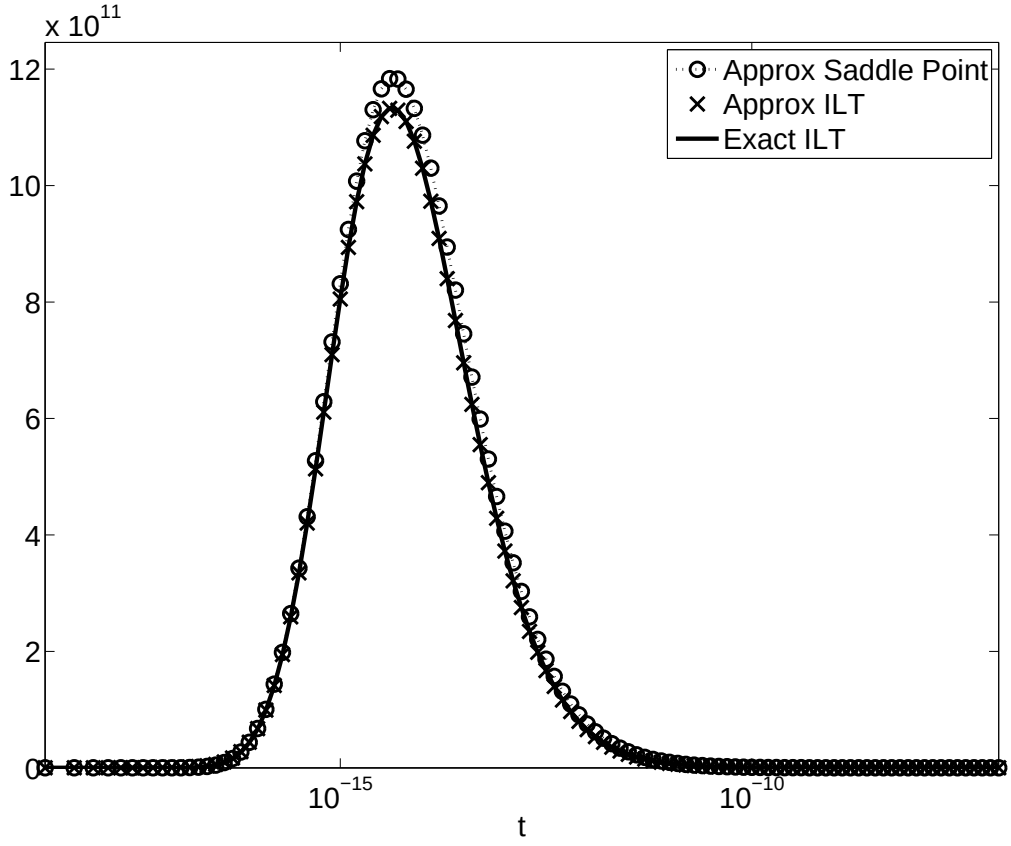

Figure 2.4 Validation of the infinite-frequency approximation of the Havriliak-Negami impulse response, at $x = 0.0002 c_\infty \tau$ and $\alpha = 0.8$. The time is translated, so that the origin is at $t = \frac{x}{c_\infty}$.

that the relative amplitude of the impulse response is heavily dependent upon $\alpha\beta$, and approaches infinity for $\alpha\beta = 1$; this reflects the fact that for the Debye response, $\Psi_\infty = \delta(t - x/c_\infty)e^{-Ax}$. Additionally, note that the approximations show better agreement with the exact response for smaller $\alpha\beta$; this is because λ will be larger for smaller $\alpha\beta$, which makes the saddle point approximation (2.21) converge more rapidly.

In order to directly evaluate the approximate impulse response as in Figures 2.3 and 2.4, we first find a parametric representation of the steepest descent contour. This is most easily accomplished in polar form. We first define $s\tau = \rho e^{i\sigma}$, and then note from equation (2.18) that both s^* and $\phi(s^*)$ will be real, so that the steepest

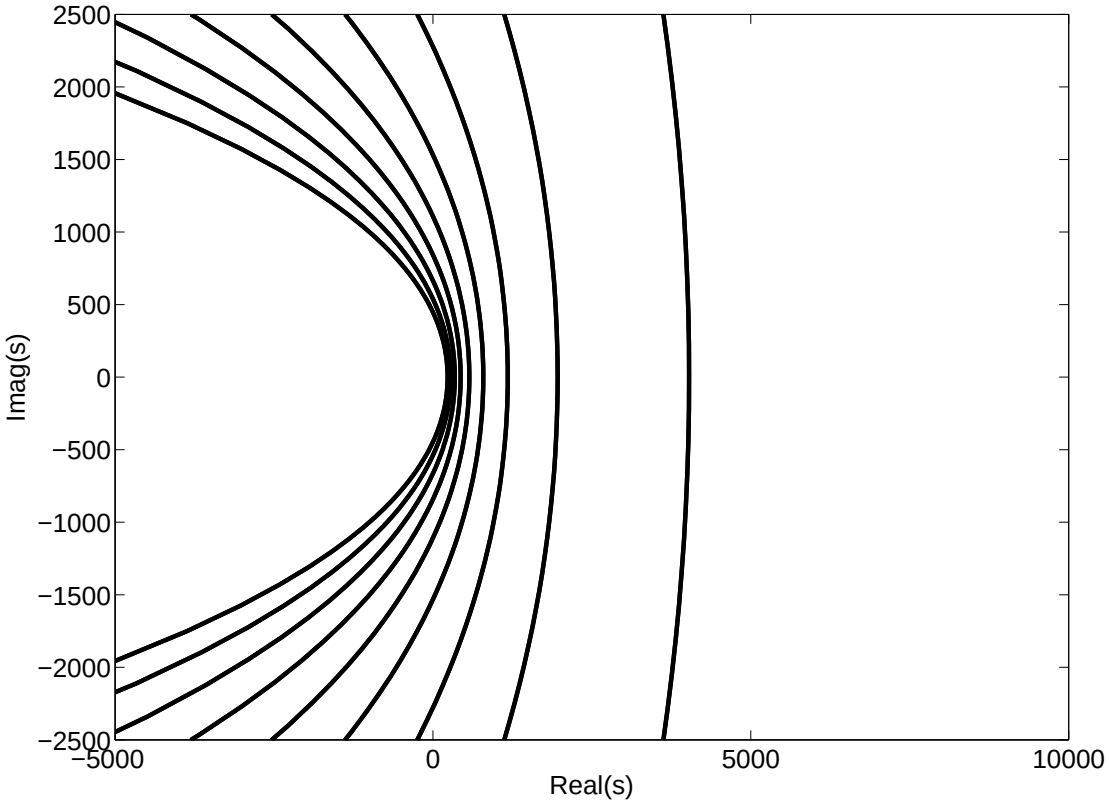

Figure 2.5 Steepest descent contour for the phase of the short-depth approximation of the H-N impulse response (2.14). Contours are shown for $1 < \theta \leq 3$, since the asymptotic regime corresponds to $\theta \approx 1$.

descent contour satisfies $\Im[\phi] = 0$. This will lead to the following expression

$$\rho(\sigma) = s^* \left[\frac{\sin\left((1-\alpha\beta)\sigma\right)}{(1-\alpha\beta)\sin\sigma} \right]^{\frac{1}{\alpha\beta}}, \quad -\pi < \sigma < \pi. \tag{2.22}$$

For the sake of simplicity, we define the function

$$S(\sigma; a, b) = \frac{b \sin(a\sigma)}{a \sin b\sigma}, \quad S(0; a, b) = 1 \tag{2.23}$$

so that $\rho(\sigma) = s^* S(\sigma; 1-\alpha\beta, 1)^{1/\alpha\beta}$, and $\rho(0) = s^*$. This contour is shown in Figure 2.5 for comparison to Figure 2.1. The contours are only of interest for $\theta \approx 1$, since this is where the approximation (2.14) is asymptotically valid. Using the parametric representation and the expression (2.23), the short-depth approximation

of the impulse response takes the form

$$\Psi_\infty = \frac{1}{2\pi\tau}\int_{-\pi}^{\pi} \exp\left[-\left(\frac{t}{\tau}-\frac{x}{c_\infty\tau}\right)\rho(\sigma)\alpha\beta S(\sigma;\alpha\beta,1)\right]\rho(\sigma)S(\sigma;\alpha\beta,1-\alpha\beta)d\sigma. \tag{2.24}$$

Approximation of this integral can be accomplished using the trapezoidal rule, which yields exponential convergence,

$$\Psi_\infty = \frac{1}{2(N+1)\tau}\sum_{k=-N}^{N} \exp-\left[\left(\frac{t}{\tau}-\frac{x}{c_\infty\tau}\right)\rho(\sigma_k)\alpha\beta S(\sigma_k;\alpha\beta,1)\right]\rho(\sigma_k)S(\sigma_k;\alpha\beta,1-\alpha\beta), \tag{2.25}$$

where $\sigma_k = \frac{k\pi}{N+1}$.

2.2.2 Large-depth Behavior

We now examine the behavior of the wave front for depths satisfying $x \gg c_\infty\tau$. In this region, we will take $t \approx x/c_s \gg \tau$, or alternatively $\theta \approx c_\infty/c_s$. This regime will correspond to the $s = 0$ limit of (2.8); thus

$$q(s\tau) \approx \sqrt{r}\left(1-\beta\frac{r-1}{2r}(s\tau)^\alpha\right) + O\left((s\tau)^{2\alpha}\right), \quad |s\tau| \ll 1 \tag{2.26}$$

where $\sqrt{r} = c_\infty/c_s$. The leading order large-depth approximation of the impulse response will then be

$$\Psi(x,t) \approx \Psi_0(x,t) = \frac{1}{2\pi i}\int_{\zeta-i\infty}^{\zeta+i\infty} e^{s\left(t-\frac{x}{c_s}\right)}e^{Bx(s\tau)^{1+\alpha}}ds \tag{2.27}$$

with $B = \beta\frac{r-1}{2rc_s\tau}$. To accomplish the evaluation of $\Psi_0(x,t)$, we again compute the inverse Laplace transform along a steepest descent contour in the complex s domain. Now the phase is $\phi = s\left(t-\frac{x}{c_s}\right) + Bx(s\tau)^{1+\alpha}$, and the saddle point will be

$$s^* = \frac{1}{\tau}\left(\frac{1-\frac{c_s t}{x}}{\beta\frac{r-1}{2r}(1+\alpha)}\right)^{\frac{1}{\alpha}} = \frac{1}{\tau}\left(\frac{1-\frac{\theta}{\sqrt{r}}}{1+\alpha}\frac{2r}{\beta(r-1)}\right)^{\frac{1}{\alpha}}. \tag{2.28}$$

From this expression, we see that for $t < x/c_s$, the saddle point will be real which will make the phase real as well. We first make the change of variables $s\tau = \lambda z$, with

$\lambda = (1 - \theta/\sqrt{r})^{1/\alpha}$; after substituting the second order approximation of the phase about $z = z^*$,

$$\phi \approx -\frac{x}{c_s \tau}\left(1 - \frac{\theta}{\sqrt{r}}\right)^{1+1/\alpha}\left(\frac{\alpha}{1+\alpha}z^* + \frac{\alpha}{2z^*}(z - z^*)^2\right) + O\left((z - z^*)^3\right) \tag{2.29}$$

where $z^* = (\beta(1-\alpha)(r-1)/2r)^{-1/\alpha}$. Integration of this expression yields

$$\Psi_0 \approx \frac{1}{\tau}\sqrt{\frac{z^*\lambda c_s \tau}{2\pi\alpha(x - c_s t)}}e^{-\frac{\alpha}{1+\alpha}z^*\lambda(\frac{x}{c_s}-1)}\left(1 + O\left(\frac{1}{\lambda}\right)\right). \tag{2.30}$$

Unfortunately, this expression is no longer valid near $t = x/c_s$, since $\lambda \to 0$, and therefore the asymptotic series diverges.

Fortunately, we can still evaluate (2.27) by finding a parametric form of the steepest descent contour, as in the case of the shallow-depth response, and discretize the integral. By setting $s\tau = \rho e^{i\sigma}$, and setting the imaginary part of the phase to zero, we obtain the parametric form

$$\rho(\sigma) = s^* S(\sigma; 1, 1+\alpha)^{\frac{1}{\alpha}}, \quad -\frac{\pi}{1+\alpha} < \sigma < \frac{\pi}{1+\alpha}, \tag{2.31}$$

where the $S(\sigma; a, b)$ is again given by equation (2.23), and the interval is taken to ensure that the expression remains real for $t < x/c_s$. Note that this expression satisfies $\rho(0) = s^*$.

When $t > x/c_s$, the saddle point vanishes, since it passes into the branch cut on the negative real $s-$axis; however the same expression (2.31) will still define a steepest descent contour. It is merely the domain that must be changed, which is instead comprised of the disjoint intervals $\sigma \in (-\pi, \pi/(1+\alpha)) \cup (\pi/(1+\alpha), \pi)$. On these intervals, $\sin((1+\alpha)\sigma) < 0$, which makes $S(\sigma; 1, 1+\alpha) < 0$; but this sign change is compensated by an additional change in the numerator of s^* due to $1 - c_s t/x$, and therefore the parametric representation remains real. The two disjoint intervals in σ form a cusp at the origin in the complex s domain, which corresponds to $\rho(\pm\pi) = 0$. The two regimes, namely that with the saddle point, and that with cusps,

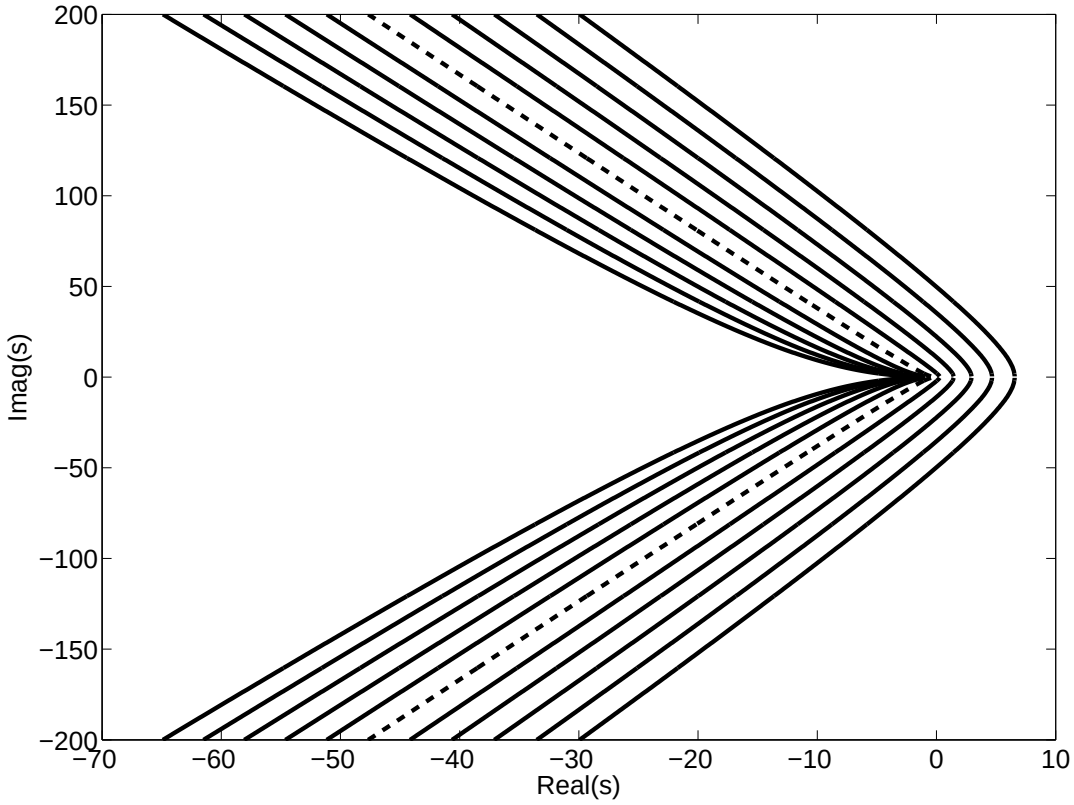

Figure 2.6 Steepest descent contour of the large-depth approximation, with increasing values of $\theta = \frac{c_\infty t}{x}$. The separatrix (dotted line) is given by $s = \rho e^{\pm \pi i/(1+\alpha)}, \rho > 0$, and corresponds to $t = x/c_s$.

are separated by the steepest descent contour along which $t = x/c_s$, as is shown in Figure 2.6. This latter curve will be comprised of the two rays $s\tau = \rho e^{\pm \pi i/(1+\alpha)}$, and must therefore be treated separately. Note that this behavior in the steepest descent contours is similar to those of the exact impulse response, shown in Figures 2.1 and 2.2.

We can now express the approximate impulse response for $t \neq x/c_s$ by replacing $s\tau = \rho(\sigma)e^{i\sigma}$, and retaining the real part of the resulting integral; the imaginary part is odd with respect to the imaginary axis, and will therefore vanish. After some

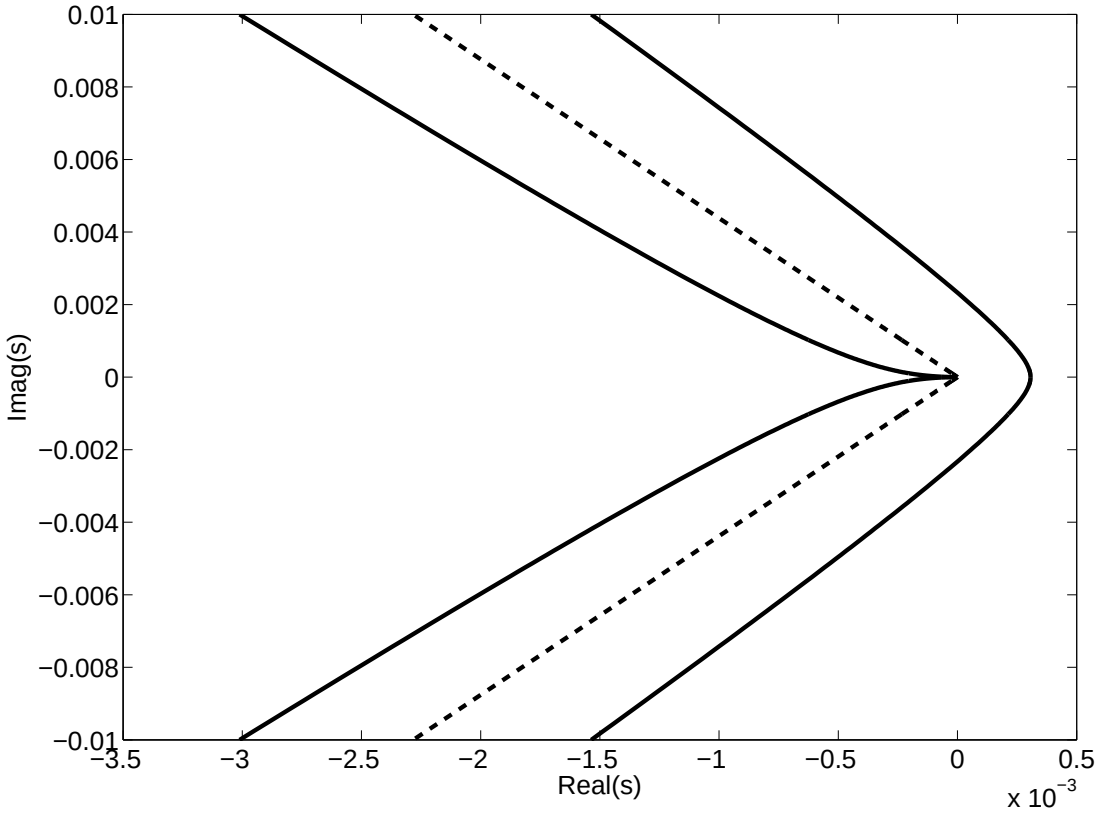

Figure 2.7 Behavior of the contour near the origin. The behavior of the contours for $\theta > \frac{c_s t}{x}, \theta = \frac{c_s t}{x}$ and $\theta < \frac{c_s t}{x}$ are shown. The separatrix (dotted line) is given by $s = \rho e^{\pm \pi i/(1+\alpha)}, \rho > 0$, and corresponds to $t = x/c_s$.

manipulation, we obtain

$$\Psi_0(x,t) = \frac{1}{2\pi\tau} \int \exp\left[\left(\frac{t}{\tau} - \frac{x}{c_s\tau}\right)\rho(\sigma)\alpha S(\sigma;\alpha,1)\right]\rho(\sigma)S(\sigma;\alpha,1+\alpha)d\sigma, \quad (2.32)$$

where the endpoints are chosen depending on the sign of $t - x/c_s$. This integral can be approximated with exponential accuracy using the trapezoidal rule,

$$\Psi_0(x,t) \approx \frac{1+\alpha}{2N\alpha\tau} \sum_{k=-N}^{N} \exp\left[\left(\frac{t}{\tau} - \frac{x}{c_s\tau}\right)\rho(\sigma_k)\alpha S(\sigma_k;\alpha,1)\right]\rho(\sigma_k)S(\sigma_k;\alpha,1+\alpha), \quad (2.33)$$

where

$$\sigma_k = \begin{cases} \frac{k}{N}\frac{\pi}{1+\alpha}, & t < \frac{x}{c_s} \\ \pi - \frac{k}{N}\frac{\alpha\pi}{1+\alpha} & t > \frac{x}{c_s} \end{cases} \tag{2.34}$$

The expression at the point $t = x/c_s$ is actually simpler, and can be evaluated analytically. At this point, the saddle point vanishes, and the expression (2.31) is no longer valid; the phase simplifies to $\phi = Bx(s\tau)^{1+\alpha}$, which can be made real along the rays $\arg s = \pm\pi/(1+\alpha)$. The approximate impulse response is thus given by

$$\begin{aligned} \Psi_0(x, t = x/c_s) &= \frac{1}{2\pi i}\int_{\zeta-i\infty}^{\zeta+i\infty} e^{Bx(s\tau)^{1+\alpha}} ds \\ &= \frac{1}{2\pi i}\left[e^{-\gamma\pi i}\int_{-\infty}^{0} e^{-Bxv^{1+\alpha}} dv + e^{\gamma\pi i}\int_{0}^{\infty} e^{-Bxv^{1+\alpha}} dv\right] \\ &= \frac{1}{\pi}\sin(\gamma\pi)(Bx)^{-\gamma}\int_{0}^{\infty} e^{-v^{1+\alpha}} dv \\ &= \frac{1}{\Gamma(\gamma)\Gamma(1-\gamma)}\gamma(Bx)^{-\gamma}\int_{0}^{\infty} e^{-u}u^{\gamma-1} du \\ &= \frac{\gamma}{\Gamma(1-\gamma)}(Bx)^{-\gamma}, \end{aligned} \tag{2.35}$$

where $\gamma = \frac{1}{1+\alpha}$, and we have used the identity $\Gamma(1-z)\Gamma(z) = \pi/\sin(\pi z)$.

The approximate impulse response is compared in Figures 2.8 and 2.9 for the same parameters as Figures 2.3 and 2.4, with $x = 100c_\infty\tau$. Once again, the hyperbolic contour is used to evaluate the exact impulse responses Ψ. As illustrated in Figures 2.8 and 2.9, the approximate impulse response clearly improves as α increases, but in both cases the peak of the exact impulse response is underestimated. The saddle point approximation is not shown, since it does not provide an accurate approximation for $t \geq x/c_s$.

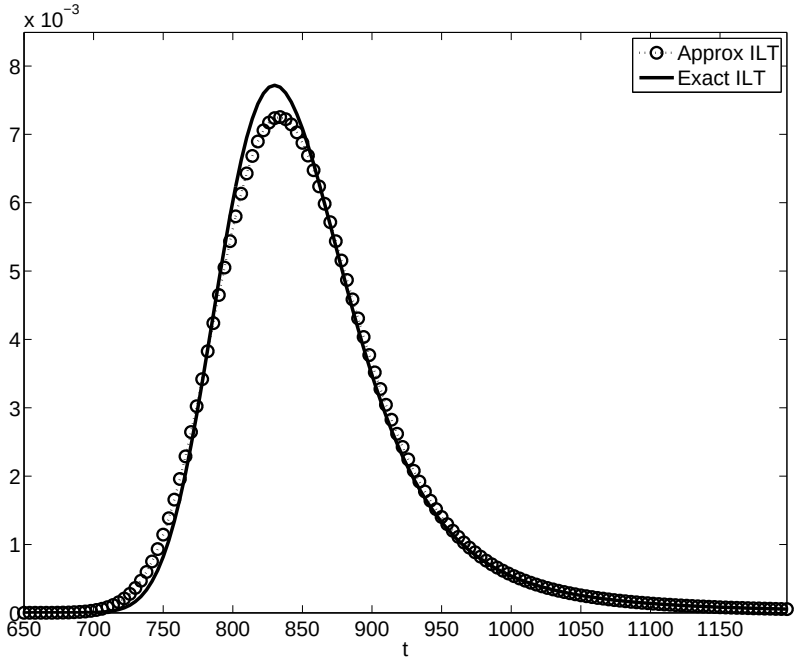

Figure 2.8 Validation of the large-depth approximation of the H-N Impulse Response, at $x = 100c_\infty\tau$, and $(\alpha, \beta) = (0.6, 0.75)$.

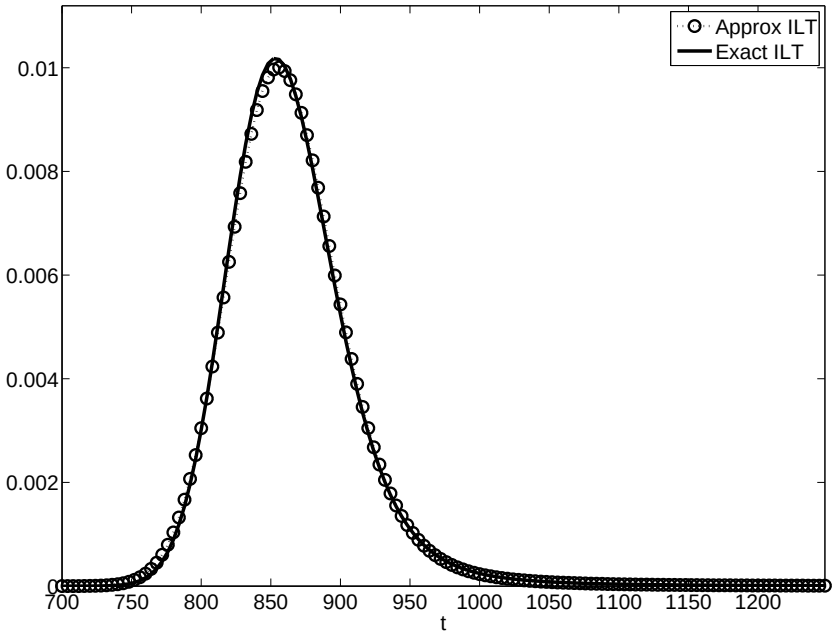

Figure 2.9 Validation of the large-depth approximation of the H-N Impulse Response, at $x = 100c_\infty\tau$, and $(\alpha, \beta) = (0.8, 0.75)$.

CHAPTER 3

THE COLE-COLE DIELECTRIC MODEL

3.1 Introduction

In this chapter we will develop a means of implementing the Cole-Cole model using FD-TD methods. The Cole-Cole model introduces a fractional power of the temporal frequency to describe the dielectric relaxation, which leads to a time-domain fractional differential equation (FDE) for the constitutive law in Maxwell's equations. From a numerical standpoint, this is of consequence, as fractional derivatives are defined by convolution integrals which are nonlocal in time and expensive to evaluate.

Despite these difficulties, the Cole-Cole model has recently received a good deal of attention [37], [26], [22], [31], [36]. In most of the existing formulations, the underlying idea is to use a basis of exponential functions $e^{-\xi_j t}$ to approximate the slowly decaying kernel $K_\alpha(t) = t^{-\alpha}/\Gamma(1-\alpha)$ in the fractional derivative. This amounts to approximating a Cole-Cole term with a number of Debye terms. The strengths and locations of the poles are determined using various optimization methods, which are applied in the frequency domain. Consequently, there is no a priori information about the accuracy of the resulting Cole-Cole approximation in the time domain. In fact, such frequency domain constructions cannot address the singular nature of $K_\alpha(t)$ for $t \to 0^+$, which is crucial in accurately capturing the polarization dynamics.

There will be two sources of error in any FD-TD approximation of the Cole-Cole model: the error in approximating the Cole-Cole term, which is essentially controlled by the number of Debye terms N; and the standard discretization error introduced by the FDTD method, which is controlled by the size of the time step Δt, and the computational time $T = N_t \Delta t$. In principal, an optimal implementation would then place these two sources on the same order, (in the case of FD-TD, the discretization

error is second order in space and time). However, this implied relationship between $N = N(\Delta t, T)$ has not yet been established in the literature. Herein we will develop a means to impose upon the Cole-Cole term approximation an accuracy of $O(\Delta t^2)$, uniformly over a preset computational interval $[0, T]$. Additionally, an explicit proof of stability will be given for our scheme, which will show that the standard CFL condition is preserved. Our analysis can be extended to the methods of [26], [37], [22], and [36], and it is likely that the same is true of [31].

Concurrently several related mathematical models involving fractional ordinary differential equations have been explored: fractionally damped dynamic systems [42]; porous media with singular memory [16]; and fractional viscoelasticity [11]. These methods all utilize various quadrature schemes to derive a sum of exponentials (i.e., Debye terms) approximation in the time domain for the kernel $K_\alpha(t)$. The use of quadrature to obtain this approximation was first put forth by Yuan and Agrawal [42], and successive improvements have been made in [16], [11]. In particular, Diethelm's construction [11] exhibits high accuracy levels in the approximation of fractional ODEs. But recent work by Beylkin and Monzón [3] has made possible a sum of exponentials approximation for singular non-oscillatory functions, which is minimal in the number of terms required, and maintains a preset tolerance level ϵ over a desired time interval.

In order to examine the accuracy of an approximation for the fractional derivative, we must first define some criterion that a given approximation must satisfy. Thus we ask:

given a function $K(t)$ over an interval $[\delta, T]$, what is the optimal choice for a sum of exponentials approximation of K, that has a uniformly bounded absolute error ϵ?

That is, we seek (w_j, ξ_j) such that

$$\max_{\delta \le t \le T} \left| K(t) - \sum_{j=1}^{M} w_j e^{-\xi_j t} \right| < \epsilon. \tag{3.1}$$

Clearly the advantage of Beylkin's approach is that we can simultaneously maximize the accuracy of the approximation of $K(t)$, and minimize the number of exponentials required, which in this sense is optimal. Li [25] has made a construction of this type for fractional integrals, but imposes the condition with $T = \infty$; hence the approximation will be suboptimal, as N will be excessively large for approximations that need only be valid for a finite time.

We must point out that in using a sum of exponentials to approximate $K_\alpha(t)$, the representation will inherently break down in some interval $t \in [0, \delta]$ containing the origin, where $K_\alpha(t)$ becomes singular. This will require a separate treatment in this region, which has a bearing on the accuracy of the resulting numerical scheme.

3.2 Fractional Derivatives

We first study independently the numerical application of fractional derivatives, and their use in fractional differential equations (FDEs). The polarization law for the Cole-Cole model can be posed as an FDE, which follows from the taking the Laplace transform of equation (1.6),

$$\hat{P}(x, s) = \epsilon_0 \hat{\chi}(s) \hat{E}(x, s) \tag{3.2}$$

where

$$\hat{\chi}(s) = \frac{\epsilon_s - \epsilon_\infty}{1 + (s\tau)^\alpha}. \tag{3.3}$$

Upon multiplying by the denominator, and inverting to the time domain, we produce the polarization law

$$\tau^\alpha D_t^\alpha P + P = \epsilon_0(\epsilon_s - \epsilon_\infty)E, \quad t > 0, \tag{3.4}$$

The term $D_t^\alpha P$ is the fractional derivative of P, of order α, and can be interpreted in several related, but different manners. Most commonly the Caputo definition of

the fractional derivative is taken, which preserves the well-posedness of the Cauchy problem [10] by introducing initial data in terms of P, rather than its fractional derivative. This is accomplished by splitting the term s^α, so that

$$\begin{aligned} D_t^\alpha P &= \mathcal{L}^{-1}\{s^\alpha \hat{P}\} = \mathcal{L}^{-1}\{(s^{\alpha-1})(s\hat{P})\} \\ &= \mathcal{L}^{-1}\{s^{\alpha-1}\} * \mathcal{L}^{-1}\{s\hat{P}\} = \frac{t^{-\alpha}}{\Gamma(1-\alpha)} * \left[\frac{dP}{dt} + P(x,0)\right], \end{aligned} \tag{3.5}$$

where $*$ denotes convolution in time. For the polarization, we can (without loss of generality) take $P(x,0) = 0$, so that the Caputo fractional derivative of order α is defined as

$$D_t^\alpha P = \int_0^t K_\alpha(u) \frac{\partial P}{\partial t}(x, t-u)du, \tag{3.6}$$

where $\Gamma(\cdot)$ is the gamma function, and where the kernel of the fractional derivative is given by

$$K_\alpha(t) = \frac{t^{-\alpha}}{\Gamma(1-\alpha)}, \quad 0 < \alpha < 1. \tag{3.7}$$

For now, we suppress the x-dependence of P, since it does not affect the results. We will also compute the numerical approximation of the fractional derivative on a uniform grid in time. If a straightforward approach is used to discretize the integral (i.e., trapezoidal rule), then the computation of the fractional derivative at each time level will be of the form

$$(D_t^\alpha P)^n = h \sum_{m=0}^{n-1} K_\alpha^m \dot{P}^{n-m}, \tag{3.8}$$

where h is the step size, and $\dot{P}^n = \frac{dP}{dt}(nh)$. This inevitably leads to a bottleneck, since the number of terms that must be summed grows at each time step; thus *each time steps takes longer to compute than the previous time step*! The computational time required to compute the fractional derivative over N_t time steps will thus be $O(N_t^2)$. This can be avoided by using fast convolution techniques [15], [20], which replace

the convolution kernel with an approximation that is used to localize the convolution procedure.

In order to make use of the fast techniques (see, e.g. [25], [20]) for convolution, we observe that $K_\alpha(t)$ in equation (3.7) is a non-oscillatory, decaying function; thus it can be approximated using a sum of real decaying exponentials, with the approximation maintaining a precision ϵ over some interval, $\delta \leq t \leq T$. The region $[0, \delta]$ must be treated separately, since it contains the singularity of $K_\alpha(t)$ and therefore the exponentials approximation cannot hold there. We will judiciously choose $\delta = q\Delta t$, with q a small integer (i.e., 1 and 2), so that the endpoints of the integration coincide with the temporal grid points. The sum of exponentials approximation will then be of the form

$$K_\alpha^N(t) = \sum_{j=1}^{N} w_j e^{-y_j t}, \quad q\Delta t \leq t \leq T. \tag{3.9}$$

Once such an approximation is obtained, the fractional derivative can be computed efficiently in $O(N)$ time at each time step, where N is much smaller than the number of time steps $N_t = T/h$, and in many cases is given by the relation $N = O(\log N_t)$. Thus, these fast algorithms will compute the fractional derivative over N_t time steps in $O(N_t \log N_t)$ time. The fractional derivative at time $t_{n+1} = (n+1)h$ is therefore comprised of a local and history part,

$$(D_t^\alpha P)^{n+1} = \psi_\ell^{n+1} + \psi_h^{n+1}, \tag{3.10}$$

where

$$\psi_\ell^{n+1} = \int_0^{qh} K_\alpha(u) \frac{dP}{dt}(t_{n+1} - u) du, \tag{3.11}$$

$$\psi_h^{n+1} = \int_{qh}^{t_{n+1}} K_\alpha^N(u) \frac{dP}{dt}(t_{n+1} - u) du. \tag{3.12}$$

The parameter q serves to produce a hybridization between the classical convolution approach (which corresponds to $q = n + 1$), and a purely fast convolution approach

($q = 0$). The optimal choice of q is made when the order of convergence of both contributions to the fractional derivative are of the same order; as we shall show below, it turns out to be $q = 2$.

3.2.1 Local Approximation

The local contribution ψ_ℓ is discretized by replacing $P(t_{n+1} - u)$ with an interpolating polynomial, and integrating the resulting expression analytically. In the case that $P(t)$ is a known function, we consider the case $q = 1$, and approximate $\dot{P}$ directly over the interval $[0, h]$ with the linear interpolant

$$\dot{P}(t-u) = \left(1 - \frac{u}{h}\right)\dot{P}^{n+1} + \frac{u}{h}\dot{P}^n + O(h^2), \quad 0 < u < h, \tag{3.13}$$

and integrate this approximation analytically. This results in

$$\begin{aligned}\psi_\ell^{n+1} &= \int_0^h \frac{u^{-\alpha}}{\Gamma(1-\alpha)}\left[\left(1 - \frac{u}{h}\right)\dot{P}^{n+1} + \frac{u}{h}\dot{P}^n\right] du \\ &= \frac{h^{-\alpha}}{\Gamma(3-\alpha)}\left[\dot{P}^{n+1} + (1-\alpha)\dot{P}^n\right].\end{aligned} \tag{3.14}$$

However this method only applies to cases when P is a known function; i.e., if we are simply computing a fractional derivative.

In the consideration of fractional differential equations, we instead compute the fractional derivative of an unknown quantity. Thus, the local contribution ψ_ℓ is discretized by replacing $P(t_{n+1} - u)$ (rather than its derivative) with an interpolating polynomial through the points P^{n+1-k} for $k = 0, 1, \ldots q$, and integrating the remaining expression analytically. This will result in a family of approximations of the form

$$\psi_\ell^{n+1} = \sum_{k=0}^{q} A_k^q P^{n+1-k}. \tag{3.15}$$

We will derive the coefficients A_k^q using interpolating polynomials, so that the error of our approximation is given by the following

Lemma 1 *For $q = 1, 2, \ldots$, define the interpolating polynomial of order q for $P(t-u)$, passing through the points $P(t - jh), j = 0, 1, \ldots q$. Then, the interpolant is accurate to order h^{q+1}, and for $P \in C^{q+1}[t-h, t]$, we have*

$$\int_0^{qh} \frac{u^{-\alpha}}{\Gamma(1-\alpha)} \frac{dP}{dt}(t-u)du = \sum_{k=0}^{q} A_k^q P^{n-k} + O(h^{q+2-\alpha}). \tag{3.16}$$

The local truncation error will then be $O(h^{q+1-\alpha})$.

Proof 1 *An interpolating function of $P(t-u)$ through $q+1$ points $P^n, P^{n-1}, \ldots P^{n-q}$, where $t = nh$, will be of the form*

$$P(nh-u) = \sum_{j=0}^{q} a_{jq}(u) P^{n-q} + f_q(u;h) \frac{d^{q+1}P}{dt^{q+1}}(\xi), \tag{3.17}$$

where a_{jq} are polynomials of degree q or less; f_q is a homogeneous polynomial of degree $q+1$, satisfying $f_q(u;h) = h^{q+1} f(\frac{u}{h}; 1)$; and $\xi \in [0, qh]$. Upon differentiating with respect to u, multiplying by $u^{-\alpha}$ and integrating over $[0, qh]$ we derive a numerical scheme, and retain the error term. Thus, the error will be of the form

$$\int_0^{qh} u^{-\alpha} f'(u;h)du = h^{q+2-\alpha} \int_0^q v^{-\alpha} f'(v;1)dv = Ch^{q+2-\alpha}. \tag{3.18}$$

The local truncation error will be one order less than this, giving the indicated convergence rate of $O(h^{q+1-\alpha})$.

Thus the resulting overall accuracy is less than second order for the $q = 1$ method. Since the FD-TD method is a second order accurate scheme, we are only interested in $q = 1, 2$. In the case $q = 1$, we proceed by replacing $\dot{P}$ with a standard finite difference approximation over the interval $[0, h]$, and therefore

$$\begin{aligned} \psi_\ell^{n+1} &= \int_0^h \frac{u^{-\alpha}}{\Gamma(1-\alpha)} \dot{P}(t_{n+1} - u)du \\ &= \frac{1}{\Gamma(1-\alpha)} \int_0^h u^{-\alpha} \frac{P^{n+1} - P^n}{h} du \\ &= \frac{h^{-\alpha}}{\Gamma(2-\alpha)} \left(P^{n+1} - P^n\right), \end{aligned} \tag{3.19}$$

so that for the case $q = 1$, the coefficients are given as

$$A_0^1 = -A_1^1 = \frac{h^{-\alpha}}{\Gamma(2-\alpha)}. \tag{3.20}$$

The important point to note is that because the derivative $\frac{dP}{dt}(t-u)$ is being represented with function values $P(t_n), P(t_{n-1})$ etc. (rather than $\frac{dP}{dt}$ at the same locations), there is a loss of accuracy. Thus, the standard finite difference approximation does not produce a second order approximation. For the case $q = 2$, and the interpolating polynomial is a parabola through P^{n+1}, P^n and P^{n-1}, so that

$$\dot{P}(t_{n+1}-u) \approx \frac{3P^{n+1}-4P^n+P^{n-1}}{2h} + -u\frac{P^{n+1}-2P^n+P^{n-1}}{h^2} + O(h^2), \quad 0 \le u \le 2h. \tag{3.21}$$

Upon inserting this approximation into equation (3.11), we obtain the local contribution

$$\begin{aligned}
\psi_\ell^{n+1} &= \int_0^{2h} \frac{u^{-\alpha}}{\Gamma(1-\alpha)} \dot{P}(t_{n+1}-u)du \\
&= \frac{1}{\Gamma(1-\alpha)} \int_0^{2h} u^{-\alpha} \left(\frac{3P^{n+1}-4P^n+P^{n-1}}{2h} \right) - u^{1-\alpha} \left(\frac{P^{n+1}-2P^n+P^{n-1}}{h^2} \right) du \\
&= \frac{(2h)^{-\alpha}}{\Gamma(3-\alpha)} \left[(2+\alpha)\left(P^{n+1}-P^n\right) + (2-3\alpha)\left(P^n-P^{n-1}\right) \right],
\end{aligned} \tag{3.22}$$

which indicates that the coefficients are now given as

$$A_0^2 = \frac{(2h)^{-\alpha}}{\Gamma(3-\alpha)}(2+\alpha) \quad A_1^2 = \frac{(2h)^{-\alpha}}{\Gamma(3-\alpha)}(-4\alpha) \quad A_2^2 = \frac{(2h)^{-\alpha}}{\Gamma(3-\alpha)}(3\alpha-2) \tag{3.23}$$

3.2.2 History Approximation

The history contribution can similarly be written as a sum of auxiliary variables; using the definition (3.9) of $K_\alpha^N(t)$, we have

$$\psi_h^{n+1} = \sum_{j=1}^{N} w_j \phi_j^{n+1}, \tag{3.24}$$

where

$$\phi_j^{n+1} = \int_{qh}^{(n+1)h} e^{-y_j u} \frac{dP}{dt}(t_{n+1} - u)du, \quad j = 1, 2, \ldots N. \tag{3.25}$$

This construction is still general, as it will hold for any choice (w_j, y_j) that forms an approximation K_α^N; we postpone an explicit choice of these parameters to first attend to the theoretical matters. With some standard manipulations, one can show that ϕ_j satisfies both a recurrence relation, as well as an ordinary differential equation:

$$\phi_j(t_{n+1}) = e^{-y_j h}\phi_j(t_n) + e^{-y_j qh} \int_0^h e^{-y_j u} \frac{dP}{dt}(t_{n+1-q} - u)du \tag{3.26}$$

$$\phi_j + y_j \frac{d\phi_j}{dt} = e^{-y_j qh} \frac{dP}{dt}. \tag{3.27}$$

These expressions can be used to derive an appropriate rule using either exponential time differencing, or the standard finite differences (trapezoidal rule) respectively. Both of these schemes are of the form

$$\phi_j^{n+1} = d_j \phi_j^n + c_j \left(P^{n+1-q} - P^{n-q} \right), \quad j = 1, 2 \ldots N. \tag{3.28}$$

For the trapezoidal rule, discretization results in

$$d_j = \frac{2 - y_j h}{2 + y_j h}, \quad c_j = e^{-y_j qh} \frac{2}{2 + y_j h}, \tag{3.29}$$

and is known to converge with second order accuracy. The corresponding exponential differences rule can be derived by replacing $\dot{P}$ with a standard finite difference approximation, and integrating the exponential. Thus

$$d_j = e^{-y_j h}, \quad c_j = e^{-y_j qh} \frac{1 - e^{-y_j h}}{y_j h}. \tag{3.30}$$

We now show that equation (3.28) with coefficients defined by (3.30) produces a second order accurate scheme. Comparison with equation (3.26) shows that $d_j = e^{-y_j h}$ is the exact choice, and so the only source of error is from the approximation of the

integral; thus we define the error

$$\mathcal{L}[\phi_j] = \int_0^h e^{-y_j u} \frac{dP}{du}(t_n - u)du - \frac{1 - e^{-z}}{z}(P^n - P^{n-1}). \tag{3.31}$$

Lemma 2 *For $P \in C^2[t-h, t]$, we have*

$$\mathcal{L}[\phi_j] = C_j \frac{z_j h^2}{12} \frac{d^2 P}{dt^2}(t - \xi), \tag{3.32}$$

where $z_j = y_j h$, and $C_j = \min(1, 6(z_j)^{-2})$. Therefore the local truncation error of equation (3.28) with coefficients defined by (3.30) is second order.

Proof 2 *We first construct the linear interpolant for $P(t-u)$ through the points $P(t), P(t-h)$, and retain the error term. Differentiation of the interpolant produces the standard finite difference approximation of $\frac{dP}{dt}$*

$$\frac{dP}{dt}(t-u) = \frac{P(t) - P(t-h)}{h} + \left(\frac{h}{2} - u\right) \frac{d^2 P}{dt^2}(t - \xi), \quad 0 \le u \le h \tag{3.33}$$

for some $\xi \in [0, h]$. Multiplying by $e^{-y_j u}$ and integrating results in (3.31), which is equal to

$$\mathcal{L}[\phi_j] = \frac{d^2 P}{dt^2}(t - \xi) \int_0^h e^{-y_j u} \left(\frac{h}{2} - u\right) du = \frac{d^2 P}{dt^2}(t - \xi)\gamma(z_j)h^2, \tag{3.34}$$

where

$$\gamma(z) = \frac{1}{2z^2}\left((2+z)e^{-z} - (2-z)\right). \tag{3.35}$$

Over the positive real line, the function $\gamma(z)$ is concave, satisfying $\gamma(0) = \gamma(\infty) = 0$, and attaining a global maximum at $\gamma(2.688) = 0.0697$. Expanding $\gamma(z)$ for large and small arguments, we have the uniform upper bound

$$\gamma(z) \le \frac{z}{12} \begin{cases} 1 & 0 < z \le \sqrt{6} \\ \frac{6}{z^2} & z > \sqrt{6} \end{cases} \tag{3.36}$$

which implies equation (3.32)*. The local truncation error of equation* (3.28) *is defined as*

$$\frac{1}{z_j}\left(\phi_j^{n+1} - e^{-z_j}\phi_j^n - e^{-qz_j}\frac{1-e^{-z_j}}{z_j}(P^{n+1-q} - P^{n-q})\right) = \frac{e^{-qz_j}}{z_j}\mathcal{L}[\phi_j], \tag{3.37}$$

and is therefore second order accurate in time.

The full numerical approximation of the fractional derivative will then consist of two steps. First the auxiliary variables ϕ_j are updated

$$\phi_j^{n+1} = e^{-y_j h}\phi_j^n + e^{-y_j q h}\left(\frac{1-e^{-y_j h}}{y_j}\right)\frac{P^{n+1-q} - P^{n-q}}{h}, \quad j = 1, 2, \cdots N, \tag{3.38}$$

then the fractional derivative can be updated

$$(D_t^\alpha P)^{n+1} = \sum_{k=0}^{q} A_k^q P^{n+1-k} + \sum_{j=1}^{N} w_j \phi_j^{n+1}. \tag{3.39}$$

For comparison, we also consider the $q = 0$ implementation. This is equivalent to directly substituting $K_\alpha(t) = K_\alpha^N$ into equation (3.6), so that

$$[D_t^\alpha P]^{n+1} = \sum_{j=1}^{N} w_j \phi_j^{n+1} \tag{3.40}$$

and where ϕ_j are still given by (3.28), with coefficients from either (3.29) or (3.30).

3.3 Approximation of $K_\alpha^N(t)$

All of the above results hold in general for any approximation $K_\alpha^N(t)$; now we make such a construction as given by Beylkin and Monzón [3], which exhibits explicit dependence on the time interval of interest (i.e., the length of the FDTD simulation). Given a specified error tolerance ϵ and a time interval $[\Delta t, T]$, the approximation is constructed as follows:

- Set $z^- = \frac{1}{\alpha}\left(\log\epsilon + \log\Gamma(\alpha+1)\right)$.

- Set $z^+ = \log(-\frac{\alpha}{\Delta t}\log(\epsilon)) + 1 + \frac{1}{2\alpha}$.
- Set $h = \frac{2\pi}{1+\alpha-\log\epsilon}$, and $N_0 = \lceil \frac{z^+ - z^-}{h} \rceil$.
- For $j = 1, \cdots N_0$, define $z_j := z^- + jh$ and

$$w_j := \frac{h}{\pi}\sin(\pi\alpha)e^{\alpha z_j}, \quad y_j := e^{z_j}. \tag{3.41}$$

Then we have

$$\left\| K_\alpha(t) - K_\alpha^{N_0}(t) \right\|_\infty < \epsilon, \quad t \in [\Delta t, T]. \tag{3.42}$$

This construction produces a quadrature that maintains a uniform accuracy ϵ over the computation interval $t \in [\Delta t, T]$; it is not optimal however, as the number of nodes and weights N_0 can still be reduced without sacrificing the overall accuracy. In fact, the numerical rank of the matrix formed by

$$V_{mn} = e^{-y_m t_n}, \quad t_n \in [\Delta t, T] \tag{3.43}$$

will determine the optimal number of nodes. In this case the rectangular matrix V contains singular values that decay exponentially, and so the final number of nodes $N < N_0$ will grow logarithmically with the accuracy, and the time step,

$$N \sim \log\frac{1}{\epsilon} + \log\frac{T}{\Delta t}. \tag{3.44}$$

A variety of methods have been introduced in recent years to compress this matrix [41],[27]; Beylkin's method consists of choosing $t_n = n\Delta t$ which makes V a Vandermonde matrix, and using a modified version of Prony's method to perform the compression, while maintaining precision ϵ. We have found comparable results by constructing Chebyshev interpolants on subintervals of time, which were used to construct the approximations in Figures 3.3 and 3.4. Once the y_j's have been

compressed, the weights are recalculated by solving the least squares problem for (3.42) at the points t_n.

Since the exponents y_j will vary over several orders of magnitude, as observed in Figure 3.3, the resulting ODEs are inherently stiff. It is for this reason that we use exponential time differencing, which preserves the amplification factors, and reduces the numerical dissipation. However the standard approximation using the trapezoidal rule can also be implemented.

We now compare the current method of computing the fractional derivative with several of those appearing in the current literature. In order to unify the ensuing discussion, we define the fractional derivative kernel by its Laplace transform

$$K_\alpha(t) = \frac{t^{-\alpha}}{\Gamma(1-\alpha)} = \frac{\sin(\pi\alpha)}{\pi}\int_0^\infty y^{\alpha-1}e^{-yt}dy, \quad t>0, 0<\alpha<1, \tag{3.45}$$

where we have used the Euler reflection principle $\Gamma(\alpha)\Gamma(1-\alpha) = \pi/\sin(\pi\alpha)$. The fractional derivative (3.6) can now be rewritten as

$$D_t^\alpha P = \frac{\sin(\pi\alpha)}{\pi}\int_0^\infty y^{\alpha-1}\phi(t;y)dy, \tag{3.46}$$

where

$$\phi(t;y) = \int_0^t e^{-y(t-t')}\frac{dP}{dt'}dt'. \tag{3.47}$$

The convolution is now written in terms of a continuous distribution of exponentials, and is therefore a continuous analog to equation (3.24); if we view y as the inverse relaxation time, then we see that ϕ is composed of a continuum of relaxation times. Holding y fixed, and differentiating with respect to time, we can now derive an ODE that governs the behavior of ϕ

$$\frac{d\phi}{dt} + y\phi = \frac{dP}{dt}. \tag{3.48}$$

Once a suitable quadrature is introduced, discretization of the integral (3.47) will reduce the continuum to a discrete set of relaxation times, so that

$$D_t^\alpha P = \sum_{j=1}^{N} w_j \phi_j, \quad \phi_j = \phi(t; y_j), \tag{3.49}$$

which is the same equation as (3.24) with $q = 0$. Thus, the following approximation has been made implicitly

$$\frac{t^{-\alpha}}{\Gamma(1-\alpha)} \approx \sum_{j=1}^{N} w_j e^{-y_j t}. \tag{3.50}$$

The determination of weights and nodes amounts to choosing a certain integral representation for the left hand side of equation (3.50), and approximating it with an appropriately chosen quadrature; the above construction (3.41) is a particular choice.

The idea to obtain the exponentials using quadrature is not new; Yuan and Agrawal first made a change of variables $y \to y^2$ in equation (3.45), and then defined the weights and nodes using an N-point Gauss-Laguerre quadrature

$$w_j := \frac{2}{\pi} \sin(\pi\alpha) w_j^{GL} \exp(x_j^{GL}) (x_j^{GL})^{2\alpha-1}, \quad y_j := x_j^{GL}, \quad j = 1, 2, \cdots N. \tag{3.51}$$

The use of y^2 instead of y has the effect of distributing the nodes so that they span a larger region of the integration domain $(0, \infty)$, which has a dualistic relation to the range of time that is resolved. Despite their attempt, it has since been discovered [11] the points don't span a large enough range for most time stepping computations of interest. Another issue is of deeper concern, which is that the Laguerre quadrature fails to account for the asymptotic behavior of the integrand, particularly in the singular limit $y \to 0$. This singularity can be treated by using generalized Laguerre Quadrature; i.e., with the weight function $w(x) = x^{2\alpha-1}e^{-x}$ instead of just an exponential; this is what we show in Figure 3.1.

In order to mitigate the slow decay of the integrand for large y, Lu and Hanyga [16] have proposed splitting the integral at some point $c > 0$ (usually, $c = 1$), and

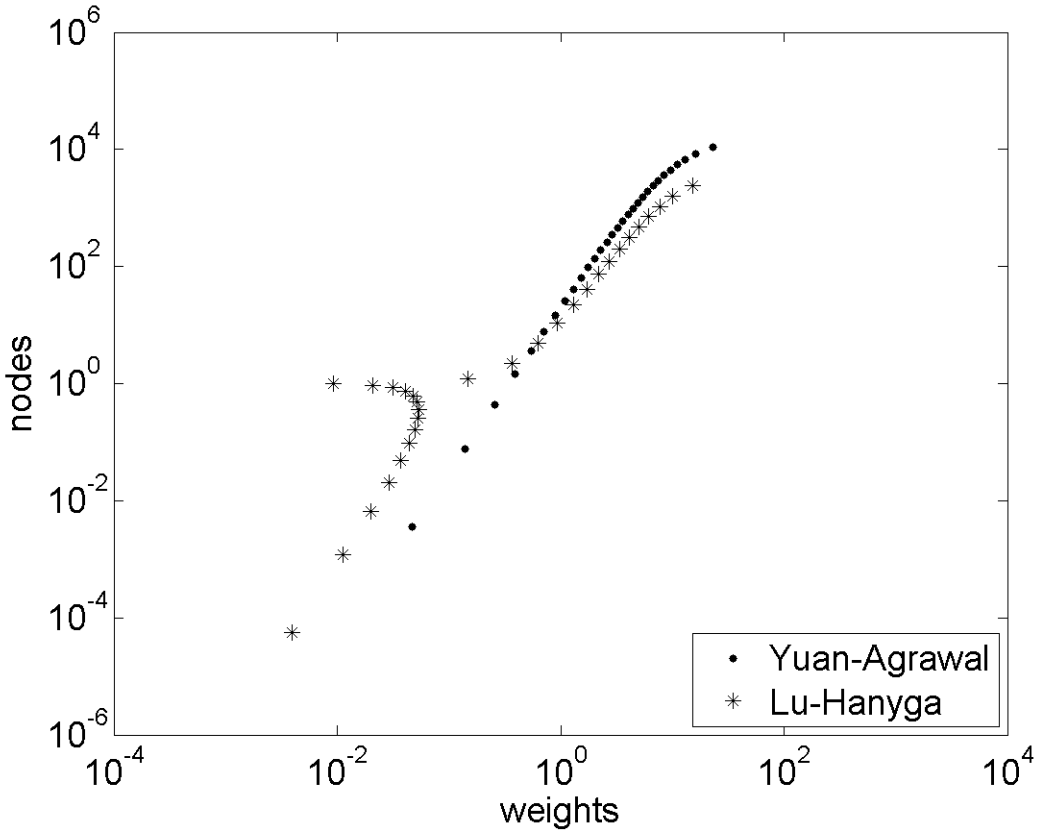

Figure 3.1 Distribution of weights and nodes with $N = 30$, and $\alpha = 0.6$. All nodes and weights are transformed, so that $t^{-\alpha}/\Gamma(1-\alpha) = \sum w_j e^{-y_j t}$. Note the effects of clustering nodes.

evaluating the first part containing the singularity using Gauss-Jacobi quadrature with weight function $w^{(0,2\alpha-1)}(x) = (1+x)^{2\alpha-1}$, and the second with a shifted Gauss-Laguerre quadrature and an additional acceleration term to accommodate the behavior at infinite. That is, if we denote the N_{GJ} nodes obtained from Gauss-Jacobi quadrature as (w_j^{GJ}, x_j^{GJ}), then

$$w_j^{(1)} := \frac{\sin(\pi\alpha)}{\pi}\left(\frac{c}{2}\right)^{2\alpha} w_j^{GJ}, \quad y_j^{(1)} := c\frac{1+x_j^{GJ}}{2},$$
$$\sum_{j=1}^{N_{GJ}} w_j e^{-y_j^2 t} \approx \int_0^c y^{2\alpha-1} e^{-y^2 t} dy. \tag{3.52}$$

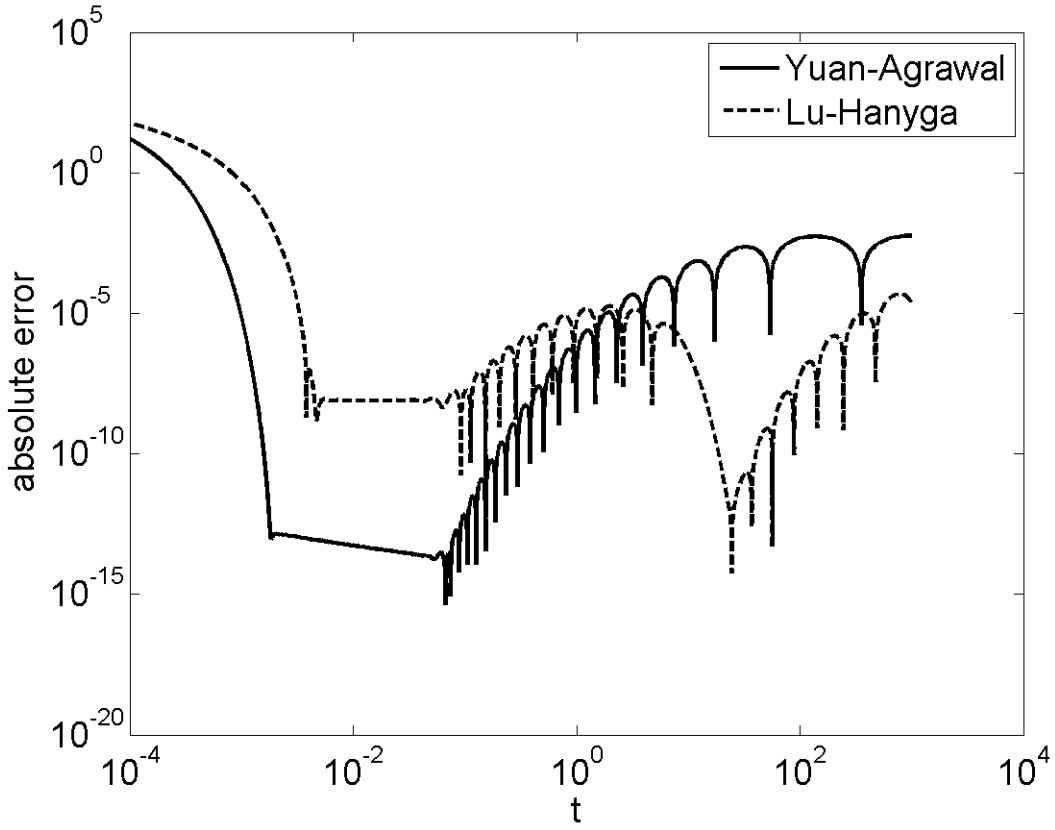

Figure 3.2 Absolute error in using an $N = 30$ term sum of exponentials to approximate the convolution kernel $t^{-\alpha}/\Gamma(1-\alpha)$, with $\alpha = 0.6$ using the Yuan-Agrawal and Lu-Hanyga methods.

Similarly, the N_{GL}-point Gauss-Laguerre weights and nodes (w_j^{GL}, x_j^{GL}) are used to construct

$$w_j^{(2)} := \frac{2}{\pi}\sin(\pi\alpha) w_j^{GL} \exp(x_j^{GL})(x_j^{GL}+c)^{2\alpha-1}, \quad y_j^{(2)} := c + x_j^{GL}, \tag{3.53}$$

$$\sum_{j=1}^{N_{GL}} w_j^{(2)} e^{-(y_j^{(2)})^2 t} \approx \int_c^\infty y^{2\alpha-1} e^{-y^2 t} dy, \tag{3.54}$$

$$g := \frac{2}{\pi}\sin(\pi\alpha)\int_c^\infty y^{2\alpha-3} dy - \sum_{j=1}^{N_{GL}} w_j^{(2)} (y_j^{(2)})^{-2} \quad . \tag{3.55}$$

The transformed weights and nodes, along with the extraction term g lead to the approximation

$$D_t^\alpha P = \sum_{j=1}^{N_{GJ}} w_j^{(1)} \phi_j^{(1)} + \sum_{j=1}^{N_{GL}} w_j^{(2)} \phi_j^{(2)} + g \frac{\partial P}{\partial t}. \tag{3.56}$$

The determination of N_{GJ}, N_{GL}, and c ultimately controls the accuracy of the approximation, yet no strategy for a good choice of these parameters is offered. We note here that this quadrature also does not lend itself to analysis of convergence, as the extraction term is represented in the time domain as a delta function,

$$\frac{t^{-\alpha}}{\Gamma(1-\alpha)} = \sum_{j=1}^{N_{GJ}} w_j^{(1)} e^{-y_j^{(1)} t} + \sum_{j=1}^{N_{GL}} w_j^{(2)} e^{-y_j^{(2)} t} + g\delta(t). \tag{3.57}$$

Diethelm has similarly utilized Gauss-Jacobi quadrature, but this time with an initial mapping to a finite domain $y = \frac{1-z}{1+z}$, so

$$\int_0^\infty y^{2\alpha-1} e^{-y^2 t} dy = \int_{-1}^{1} (1-z)^{2\alpha-1} (1+z)^{1-2\alpha} e^{\left(\frac{1-z}{1+z}\right)^2 t} \frac{2}{(1+z)^2} dz \tag{3.58}$$

This also makes the choice of Jacobi quadrature intuitive, with weight function $w^{(a,b)}(z) = (1-z)^{2\alpha-1}(1+z)^{1-2\alpha}$. With such a choice, the approximation (3.50) holds with a higher accuracy, and over a larger range of time. This quadrature is well-designed, since the algebraic singularity as $t \to 0$ (corresponding to $z \to 1$) is built into the weights. Thus,

$$w_j := \frac{4}{\pi} \sin(\pi\alpha) \frac{w_j^{GJ}}{(1+z_j^{GJ})^2}, \quad y_j := \left(\frac{1-z_j^{GJ}}{1+z_j^{GJ}} \right)^2. \tag{3.59}$$

Gautschi [14] has indicated that the approximation will converge to the integral exponentially fast when the nearest pole of ϕ in the complex z domain is bounded away from the real line segment $(-1, 1)$. This condition holds for $t \geq \delta > 0$, where $\delta = O(N^{-4})$ is determined by the number of nodes; however imposing a certain degree of uniform accuracy with this method as a function of the number of points

N is still not so straightforward. While exponential accuracy is obtained with the Jacobi quadrature for $O(1)$ time, as observed in Figure 3.4, the breakdown of the approximation for small times happens well before the the time $\delta \approx N^{-4}$.

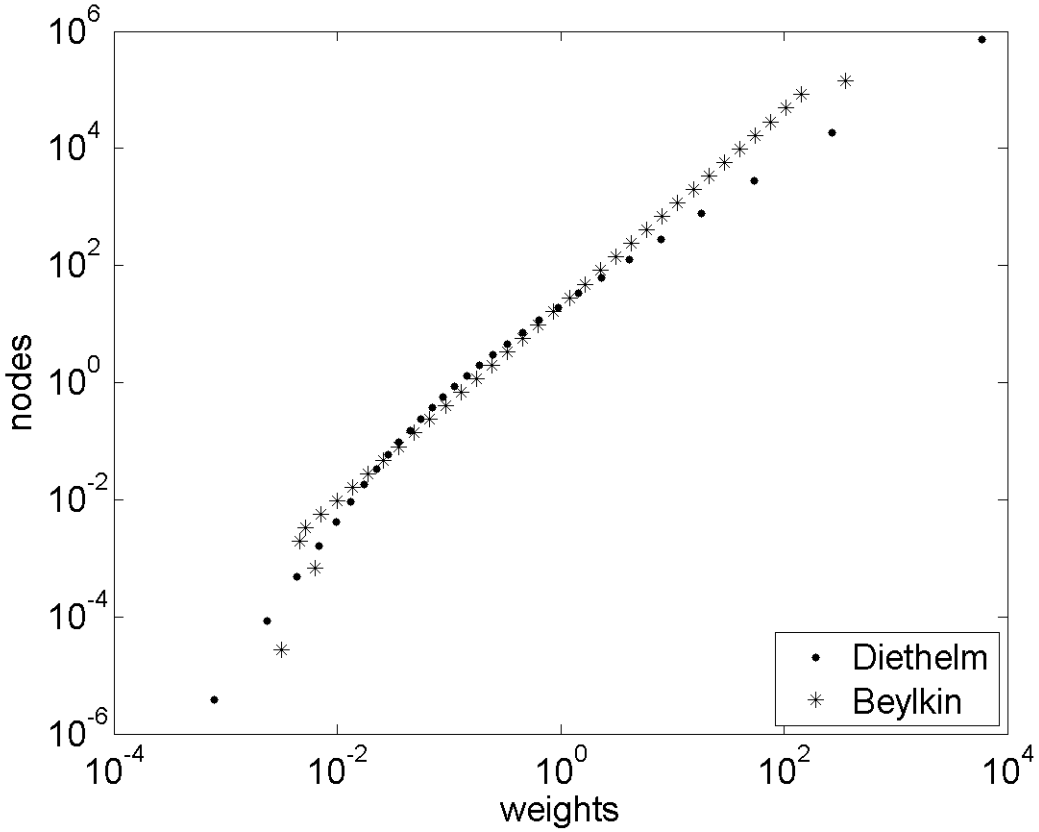

Figure 3.3 Distribution of weights and nodes with $N = 30$, and $\alpha = 0.6$. All nodes and weights are transformed, so that $t^{-\alpha}/\Gamma(1-\alpha) = \sum w_j e^{-y_j t}$. Note the effects of spreading.

The construction of equation (3.41) can be recovered by making a change of variables $y = e^z$ in equation (3.45) so that

$$t^{-\alpha} = \frac{1}{\Gamma(\alpha)} \int_{-\infty}^{\infty} e^{\alpha z - te^z} dz. \tag{3.60}$$

The rightmost integrand has some notable features, such as exponential convergence at the lower limit, and super-exponential convergence at the upper limit. Because of this, we can truncate the integration limits and bound the neglected contributions,

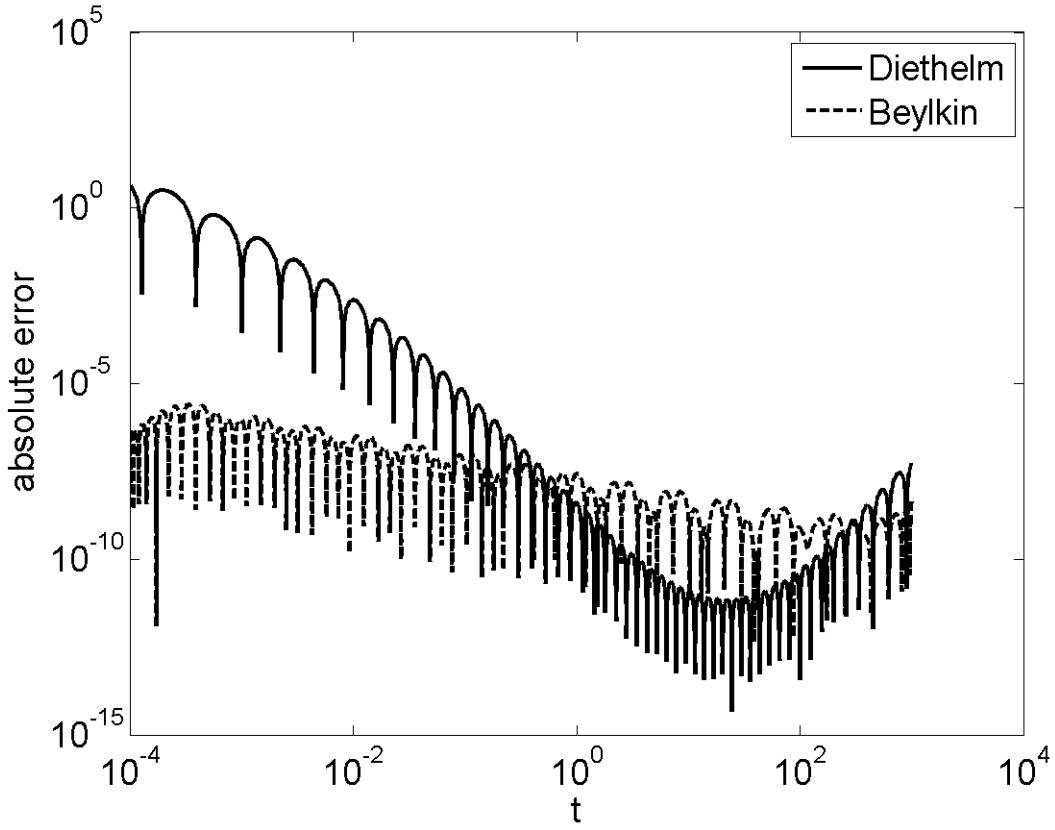

Figure 3.4 Absolute error in using an $N = 30$ term sum of exponentials to approximate the convolution kernel $t^{-\alpha}/\Gamma(1-\alpha)$, with $\alpha = 0.6$ using the Beylkin and the Gauss-Jacobi methods. Only that of Beylkin can ensure a uniform accuracy across the time interval of interest.

which will be exponentially small. The remaining integral can then be discretized using the trapezoidal rule, where the step size is determined using the Poisson summation formula and the condition that a degree of error is maintained uniformly; we refer the reader to [3] for further details.

In order to quantify how well each of the above listed methods performs, it would suffice to ask how accurate the approximation (3.50) is, and over which interval of time a given prescribe error is maintained. To this end, Figure 3.4 shows that only the construction by Beylkin can yield an a priori error bound that is uniformly maintained over a time interval of interest. The Gauss-Jacobi quadrature constructed by Diethelm actually outperforms the Beylkin construction for $O(1)$ times, where

exponential convergence is achieved; however, this behavior breaks down for small times, which would become important in resolving the transient behavior of the Cole-Cole medium. These methods are clearly better than those proposed by Yuan and Agrawal, or Lu and Hanyga.

It is no coincidence that the distribution of the weights and nodes in Figures 3.1 and 3.3 show two distinctive patterns; that is, the methods which yield more accurate approximations have a tendency to distribute the weights and nodes uniformly, over larger ranges. In fact for the Yuan-Agrawal method, the clustering of the nodes over the interval $y \in [10^2, 10^4]$ corresponds to the high resolution over the time interval $t \in [10^{-3}, 10^{-1}]$ in Figure 3.2; this is however at the expense of the accuracy in other time intervals. Similarly, the method of Lu and Hanyga also exhibits clustering that resolves certain time intervals more accurately than others.

We now take a moment to compare to work by Torres et. al [37], in which a similar implementation of the Cole-Cole model is constructed. This time, the weights and nodes are first scaled by the time step and integrated

$$\int_{m\Delta t}^{(m+1)\Delta t} \frac{u^{-\alpha}}{\Gamma(1-\alpha)} du \approx \frac{\Delta t^{1-\alpha}}{\Gamma(2-\alpha)} \sum_{j=1}^{N} a_j e^{-b_j m}. \tag{3.61}$$

The equivalence of this approach, and those above can be shown by integrating the right hand side of equation (3.50) over $[m\Delta t, (m+1)\Delta t]$, and equating the resulting expression; thus $b_j = y_j \Delta t$, and $a_j = \Delta t^{\alpha} \Gamma(2-\alpha)(1-e^{-b_j})\frac{w_j}{b_j}$. In order to arrive at this expression, the approximation that $\frac{\partial P}{\partial t}(t-u)$ is a constant over each interval is taken.

3.4 Numerical Example of Fractional Derivatives

The computation of a fractional derivative is a special case of a fractional differential equation of order α

$$D_t^{\alpha} P(t) = f(t, P(t)), \quad t > 0, \tag{3.62}$$

for which $f(t, P(t)) = f(t)$. We will first compute the fractional derivative of two trial functions that highlight the prominent quantitative features of the method of approximation

$$f_1(t) = 1 + t + t^2, \quad f_2(t) = t^3 \tag{3.63}$$

The trapezoidal and exponential methods are employed to compute the fractional derivative of order $\alpha = 0.65$ for each of the functions (3.63) over the interval $[h, 1]$ for h in the range $[9 \times 10^{-5}, 10^{-1}]$. A representative solution for each fractional derivative is shown in Figures 3.5 and 3.7, along with the resulting L^2 convergence plots in Figures 3.6 and 3.8. For reference, the fractional derivative for monomials is given by

$$D_t^\alpha \left(t^k\right) = \frac{\Gamma(k+1)}{\Gamma(k+1-\alpha)} t^{k-\alpha}, \quad k > 0, \tag{3.64}$$

and where the fractional derivative of a constant ($k = 0$) is zero, as can be observed by appealing directly to the Caputo definition (3.6). The exponentials were obtained using Gauss-Jacobi quadrature, and are held fixed with $N = 40$ terms in each implementation. The size of the exponentials y_j span the range $[10^{-6}, 5 \times 10^6]$. This is in agreement with the asymptotic behavior of the Gauss-Jacobi nodes, which gives the smallest exponential to be $y_1 = c_1 N^{-4}$, and the largest by $y_N = c_2 N^4$. The constants c_1 and c_2 are both $O(1)$, and depend on α.

We are now presented with a dilemma; the range of the exponentials indicates that the resulting ODEs are stiff, and while the parameter N increases the accuracy of the fractional derivative approximation (3.9), it simultaneously increases the stiffness of the resulting system. This is both problematic and unavoidable for long time simulations, for which N must chosen large to maintain accuracy over the entire time interval.

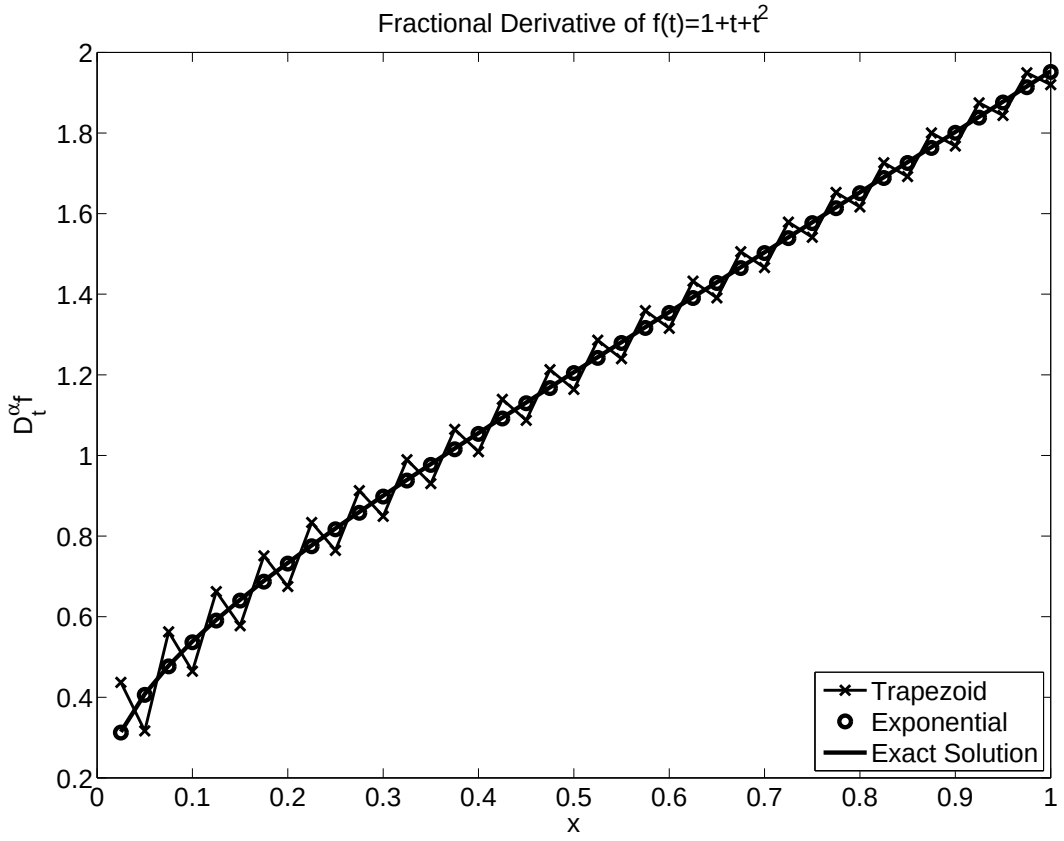

Figure 3.5 The fractional derivative of order $\alpha = 0.65$ for $f_1(t) = 1 + t + t^2$. The oscillations in the trapezoidal rule are noticeable in this instance. Excellent agreement is achieved using the exponential differences method.

The trapezoidal rule requires that the largest quantity $y_j h$ be small in order to resolve the stiffness. But since the smallest step size in our computations is $h = 9 \times 10^{-5}$, and largest exponential is $y_N \approx 10^6$, it is clear that the stiffness is not adequately resolved. Consequently, the trapezoidal rule produces oscillatory behavior in the solution shown in Figure 3.5; but notice that such oscillations do not present themselves in the case $f(t) = t^3$ in Figure 3.7, which is used to demonstrate convergence in [11]. In fact, the convergence indicated in Figure 3.8 shows second order convergence for this function, but only first order convergence for $f(t) = 1+t+t^2$ in Figure 3.6. The slower convergence is due to the oscillations, which result from the the asymptotic behavior of d_j in equation (3.29) for large y_j; that is, $d_j \approx -1$. The

corresponding auxiliary variables ϕ_j will thus become nothing more than spurious modes of oscillation which pollute the numerical solution. Their amplitude will be determined by the size of $\dot{f}(t)$, which is the right hand side for the ODEs (3.27). Over the first few time steps, the derivative of $f(t) = t^3$ is $O(h^2)$, so that the oscillations are initially small, and will in fact remain small for substantially longer times. Thus the oscillations do not present themselves when $f(t)$ is chosen so that its first few derivatives near $t = 0$ are small; that is, when $f(t)$ is sufficiently flat.

This flatness condition is violated for the trial function $f(t) = 1+t+t^2$, which has an $O(1)$ derivative over the first few time steps. For such functions, the stimulation of the spurious oscillatory modes is unavoidable. Consequently, the trapezoidal rule

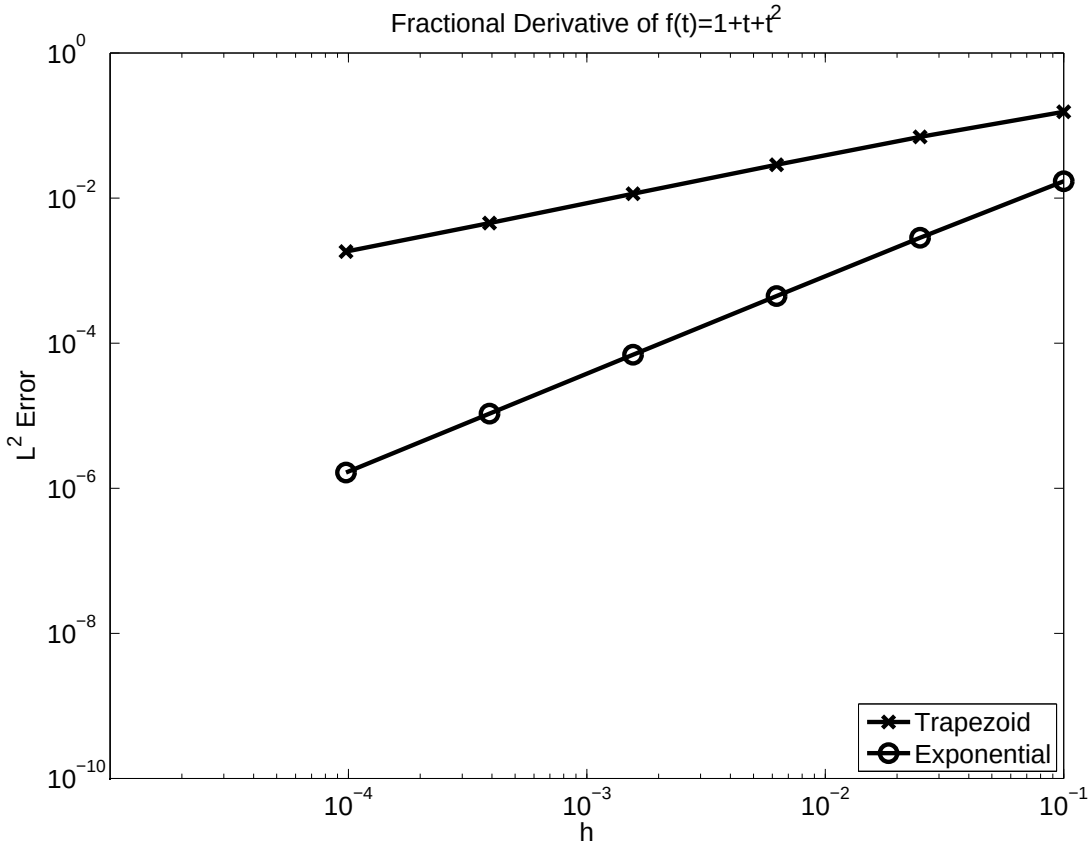

Figure 3.6 L^2 convergence for $f_1(t) = 1 + t + t^2$. The Trapezoidal rule gives 1st order convergence, but the exponential differences method gives convergence of order $2 - \alpha$.

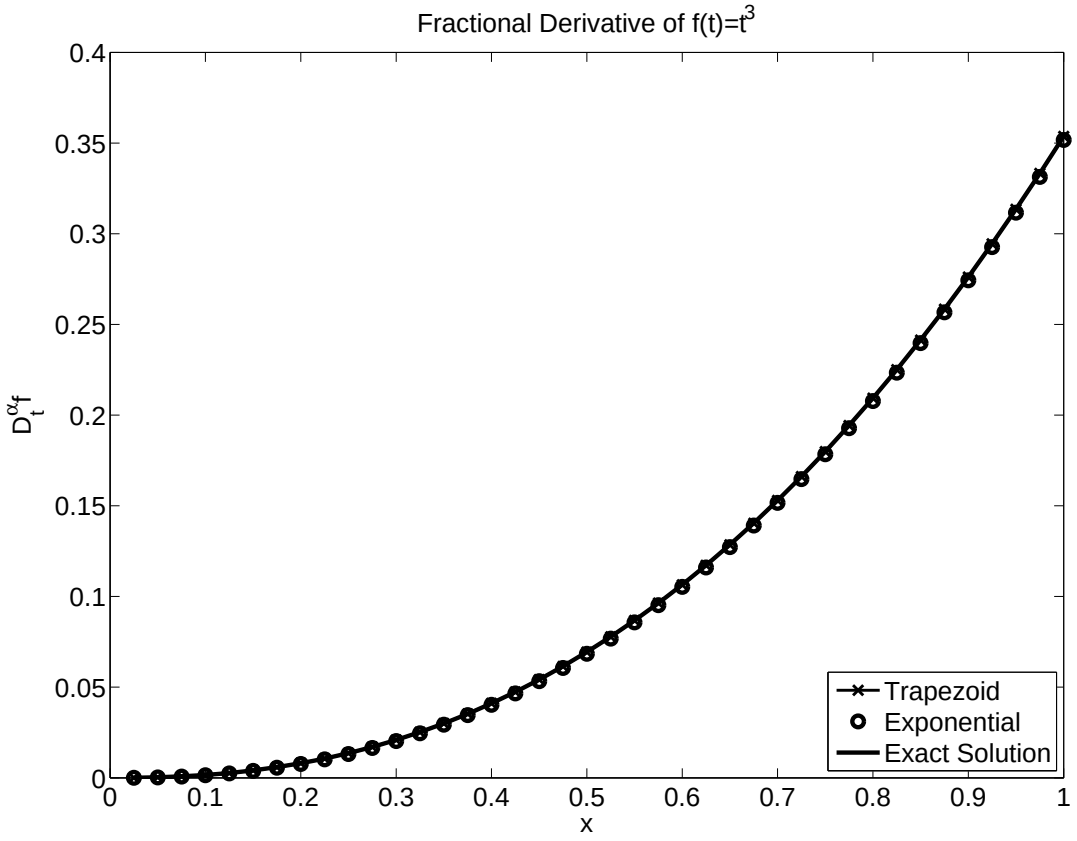

Figure 3.7 The fractional derivative of order $\alpha = 0.65$ for $f_2(t) = t^3$. The oscillations in the trapezoidal rule in are not present in this case, but the same agreement is achieved for the exponential differences method.

is only useful when $f(t)$ is sufficiently flat near the origin, since only then can the relatively strict condition on the time step, namely that $y_N h \ll 1$, be relaxed.

In contrast, the exponential differences method produces convergence of order $2 - \alpha$ for both trial functions. The oscillations observed in the trapezoidal rule will not present themselves here, since the asymptotic limit for large y_j produces $d_j \to 0$, rather than -1. To explain this phenomenon, we compare the coefficients in equations (3.28) and (3.30) with the recurrence relation (3.26). Notice that in the case of exponential differences the choice of d_j is exact, and therefore preserves the asymptotic properties of the true solution for large y_j. For this reason, no spurious oscillations present themselves in the numerical solutions, despite the fact that the

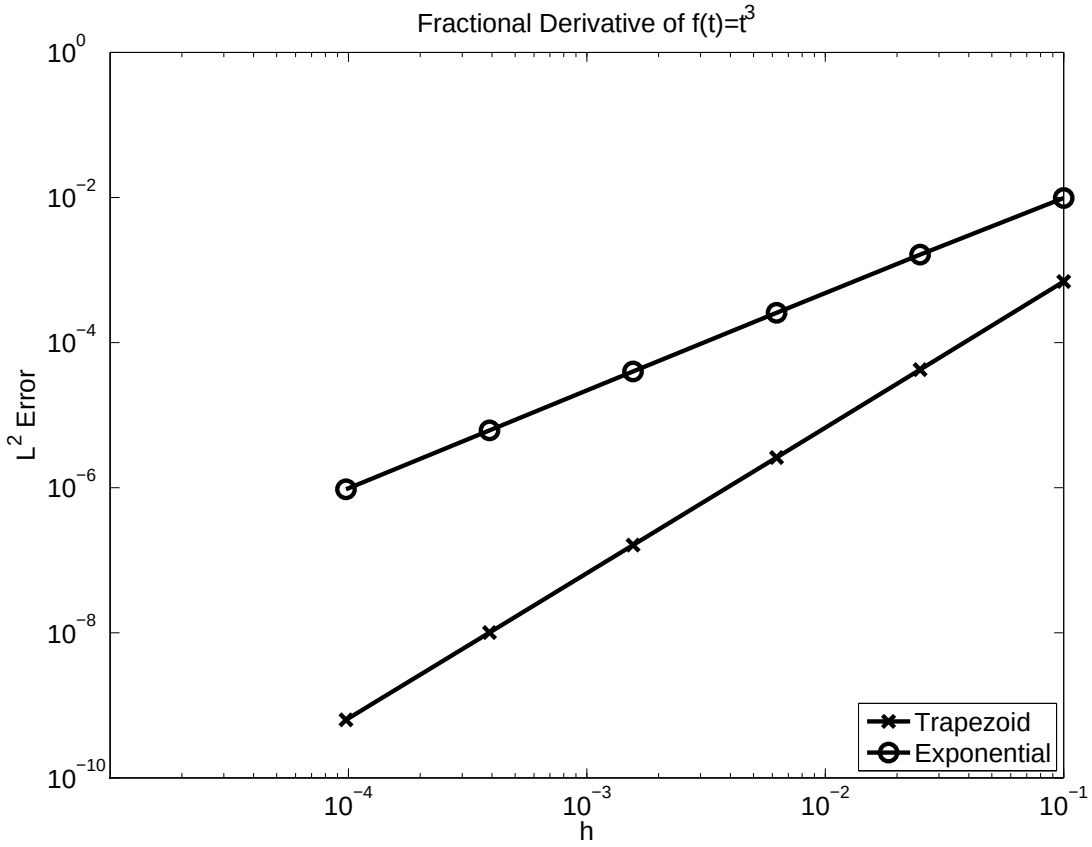

Figure 3.8 L^2 convergence for $f_2(t) = t^3$. The Trapezoidal rule gives 2nd order convergence, but the exponential differences method gives convergence of order $2-\alpha$.

step size is not sufficient to resolve the stiffness. Notice that this is true regardless of the function $f(t)$. This makes the use of exponential differences preferable to the trapezoidal rule in approximating the fractional derivative.

3.4.1 Approximation with $q = 1, 2$

Despite its advantages, the convergence of order $2 - \alpha$ in the exponential differences method is rather slow. We will now use the $q = 1, 2$ methods to compute the numerical fractional derivative of the same functions (3.63).

The fractional derivative for the same two functions, with the same parameters shown in Figures (3.5) and (3.7) respectively, were computed numerically using this

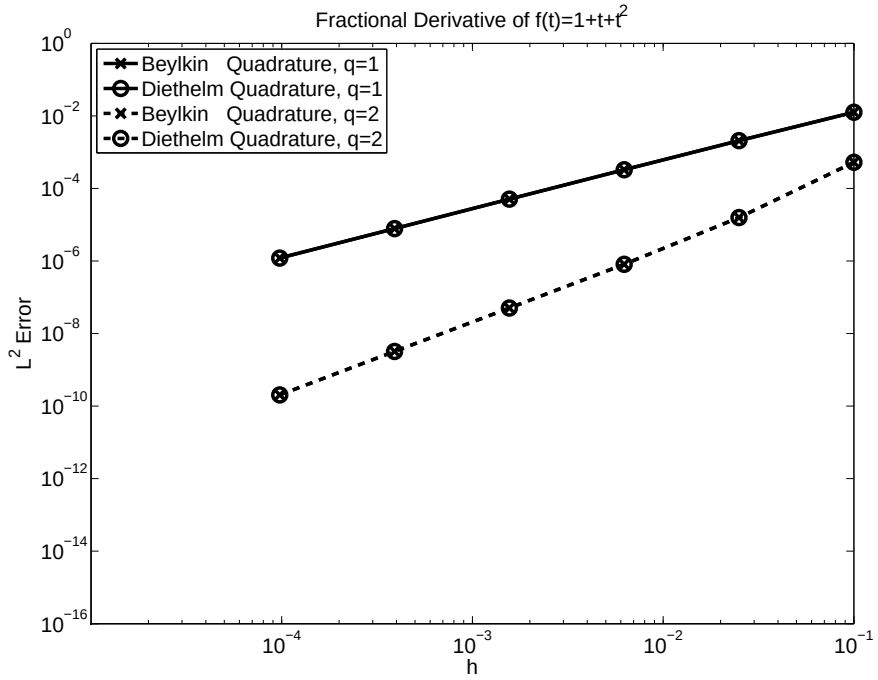

Figure 3.9 Second order convergence is achieved for the $q = 2$ method. The $q = 1$ method exhibits convergence of order $2 - \alpha$.

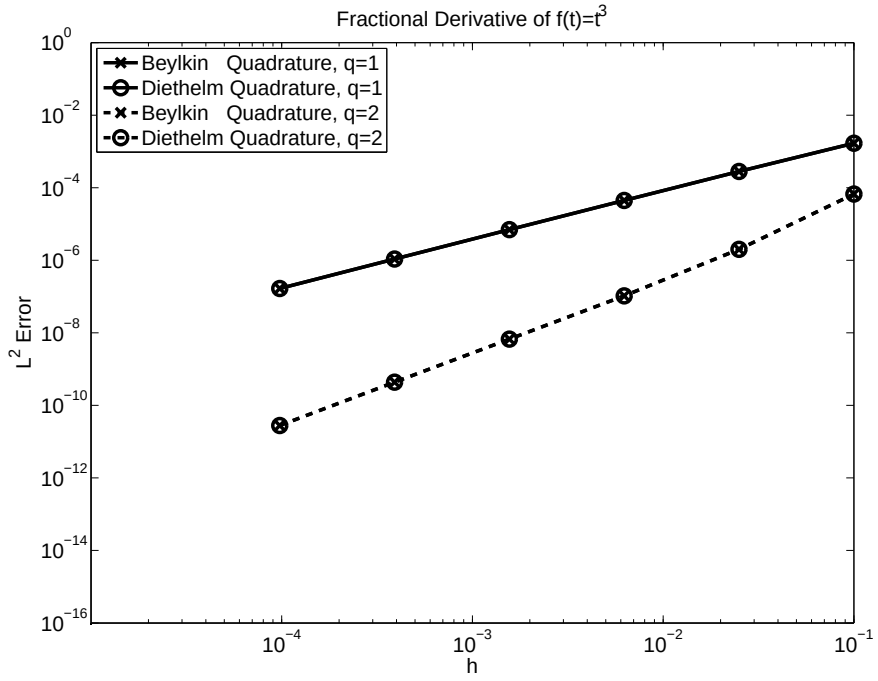

Figure 3.10 Second order convergence is achieved for the $q = 2$ method. The $q = 1$ method exhibits convergence of order $2 - \alpha$.

method. The L^2 convergence is shown in Figures 3.9 and 3.10. For comparison, the best two methods for computing the sum of exponentials from Figure 3.4 are shown. For both functions, the $q = 1$ method shows convergence of order $2 - \alpha$, whereas the $q = 2$ method gives second order convergence.

3.4.2 Relationship with Fractional Integrals

A more recent work by Li [25] has also presented a method for calculating fractional integrals that is closely related to those presented here. The construction therein gives a quadrature with Q points, where Q is $O((\log \frac{1}{\epsilon} + \log \frac{1}{\Delta t})^2)$. Notice that this is an order of magnitude larger than N as indicated in equation (3.44). The main difference is that Li's construction is valid for all time. For comparison, we show in Figures 3.11 and 3.12 the error in approximating the kernel with the exponential method due to Beylkin for two values of α. These constructions are valid for the prescribed precision $\epsilon = 10^{-6}$ over successively larger time intervals. The right plot is the most demanding value of α shown in [25], due to the slow decay of the kernel. The approximations with $N = 52$ and $N = 73$ are valid up to times $t = 10^{10}$ and $t = 10^{15}$, respectively. At time $t = 10^{60}$, the function which is being approximated has decreased below the prescribed tolerance level, so that the absolute error cannot be larger; and so increasing N beyond 369 would be unnecessary. It is noteworthy that before reduction of nodes, our algorithm found $N_0 = 422$ nodes necessary to initialize the quadrature, in complete agreement with Li's bound. While it is an interesting prospect to think of computing a solution up to such a time, it is not practical. Furthermore, it is clear that by imposing the prescribed accuracy up to some finite time T rather than $T = \infty$, the number of quadrature points can be reduced by an order of magnitude (perhaps several). When we also take into account that the storage for the fractional integral is $O(N)$ and the computational complexity

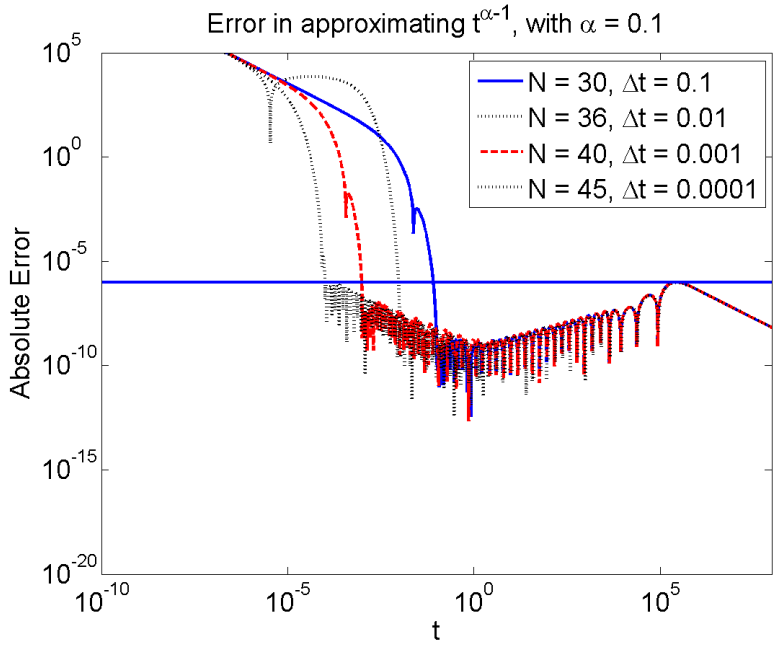

Figure 3.11 The absolute error in approximating $t^{\alpha-1}/\Gamma(\alpha)$, with $\alpha = 0.1$. The prescribed precision is $\epsilon = 10^{-6}$. The time step $\Delta t = 10^{-4}$ is used for the construction. Eventually the function decreases below the precision level, and no more nodes are required.

is $O(NN_t)$ after N_t time steps, we see that reducing the quadrature inherently makes the algorithm more efficient.

To demonstrate this further, we solve the fractional integral problem for the same function used in [25]

$$f(t) = \frac{t}{1+t} + \sin(16.3t) + t^{\alpha} + t^{2\alpha} + t^{1+\alpha} + t^{2+2\alpha}, \tag{3.65}$$

and construct the L^2 error for the minimal number of quadrature nodes in Figure 3.13. Upon setting $N = 25$, the error behaves as depicted in the $p = 2$ case in Figure 4 of [25]; but if N is decreased to 24, the quadrature error dominates the truncation error as Δt decreases. Hence, for a fixed time interval the approximation can be made with far fewer nodes, and without affecting the overall accuracy.

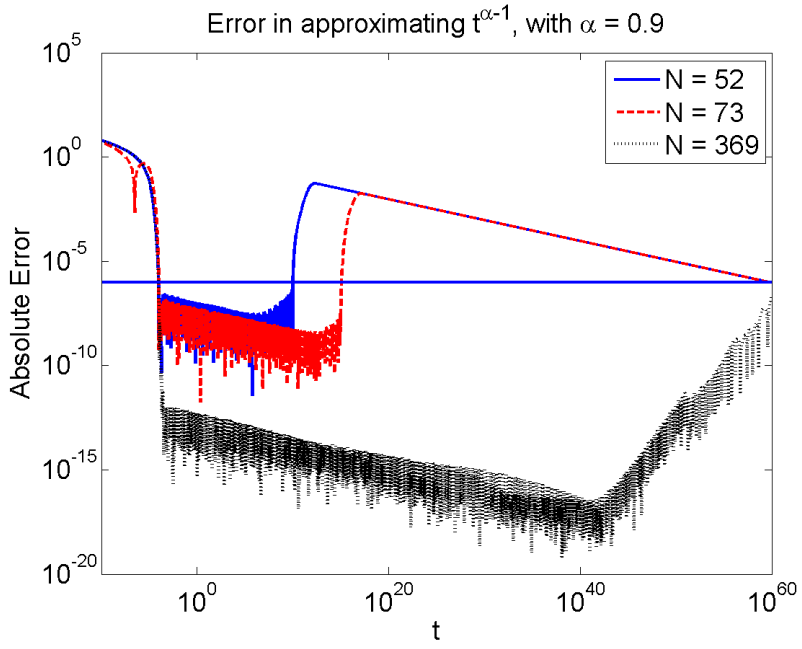

Figure 3.12 The absolute error in approximating $t^{\alpha-1}/\Gamma(\alpha)$, with $\alpha = 0.9$. The prescribed precision is $\epsilon = 10^{-6}$. The time step $\Delta t = 10^{-4}$ is used for the construction. Eventually the function decreases below the precision level, and no more nodes are required.

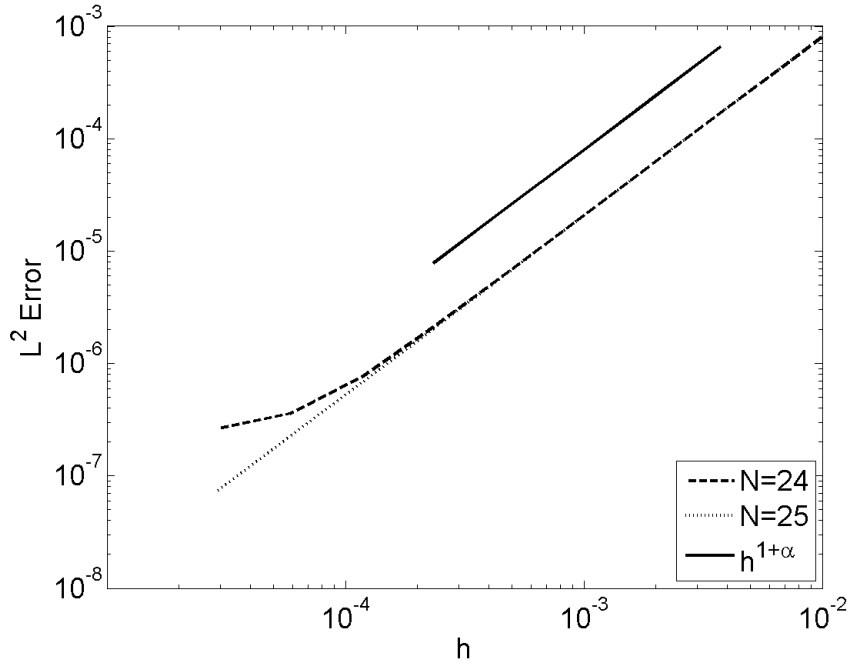

Figure 3.13 Error in approximating the fractional integral of (3.65) with a small number of nodes.

3.5 FD-TD Implementation

We now proceed with a construction of FD-TD method for the Cole-Cole model. Before discretization of equations (1.2), we non-dimensionalize by introducing the scaled variables

$$E' = \frac{1}{\sqrt{\epsilon_0}}E, \quad P' = \sqrt{\epsilon_0}P, \quad H' = \frac{1}{\sqrt{\mu_0}}H, \quad t' = \frac{t}{T_p}, \quad x' = \frac{\sqrt{\epsilon_0\mu_0}}{T_p}x. \tag{3.66}$$

The natural choice for the time scaling parameter would be $T_p = \tau$, which would eliminate the appearance of $\tau' = \tau/T_p$ below; this is in fact what is done for our simulations. Nonetheless we retain τ' to provide a more general presentation of the model, which is applicable when $T_p \neq \tau$. Maxwell's equations are discretized in time and space according to a standard Yee scheme; let $E_m^n = E(m\Delta x, n\Delta t)$, and similarly define the magnetic and polarization field. Inserting the scaled variables (3.66) and dropping the primes, we have

$$\begin{aligned} \frac{1}{\Delta t}\left(H_{m+\frac{1}{2}}^{n+\frac{1}{2}} - H_{m+\frac{1}{2}}^{n-\frac{1}{2}}\right) &= \frac{1}{\Delta x}\left(E_{m+1}^n - E_m^n\right), \\ \frac{1}{\Delta t}\left(\epsilon_\infty(E_m^{n+1} - E_m^n) + P_m^{n+1} - P_m^n\right) &= \frac{1}{\Delta x}\left(H_{m+\frac{1}{2}}^{n+\frac{1}{2}} - H_{m-\frac{1}{2}}^{n+\frac{1}{2}}\right) \\ \tau^\alpha \left(D_t^\alpha P\right)_m^{n+1} + P_m^{n+1} &= (\epsilon_s - \epsilon_\infty)E_m^{n+1}. \end{aligned} \tag{3.67}$$

The dimensionless infinite frequency speed $c_\infty = 1/\sqrt{\epsilon_\infty}$ defines the CFL number $\nu = c_\infty \frac{\Delta t}{\Delta x}$. The discretization of the polarization law (3.4) is performed at $t = (n+1)\Delta t$, which is consistent with our treatment in Section 3.2 and will make it possible to determine the fractional derivative in terms of P at the grid points $n\Delta t$.

3.5.1 Stability

In the standard framework, we study the amplification factors of the system by forming the stability polynomial, and determining the location of its roots. For E, P, H, and ϕ_j we make the substitution $(\cdot)_m^n = (\cdot)\, g^n e^{ikm\Delta x}$, and form the characteristic

polynomial. The stability polynomial can be put in the general form:

$$\Phi(g) = (g-1)^2 \left(1 + \frac{r-1}{1+\tau^\alpha \sigma(g)}\right) + 4\nu^2 \sin^2\left(\frac{k\Delta x}{2}\right) g = 0, \tag{3.68}$$

where $\nu = c_\infty \Delta t/\Delta x$ is the CFL number. The fractional derivative approximation is characterized by $\sigma(g)$, and will therefore contain all of the information involving the exponentials, as well as the coefficients (3.20) and (3.23) for $q = 1, 2$ respectively. For the $q = 1$ method, we have

$$\sigma(g) = (g-1)\left(A_0^1 + \sum_{j=1}^{N} \frac{w_j b_j}{g - e^{-y_j \Delta t}}\right), \tag{3.69}$$

with

$$b_j = e^{-y_j \Delta t}(1 - e^{-y_j \Delta t})/(y_j \Delta t), \quad j = 1, 2 \ldots N. \tag{3.70}$$

Similarly, the $q = 2$ method can be written as

$$\sigma(g) = (g-1)\left(A_0^2 - gA_2^2 + \sum_{j=1}^{N} \frac{w_j b_j e^{-y_j \Delta t}}{g - e^{-y_j \Delta t}}\right), \tag{3.71}$$

where we have used the fact that $A_1^2 = -A_0^2 - A_2^2$ to factor out the $(g-1)$ term. The stability polynomial can also be evaluated numerically by forming the corresponding amplification matrix of size $N+2+q$, and finding the eigenvalues for a representative set of parameters. Of the roots, $N+q$ of them remain mostly stationary as the wave number k is varied; the remaining two traverse arcs that stay near (but within) the boundary of the unit circle, beginning at $g = 1$ when $k = 0$, and approaching $g = -1$ for $k = \pi$. When the classical CFL condition $\nu = 1$ is imposed, these two roots will come to rest inside the unit disk, very close to the real $g-$axis.

We show a representative example of the absolute value of the maximum eigenvalue, with $r = 75$, $h = 10^{-3}$, and $\alpha = 0.75$ for the $q = 1$ method. Notice that when the classical CFL condition $\nu = 1$ is prescribed, the maximum eigenvalue is

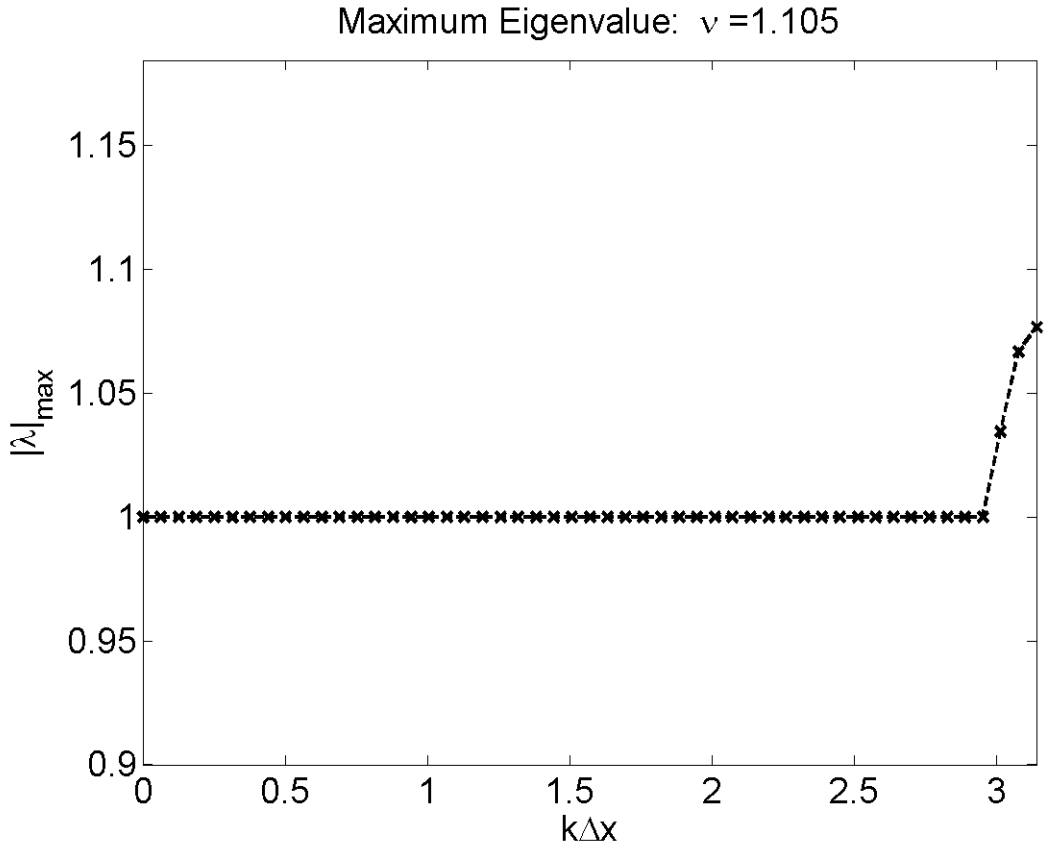

Figure 3.14 Instability is demonstrated for the $q = 1$ case when the numerical CFL condition (3.72) is violated. The pertinent parameters are $r = 75$, $h = 10^{-3}$ and $\alpha = 0.75$.

always 1; this corresponds to the approximate eigenvalue $e^{-y_1 \Delta t} \approx 1$, which is for all practical purposes independent of the wavenumber. Given this behavior, the important properties of the stability factor are determined in a neighborhood of $g = -1$, when we allow $z = \nu \sin\left(\frac{k\Delta x}{2}\right)$ to exceed unity. We can therefore determine the approximate stability condition for the numerical scheme by evaluating $\sigma(-1)$, and treating the rest of the polynomial, which is now quadratic and therefore easy to examine. Applying the Schur criterion [4], we have the following two approximate stability conditions

$$\nu^2 \leq 1 + \frac{r-1}{1 + 2(A_0^1 + \rho_1)}, \quad \rho_1 = \sum_{j=1}^{N} \frac{w_j b_j}{1 + e^{-y_j \Delta t}}. \tag{3.72}$$

Table 3.1 Validation of Stability Conditions Given by Equations (3.72) and (3.73).

	q=1		q=2	
h	$\nu_{Predicted}$	ν_{Actual}	$\nu_{Predicted}$	ν_{Actual}
.001	1.0812	1.1013	1.0610	1.0601
.0001	1.0149	1.0188	1.0111	1.0112
.00001	1.0027	1.0034	1.0020	1.0020

when $q = 1$; and analogously for $q = 2$ the stability condition is

$$\nu^2 \leq 1 + \frac{r-1}{1 + 2(A_0^2 + A_2^2 + \rho_2)}, \quad \rho_2 = \sum_{j=1}^{N} \frac{w_j b_j e^{-y_j \Delta t}}{1 + e^{-y_j \Delta t}}. \tag{3.73}$$

Both of these conditions can be put into a simpler form, with the right hand sides replaced with $1+c_q(r-1)h^\alpha$, with c_q and $O(1)$ constant. These approximate conditions are validated in Table 3.1, where the predicted bounds from (3.72) and (3.73) is computed for different values of h, holding all other parameters fixed. The actual value ν is that for which the maximum eigenvalue of the amplification factor exceeds 1. The parameters used in Figure 3.14 are retained. Both cases predict the actual instability quite well, but the $q = 2$ case provides markedly excellent agreement.

Notice that for $g = e^{i\omega\Delta t}$, setting $g = -1$ is equivalent to choosing ω to be the highest frequency resolved by the stepsize Δt. Thus, freezing the fractional derivative $\sigma(g)$ at $g = -1$ is equivalent to evaluating it at the highest frequency that is resolved, and therefore we are examining the infinite-frequency limit of the fractional derivative.

The stability conditions can be reformulated in dimensional quantities; replacing the CFL condition and rearranging, the stability conditions take the form

$$\left(\frac{\Delta x}{\Delta t}\right)^2 \leq \mu_0 \epsilon_0 \left(\epsilon_\infty + \frac{\epsilon_s - \epsilon_\infty}{1 - \sigma(-1)}\right). \tag{3.74}$$

We now see that the right hand side of the expression is the square of the inverse speed of the medium, given in terms of the permittivity. Thus, our approximation is

recovering the numerical approximation of the infinite-frequency wave speed c_∞ in the Cole-Cole medium. The numerical equivalent of this maximum speed is dependent on the step size, and approaches the true limit as $\Delta t \to 0$; this can be seen by noticing that $A_k^q \sim \Delta t^{-\alpha}$, and thus $\sigma(g)$ is singular in this limit. In practice, we prefer to choose a CFL condition which is independent of the stepsize Δt, and indeed taking the limit $\Delta t \to 0$ in equations (3.72) and (3.73) produces the classical choice $\nu \leq 1$. In our numerical simulations, we therefore use $\nu = 1$.

3.5.2 Phase Error

The phase error represents the total error in the system (3.67) for a given spatial Fourier component $k = k(\omega)$. It will be composed of the truncation error due to discretizing the PDEs, as well as the quadrature error in approximating the integral (3.46). We examine the phase error $\Phi_{N,h} = |k_{N,h}/k - 1|$ for a given value of α by varying both N and $h = \Delta t/\tau$, for $\omega \Delta t \leq \pi$. The wave number k is given by

$$k^2 = \omega^2 \mu_0 \epsilon_0 \left(\epsilon_\infty + \frac{\epsilon_s - \epsilon_\infty}{1 + (i\omega\tau)^\alpha} \right) = \left(\frac{\omega}{c_0} \right)^2 (\epsilon_\infty + \hat{\chi}) \,. \tag{3.75}$$

The discretized wave number similarly satisfies

$$\frac{4}{\Delta x^2} \sin^2 \left(\frac{k_{N,h} \Delta x}{2} \right) = \frac{4}{(c_\infty \Delta t)^2} \sin^2 \left(\frac{\omega \Delta t}{2} \right) \left(1 + \frac{r-1}{1 + \sigma(\omega)\tau^\alpha} \right), \tag{3.76}$$

where the term $\sigma(\omega) \approx (i\omega)^\alpha$ is the approximation to the fractional derivative, as shown in the stability analysis, but now with $g = e^{i\omega\Delta t}$. We construct the approximation for $q = 1$,

$$\sigma(\omega) = \left(1 - e^{-i\omega\Delta t}\right) \left(A_0^1 + \sum_{j=1}^{N} \frac{w_j b_j e^{-i\omega\Delta t}}{1 - e^{-(y_j + i\omega)\Delta t}} \right), \tag{3.77}$$

whereas when $q = 2$ we have

$$\sigma(\omega) = \left(1 - e^{-i\omega\Delta t}\right) \left(A_0^2 - A_2^2 e^{-i\omega\Delta t} + \sum_{j=1}^{N} \frac{w_j b_j e^{-(y_j + i\omega)\Delta t}}{1 - e^{-(y_j + i\omega)\Delta t}} \right). \tag{3.78}$$

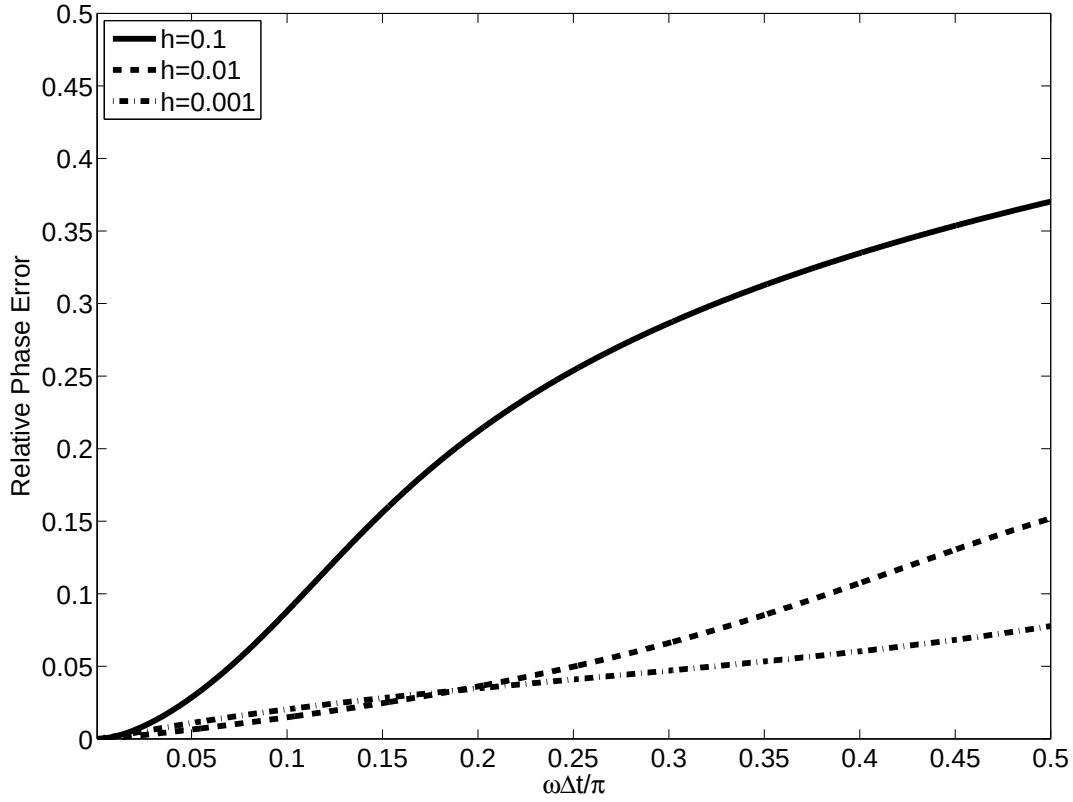

Figure 3.15 Phase error for the two methods, with $q = 1$. Here we have taken $\alpha = 0.75, \tau = 1, \epsilon_s = 75$, and $\epsilon_\infty = 1$.

As in the stability analysis, we have again made use of the fact that $A_1^2 = -A_0^2 - A_2^2$ to eliminate one of the coefficients. These two methods are compared for a representative set of parameters ($\alpha = 0.75, \epsilon_s = 75, \epsilon_\infty = 1, \tau = 1$) in Figures 3.15 and 3.16.

The same quadrature nodes and weights are used for both q methods. Note that for relatively large time step sizes, the $q = 1$ method performs nominally better than the more accurate $q = 2$ methods. This will also be shown in our FD-TD validation. The order of the phase error can be determined by careful observation of the terms appearing in the fractional derivative. First, note that

$$b_j = e^{-y_j \Delta t} \frac{1 - e^{-y_j \Delta t}}{y_j \Delta t} = \frac{e^{-y_j \Delta t}}{\Delta t} \int_0^{\Delta t} e^{-y_j u} du, \quad j = 1, 2, \ldots N, \tag{3.79}$$

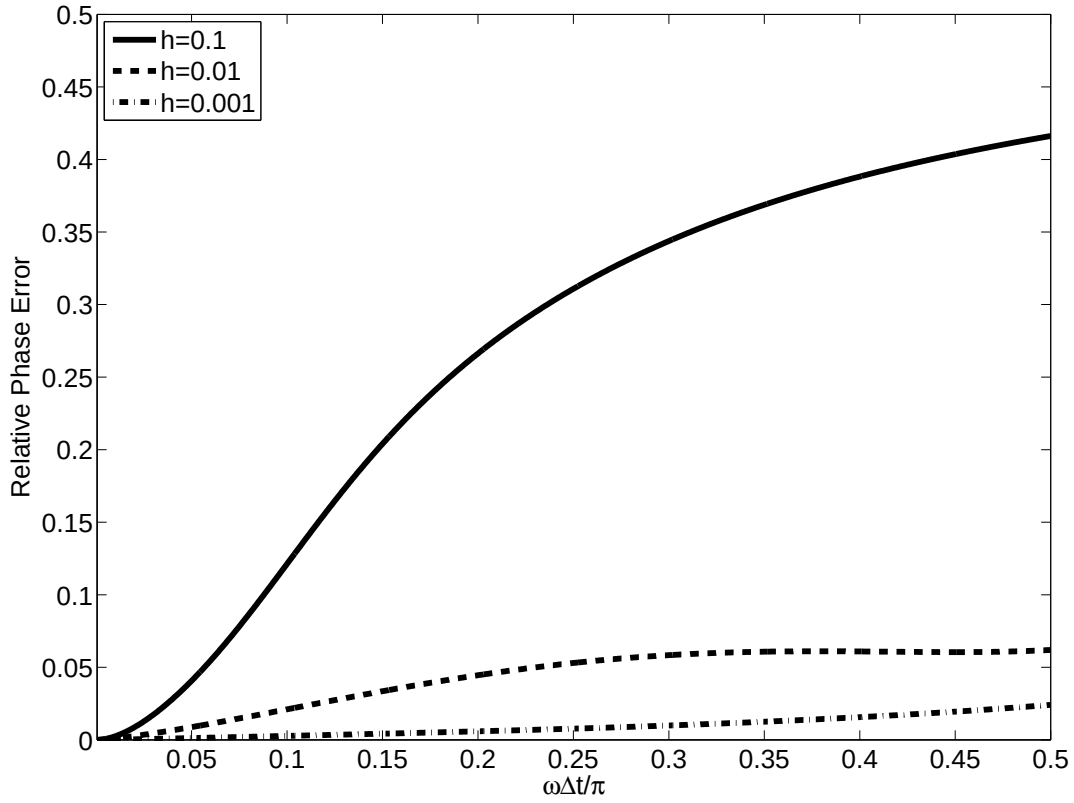

Figure 3.16 Phase error for the two methods, with $q = 2$. Here we have taken $\alpha = 0.75, \tau = 1, \epsilon_s = 75$, and $\epsilon_\infty = 1$.

and that according to equation (3.9), the sums involving exponentials will satisfy

$$\sum_{j=1}^{N} w_j e^{-y_j \Delta t} = \frac{\Delta t^{-\alpha}}{\Gamma(1-\alpha)} \tag{3.80}$$

with a small error ϵ. The denominator of $\sigma(\omega)$ can be expanded as an infinite series, and with the definition of A_0^1 and b_j, we have (for $q = 1$)

$$\begin{aligned}
\sigma(\omega) &= \frac{1 - e^{-i\omega\Delta t}}{\Delta t} \left(\frac{\Delta t^{1-\alpha}}{\Gamma(2-\alpha)} + \sum_{n=0}^{\infty} \sum_{j=1}^{N} w_j \int_0^{\Delta t} e^{-(n+1)(y_j + i\omega)\Delta t - y_j u} du \right) \\
&= \frac{1 - e^{-i\omega\Delta t}}{\Delta t} \left(\frac{\Delta t^{1-\alpha}}{\Gamma(2-\alpha)} + \sum_{n=1}^{\infty} e^{-ni\omega\Delta t} \int_{n\Delta t}^{(n+1)\Delta t} \sum_{j=1}^{N} w_j e^{-y_j u} du \right) \\
&= \frac{1 - e^{-i\omega\Delta t}}{\Delta t} \sum_{n=0}^{\infty} e^{-ni\omega\Delta t} \int_{n\Delta t}^{(n+1)\Delta t} \frac{u^{-\alpha}}{\Gamma(1-\alpha)},
\end{aligned} \tag{3.81}$$

where in the final step, we have used the fact that A_0^1 is clearly the $n = 0$ contribution to the summand. This final approximation is precisely the Fourier transform of the fractional derivative kernel, with a second order error, which follows from

$$\frac{1 - e^{-i\omega\Delta t}}{\Delta t} e^{-ni\omega\Delta t} = e^{-i\omega u} + O((\omega\Delta t)^2), \quad n\Delta t \leq u \leq (n+1)\Delta t. \tag{3.82}$$

An analogous argument is made for the $q = 2$ case, but with the first two terms of the summand coming from the local expansion coefficients A_0^2, A_1^2, A_2^2. Thus, we have

$$\sigma(\omega) = (i\omega)^\alpha + O((\omega\Delta t)^2), \tag{3.83}$$

and substitution into the phase shows that the phase error will also be second order in both cases.

3.6 Numerical Validation

The solution to the system (3.67) was computed for the time signaling problem for various values of α and $h = \frac{\Delta t}{\tau}$; the remaining parameters are fixed and scaled according to (3.66), so that $\epsilon_s = 75, \epsilon_\infty = 1, \tau = 1$ and the CFL condition is $\nu = 1$. Notice this also fixes the dimensionless speeds to be $c_\infty = 1$, $c_s = 1/\sqrt{75}$ in the infinite and zero frequency limits respectively.

The electric field was prescribed at $x = 0$ by a unit impulse of duration $t_d = \tau = 1$ and amplitude $1/t_d = 1$. The resulting time trace was recorded at a few spatial locations to observe its evolution. The simulation is ended prior to the signal reaching the right-hand boundary, so that no reflection is recorded. Representative solutions are shown in Figures 3.17, 3.19 and 3.21 for $\alpha = 0.6$ and 0.75, at short, medium and large depths respectively into the material. The solution was carried out to time $T = 250\tau$, and a depth of $L = 20c_\infty\tau$. The solutions shown were computed using the $q = 2$ method and Beylkin's quadrature, and the exact solution is given by using the Laplace transform method of Chapter 2.

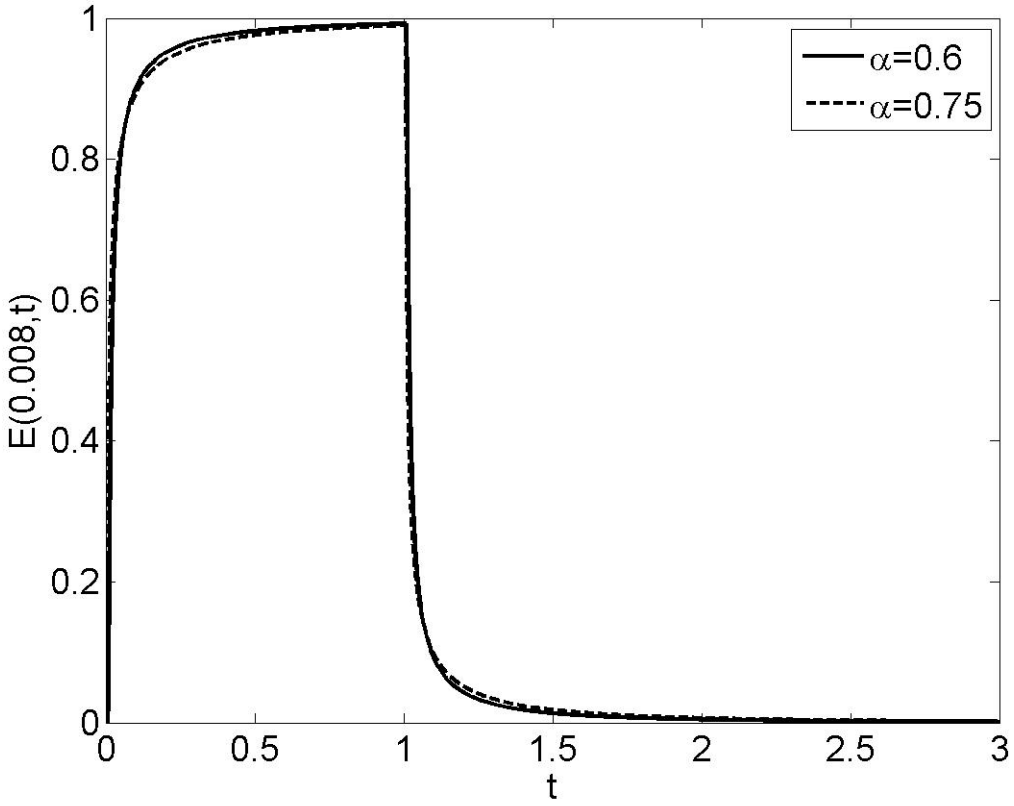

Figure 3.17 Plot of the electric field due to a step pulse of duration $t_d = \tau$, at a depth $x = 0.008 c_\infty \tau$. In the skin-depth, the initial waveform is prevalent, but smoothing has already begun. The value of α has little effect here.

For short depths, the transient nature of the waveform is observed, which still resembles the initial square pulse that was introduced at the air-medium interface. As predicted in Section 2.2, the initial discontinuities of the square wave are immediately removed due to the smoothing nature of the fractional operator.

Beyond the skin depth the transient nature of the pulse fades, and the pulse propagates at sub-characteristic speed c_s. The peak value of the electric field arrives slightly before the time determined by the sub-characteristic ray $t = x/c_s$ for $\alpha < 1$, as predicted.

The L^2 relative error $||E_{exact} - E||/||E_{exact}||$ is then computed over time. For comparison, the error is shown in Figures 3.17, 3.19 and 3.21 for the $q = 1$ and $q = 2$

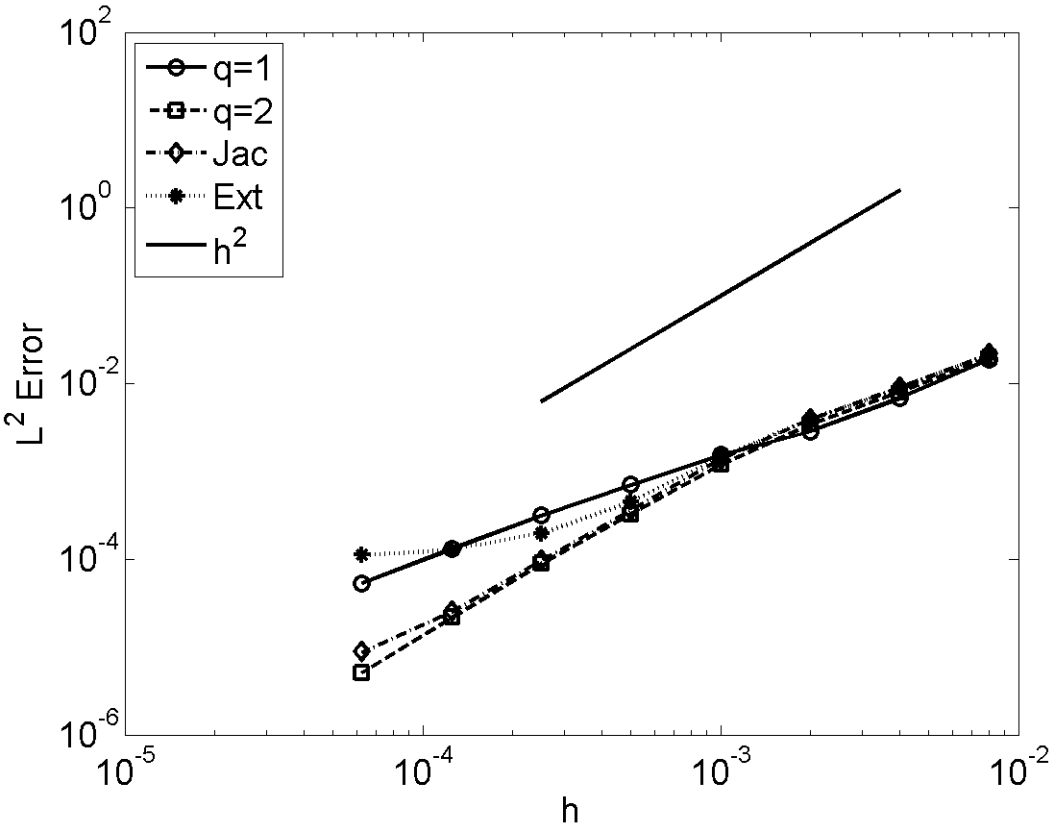

Figure 3.18 L^2-Error corresponding to Figure 3.17.

methods at short, medium and large spatial depths. The quadrature is designed for each case to satisfy $\epsilon = O(h^{q+1})$ ensure that the error due to approximating the fractional derivative does not exceed the truncation error. Additionally, we have also computed the solution using the trapezoidal rule, neglecting the local contributions ($q = 0$), using Diethelm's Jacobi ('Jac' in the error plots) method with $N = 20$, and the extraction method ('Ext') of Lu and Hanyga with $N = 50$.

For short depths, the expected order of convergence is achieved as h is reduced, but surprisingly the $q = 1$ method performs slightly better for larger h. The same is true for larger depths, but even more noticeably. The order of convergence is as expected; first order for $q = 1$ and second for $q = 2$. Perhaps more surprising is the second order convergence of the 'Jac' and 'Ext' methods, which do not contain

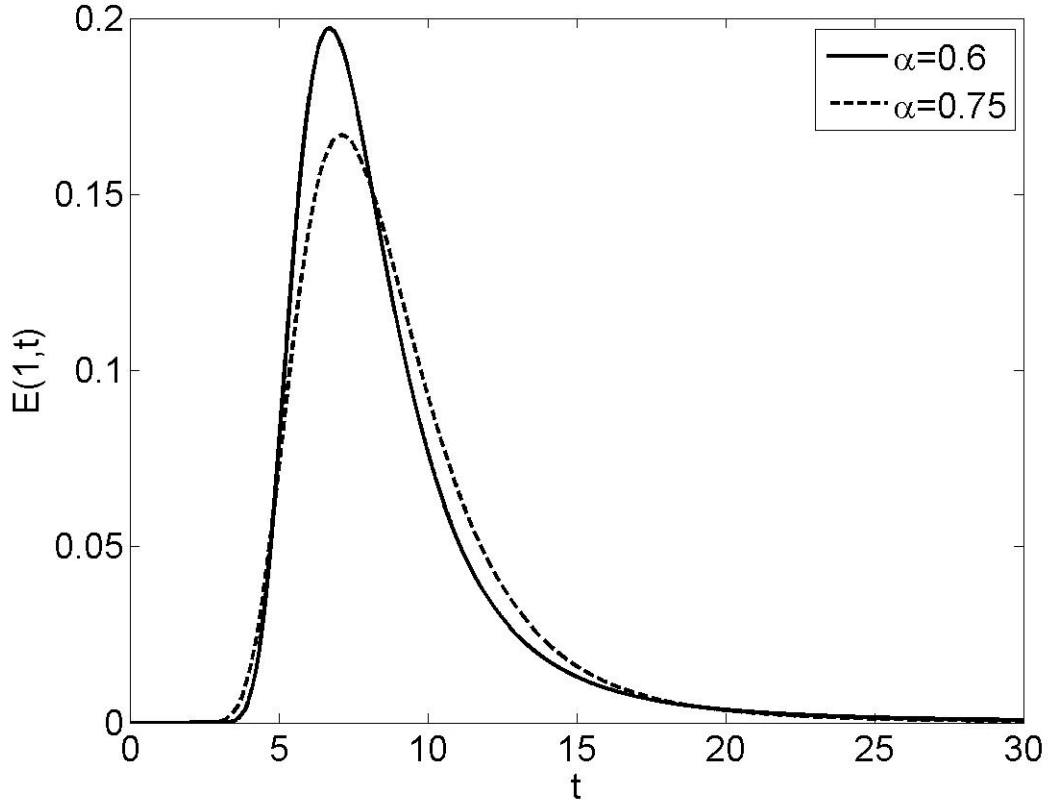

Figure 3.19 Plot of the electric field due to a step pulse of duration $t_d = \tau$, at a depth $x = c_\infty \tau$. The transition region between the skin depth and the bulk medium shows rapid attenuation. The transient behavior of the waveform is rapidly diminishing, and the characteristic pulse due to the material response is becoming apparent.

a local approximation of the fractional derivative (thus, they are $q = 0$ methods). The quadrature error in the Jacobi method is dominated by the discretization error, and is therefore less than $O(\Delta t^2)$ for $\Delta t \geq 3.125 \times 10^{-5}$, even with 20 nodes; this is far better than predicted by Figure 3.4. By comparison, the 'Ext' method with $N = 50$ can be seen to be dominated by quadrature error as Δt is reduced in Figure 3.20. The numerical evidence suggests that the fractional derivative can be accurately approximated for a sufficiently accurate quadrature rule, without the special treatment at the singularity given by the new q methods presented here (i.e., with a straightforward application of the trapezoidal rule). It must be noted however

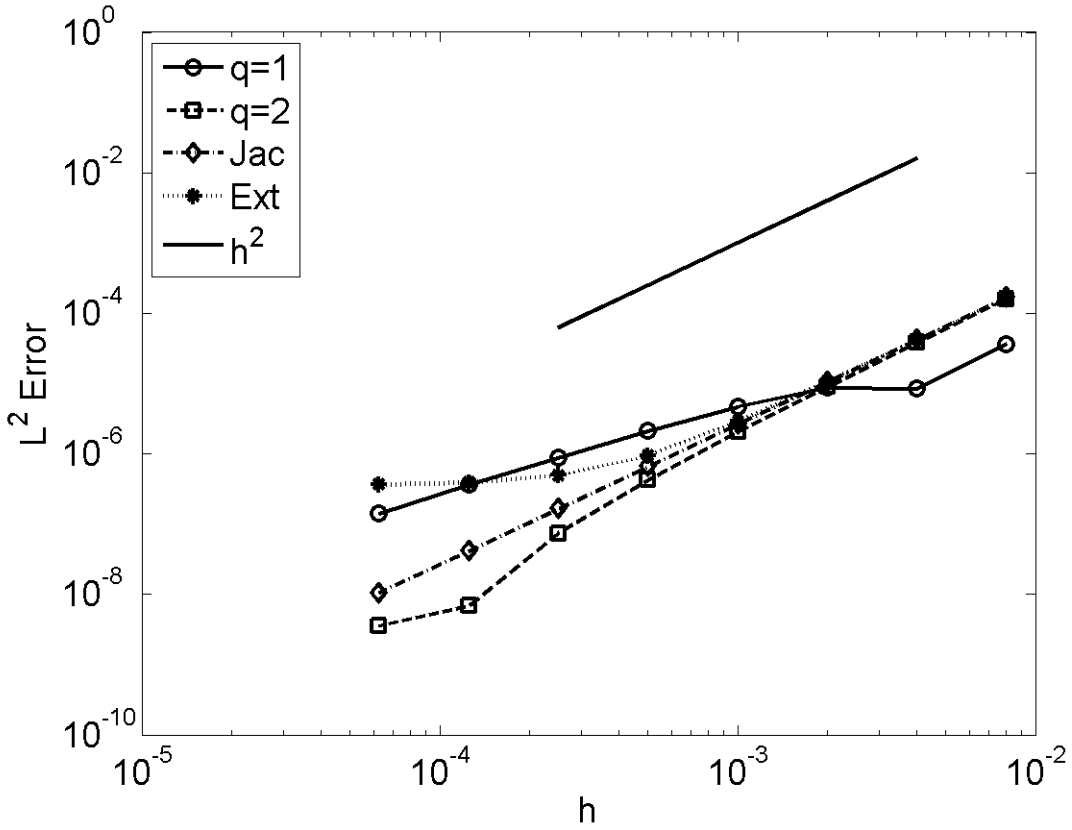

Figure 3.20 L^2-Error corresponding to Figure 3.19.

that the $q = 2$ method does outperform all other methods uniformly by a noticeable margin at all spatial depths.

3.7 Conclusion

In the present work, we have implemented and analyzed a numerical scheme that computes the propagation of an incident electromagnetic pulse through a medium described by the Cole-Cole dielectric model using standard FDTD methods. We present numerical schemes for $q = 1$ and 2, which are convergent of order 1 and 2 respectively, both of which preserve the CFL condition; this latter result holds for similar methods such as [26], [37], [36], which were shown to be equivalent to our $q = 1$ method, but with a different choice of exponentials. The numerical results suggest

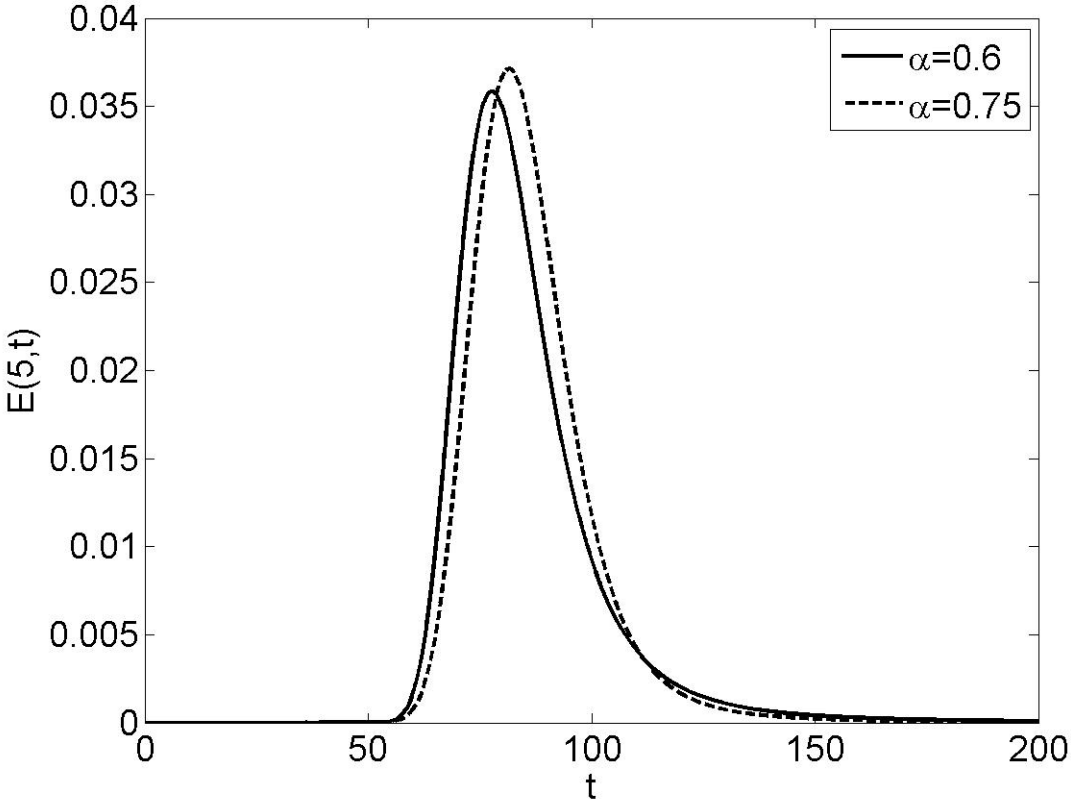

Figure 3.21 Plot of the electric field due to a step pulse of duration $t_d = \tau$, at a depth $x = 5c_\infty\tau$. The waveform is now determined by the medium parameters. For the two solutions depicted, all parameters are held fixed except α, which can be seen to to affect the pulse symmetry, and duration of the tail.

that a $q = 0$ implementation, which omits special treatment of the singularity in the fractional derivative, yields second order results as well, although with a marginally larger error than the $q = 2$ method. As will be shown in Chapter 4, the polarization can also be formulated as a convolution with the electric field, which will also be shown to be second order accurate.

Several methods of discretizing the fractional derivative were investigated. The most efficient of these are the sum of exponentials construction presented in [3], and the Gauss-Jacobi quadrature of [11]. However only in the former method is there a relationship which makes it possible to choose the appropriate number of exponentials.

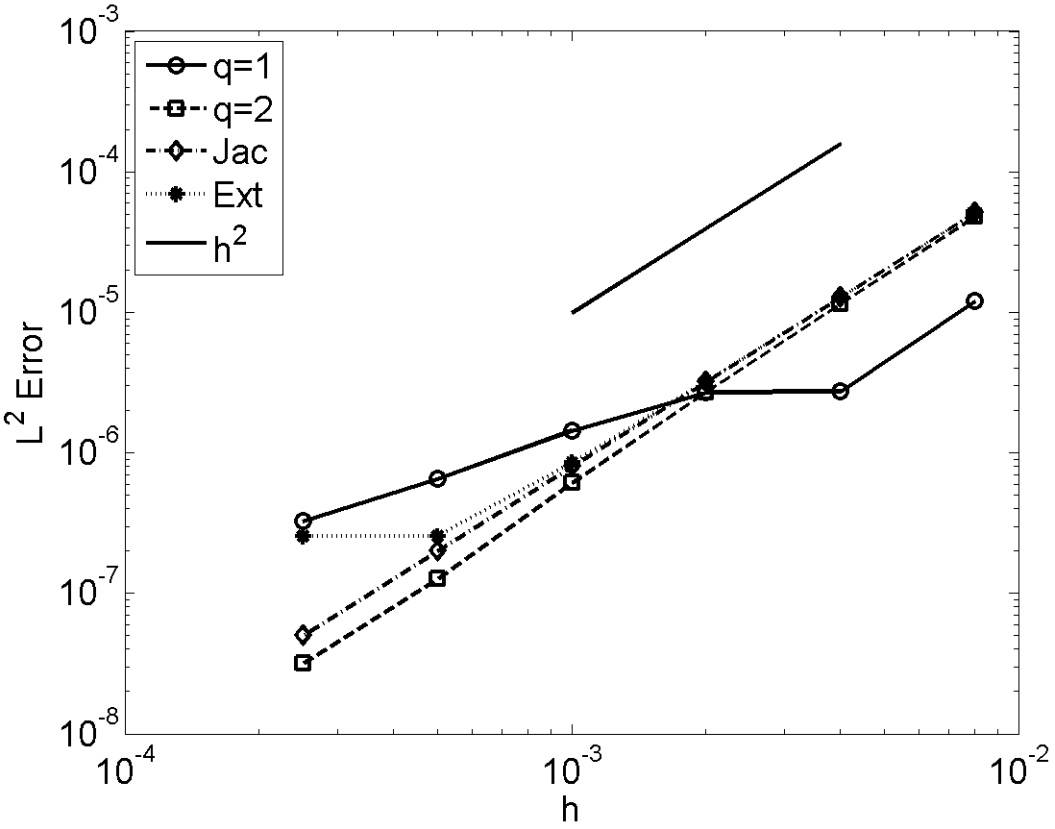

Figure 3.22 L^2-Error corresponding to Figure 3.19.

Given a tolerance ϵ, and a number of timesteps N_t, the number of exponentials is $N = O(\log 1/\epsilon + \log N_t)$.

CHAPTER 4

THE HAVRILIAK-NEGAMI DIELECTRIC MODEL

4.1 Introduction

As was mentioned previously, the discussion in Chapter 3 for the C-C model cannot be extended to the FDTD method for the H-N model. Recently, a procedure to approximate the H-N dielectric with exponentials in the time domain has been presented in the literature [22]. This work presents an approximation of the H-N dielectric model by Debye functions (poles) in the frequency domain with a preset accuracy over a specified band of frequencies. Therefore the overall scheme possesses the stability and accuracy properties of the schemes typically used to implement the Debye dielectric model in the FD-TD scheme [28]. However, the accuracy in the time domain, particularly over a given computational duration $t \in [0, T]$, will be unknown. Furthermore, the polarization dynamics are not accurately represented in the time-domain, as the singularity of the time-domain susceptibility that arises from dielectric models with fractional relaxation is not taken into account. Consequently, the ability to compute the impulse or step response of spatially complex dispersive scatterers is lost.

It appears that there would be great utility in being able to implement the H-N dielectric model in a way that offers the modeler the ability to perform time-domain simulations over a specified time interval $[0, T]$ while maintaining both a preset accuracy for the polarization dynamics and the stability and accuracy attributes of the FD-TD method. Also, it would be desirable that the implementation does not depend on the values of α and β thus eliminating the need for separate codes when considering the H-N model's subclasses in the FD-TD method.

Although the Debye case ($\alpha \to 1^-,\ \beta = 1$) is a singular limit of the H-N model, and thus our approach presented below does not include it, we offer a work-around this shortcoming in the Summary Section 6. Finally, it should be emphasized that it is desirable that the implementation of the polarization dynamics of the H-N model be correct at $t \to 0^+$ in order to allow the modeler to compute the impulse- or step-response response of a spatially complex time-dispersive object directly in the time-domain for the purpose of storing the obtained results at desired spatial locations and later using them to compute the response of the object to arbitrary incident pulses without recomputing with the FD-TD method.

In Section 4.2 of the chapter we present an approach that approximates the induced polarization dynamics of the H-N model with a preset accuracy over an arbitrary (but a priori known) computational time interval $[0, T]$. We show our method correctly captures both the short- and long-time behavior of the corresponding time-domain susceptibility. The conventional approach to convolution requires $O(N)$ storage, where N is the number of time steps, so that longer computations become progressively restrictive due to memory allocation. In the development of our method we employ the efficient numerical techniques of [20], [2] to drastically reduce the required storage from $O(N)$ to $O(\log N)$ in order to compute a convolution and solve the H-N model as a system of $M = \log N$ evolution equations appended to the Maxwell system which requires only the information from the previous time step to perform an update. In Sections 4.3.1 and 4.3.2 we show our scheme preserves the second order convergence and the CFL stability condition of the FD-TD method. We close the chapter with numerical validations and experiments in Section 4.4 and a short summary and discussion in Section 4.5.

4.2 Numerical Approximation of the Polarization Law

We now present the FD-TD implementation for the H-N model by considering the same signaling problem as in Chapter 3. As before, we proceed by first scaling the space, time and field variables

$$E \to \sqrt{\epsilon_0}E, \quad P \to \frac{1}{\sqrt{\epsilon_0}}P, \quad H \to \sqrt{\mu_0}H, \quad t \to T_p t, \quad x \to \frac{T_p}{\sqrt{\epsilon_0\mu_0}}x, \tag{4.1}$$

where the time scale T_p is usually (but not necessarily) chosen to be the dielectric model central relaxation time τ. Maxwell's equations are again

$$\frac{\partial H}{\partial t} = \frac{\partial E}{\partial x}, \tag{4.2}$$

$$\frac{\partial}{\partial t}\left(\epsilon_\infty E + P\right) = \frac{\partial H}{\partial x}, \tag{4.3}$$

but we will now appeal to the definition of the induced polarization (1.6)

$$P(x,t) = \int_0^t \chi(t-t')E(x,t')dt'; \quad t > 0. \tag{4.4}$$

The susceptibility $\chi(t)$ expresses the induced polarization dynamics and for the H-N model it is obtained as the inverse Laplace transform

$$\begin{aligned}
\chi(t) =& \mathcal{L}^{-1}\left\{\frac{\epsilon_s - \epsilon_\infty}{\left(1+(s\tau)^\alpha\right)^\beta}\right\} \\
=& \frac{\Delta\epsilon}{2\pi i}\int_{\zeta-i\infty}^{\zeta+i\infty}\frac{e^{st}}{\left(1+(s\tau)^\alpha\right)^\beta}ds \\
=& \frac{\Delta\epsilon}{\pi\tau}\int_0^\infty \frac{\sin\left(\beta\theta(y)\right)e^{-yt/\tau}}{\left(y^{2\alpha}+2\cos\left(\pi\alpha\right)y^\alpha+1\right)^{\beta/2}}dy,
\end{aligned} \tag{4.5}$$

with $\theta(y) \in [0, \pi\alpha]$ given by

$$\theta = \cos^{-1}\left\{\frac{y^\alpha\cos\left(\pi\alpha\right)+1}{\sqrt{y^{2\alpha}+2\cos\left(\pi\alpha\right)y^\alpha+1}}\right\}. \tag{4.6}$$

It is worth noting that in current literature, the angle θ is defined using the arctangent, which is only valid for $\theta < \pi/2$, and must therefore be defined piecewise to obtain the

correct angle [43]; the above definition does not require such manual adjustment. In addition, this definition will hold in general for $0 < \alpha < 1$, and is thus valid for both the C-C and H-N models. The C-D model requires a slightly modified treatment; in this case the Bromwich contour used in the inverse Laplace transform is deformed onto the branch cut which is now located along the negative real axis issuing from the branch point at $s = -1/\tau$ rather than at the origin (as in the case of the H-N and C-C models). Furthermore, $\theta \to \pi$, and the denominator can be reduced. We thus obtain the time-domain susceptibility for the C-D model

$$\begin{aligned}\chi(t) &= \frac{\Delta\epsilon}{\pi\tau}\int_1^\infty \frac{\sin(\pi\beta)}{(y-1)^\beta}e^{-yt/\tau}dy \\ &= \frac{\Delta\epsilon}{\pi\tau}\sin(\pi\beta)e^{-t/\tau}\int_0^\infty v^{-\beta}e^{-vt/\tau}dv \\ &= \frac{\Delta\epsilon}{\Gamma(\beta)\tau}\left(\frac{t}{\tau}\right)^{\beta-1}e^{-t/\tau}.\end{aligned} \tag{4.7}$$

Notice that we can directly evaluate the case $\beta = 1$ in this latter expression and recover the Debye case; this could also have been done by observing that in this case the distribution in (4.5) will collapse into a delta function $\delta(t-\tau)$, which ultimately leads to the same result. The integral in equation (4.7) provides implicitly an integral transform for the singular portion of the susceptibility $t^{\beta-1}$; through this relation the C-D model can be similarly treated along with the general H-N model.

Specifically, equations (4.5) and (4.7) comprise a continuous distribution of exponentials; in fact the Debye case is a "distribution" of a single exponential. The nucleus of our method is to replace the susceptibility by an approximation that makes discretization simple, but for which we have an a priori error bound that is uniform over our computation window $t \in [0, T = N\Delta t]$. For FD-TD methods, we will use a uniform grid in time that locates the E and P fields at $t_n = n\Delta t$, $n = 1, 2, \ldots N$.

To motivate our approximation, we obtain the behavior of the susceptibility by expanding the integrand in (4.5) for large and small arguments of the integration

variable y. Doing so provides the leading order behavior for small and large t, respectively in the H-N case; the corresponding result for the C-D model can be obtained from direct examination of the closed form obtained from equation (4.7). The resulting behaviors for small and large time in each model are:

$$\chi \sim \begin{cases} t^{\alpha\beta-1}, & t \to 0; \quad t^{-\alpha-1}, \quad t \to \infty \quad H-N \\ t^{\alpha-1}, & t \to 0; \quad t^{-\alpha-1}, \quad t \to \infty \quad C-C \\ t^{\beta-1}, & t \to 0; \quad e^{-t/\tau}, \quad t \to \infty \quad C-D. \end{cases} \tag{4.8}$$

Recalling that $0 < \alpha, \beta < 1$ it follows that $\chi(t) \in L^1([0,c])$ and $\chi(t) \in L^1([c,\infty]) \cap L^2([c,\infty])$ for $c > 0$. Due to the singularity at $t = 0^+$, we treat the interval $[0, \Delta t]$ separately. Away from $t = 0^+$, $\chi(t)$ is a smooth algebraically decaying function that can be approximated efficiently with a sum of exponentials over a finite interval $[\Delta t, T]$. Therefore, we will represent the induced polarization as a sum of a local and a history part [15],

$$\begin{aligned} P(x,t) &= \int_0^t \chi(t-t')E(x,t')dt' = \int_0^t \chi(t')E(x,t-t')dt' \\ &= \int_0^{\Delta t} \chi(t')E(x,t-t')dt' + \int_{\Delta t}^t \chi(t')E(x,t-t')dt' \\ &= P_{loc}(x,t) + P_{hist}(x,t). \end{aligned} \tag{4.9}$$

4.2.1 Local Approximation

In order to represent the local part P_{loc} of the induced polarization accurately we obtain an asymptotic expansion of the susceptibility χ for the small t, of which the leading order behavior is indicated in (4.8). A simple scaling argument shows that this will correspond to large values of the integration variable s in the first line of equation (4.5). The Laurent expansion of $(1 + (s\tau)^\alpha)^{-\beta}$ is then integrated term by term, resulting in

$$\chi(t) \approx \frac{\Delta\epsilon}{\tau} \sum_{k=0}^{K} \frac{(-1)^k}{\Gamma(\alpha(k+\beta))} \binom{\beta+k-1}{k} \left(\frac{t}{\tau}\right)^{\alpha(k+\beta)-1}, \tag{4.10}$$

where

$$\binom{\beta+k-1}{k} = \frac{\Gamma(\beta+k)}{\Gamma(\beta)\Gamma(k+1)} \tag{4.11}$$

is a generalized binomial coefficient, and the number of terms K to be included can be determined for a preset precision level.

The C-C and C-D models can be obtained by setting β and $\alpha = 1$ respectively; for the C-D model, we can see that the expansion is in fact that of the exponential obtained in (4.7) which is multiplied by the singular term $(t/\tau)^{\beta-1}$, which means that the expression is exact for $K \to \infty$. This is true for the H-N model, since the series in (4.10) can be shown to be absolutely convergent. Since $\chi \in L_1([0, \Delta t])$, if we assume that $E \in L_2([0, \Delta t])$ then the same will hold for the local approximation P_{loc}. We now use linear interpolation to approximate

$$E(x, t - t') \approx E(x, t) + \frac{t'}{\Delta t}\left[E(x, t - \Delta t) - E(x, t)\right] \tag{4.12}$$

which expresses E at the grid points and is second order accurate for $t \in [0, \Delta t]$. The local approximation is then determined to be

$$P^n_{loc} = E^n \left(\int_0^{\Delta t} \left(1 - \frac{t'}{\Delta t}\right) \chi(t') dt' \right) + E^{n-1} \left(\int_0^{\Delta t} \frac{t'}{\Delta t} \chi(t') dt' \right) \tag{4.13}$$

$$= \Delta\epsilon \left(a E^n + b E^{n-1} \right), \tag{4.14}$$

where

$$a = \sum_{k=0}^{K} \frac{(-1)^k}{\Gamma(\alpha(k+\beta)+2)} \binom{\beta+k-1}{k} h^{\alpha(k+\beta)} \tag{4.15}$$

$$b = \sum_{k=0}^{K} \frac{(-1)^k \alpha(k+\beta)}{\Gamma(\alpha(k+\beta)+2)} \binom{\beta+k-1}{k} h^{\alpha(k+\beta)}, \tag{4.16}$$

and $h = \Delta t/\tau$. We have used the shorthand notation $E^n = E(x, n\Delta t)$. Since we must choose Δt small enough to resolve the relaxation time [28], we will have $h < 1$. Furthermore, the coefficients a and b can be also be shown to be absolutely

convergent series. To assess the nature of the coefficients for large k we can use Sterling's approximation generalized for the Gamma function

$$\Gamma(z) = \sqrt{\frac{2\pi}{z}} \left(\frac{z}{e}\right)^z \left(1 + O(z^{-1})\right) \tag{4.17}$$

and the binomial coefficient

$$\binom{z+k}{k} = \frac{k^z}{\Gamma(z+1)} \left(1 + \frac{z(z+1)}{2k} + O(k^{-2})\right). \tag{4.18}$$

The terms in the coefficient b will then be of the form

$$\begin{aligned} b_k =& \frac{\alpha(k+\beta)}{\Gamma(\alpha(k+\beta)+2)} \binom{\beta+k-1}{k} \\ \approx& \frac{\alpha(k+\beta)}{\Gamma(\alpha(k+\beta)+2)} \frac{k^{\beta-1}}{\Gamma(\beta)} \left(1 + \frac{\beta(\beta-1)}{2k}\right) \\ \approx& \left(\alpha(k+\beta)\right) \frac{k^{\beta-1}}{\Gamma(\beta)} \sqrt{\frac{\alpha(k+\beta)+2}{2\pi}} \left(\frac{e}{\alpha(k+\beta)+2}\right)^{\alpha(k+\beta)+2} \\ \approx& \frac{\alpha^{1-\beta}}{\sqrt{2\pi}} \frac{(\alpha k)^{\beta+1/2}}{\Gamma(\beta)} \left(\frac{e}{\alpha k}\right)^{\alpha(k+\beta)+2} \\ \approx& C(\alpha,\beta) \left(\frac{e}{\alpha k}\right)^{\alpha(k+\beta)-\beta+3/2}. \end{aligned} \tag{4.19}$$

In this final expression, $C(\alpha, \beta)$ is independent of K, and is $O(1)$, while the parenthetical term will exhibit exponential decay for $k > e/\alpha$; but since the terms in equation (4.16) are of the form $b_k h^{\alpha(k+\beta)}$ the final term obtained by setting $k = K$ will be sufficiently small for K satisfying $K > he/\alpha$. Upon multiplying the expression (4.19) by $h^{\alpha(K+\beta)}$, we obtain the approximate form of the final term in the sum (4.16), which we set equal to some user-prescribed tolerance δ_K. That is,

$$\delta_K = C(\alpha,\beta) \left(\frac{eh}{\alpha K}\right)^{\alpha(K+\beta)-\beta+3/2} h^{\beta-3/2} = C \left(\frac{eh}{\alpha K}\right)^{\alpha(K+\beta)-\beta+3/2}, \tag{4.20}$$

and upon taking the natural log of both sides we have

$$\log \delta_K = [\alpha K + 3/2 - (1-\alpha)\beta] \log\left(\frac{eh}{\alpha K}\right) + \log C$$
$$\approx \alpha K \log h + O(1). \tag{4.21}$$

The discarded terms involving K assuredly remain small, since we consider $K > he/\alpha$. We can now solve the reduced expression for K by omitting the $O(1)$ terms, resulting in a loose upper bound for the number of terms required for convergence,

$$K = \left\lceil \frac{\log \delta_K}{\alpha \log h} \right\rceil. \tag{4.22}$$

The same bound will hold trivially for a in equation (4.15), since $|a_k| < |b_k|$ for each k. Generally K will be relatively small, and in practice $K < 10$ is sufficient to converge to double precision for any values of $.5 < \alpha, \beta \leq 1$ and $0.0001 < h < 0.01$. It also follows from the restriction on K that fewer terms are required for smaller values of h, and larger α. In the present context, the linear interpolation of the electric field will introduce a second order error, so if we choose $\delta_K < h^2$ we are assured that the local approximation will maintain second order accuracy.

4.2.2 History Approximation

The kernel of the history part in (4.9) is now approximated as follows

$$\left|\left| \chi(t) - \frac{\Delta\epsilon}{\tau} \sum_{j=1}^{M} w_j e^{-y_j t/\tau} \right|\right| < \delta_M, \tag{4.23}$$

where δ_M is again a user-prescribed tolerance, and the norm is defined to be

$$||\cdot|| = \max_{\Delta t \leq t \leq N\Delta t} ||\cdot||. \tag{4.24}$$

The values of the weights and nodes (w_j, y_j) are determined using generalized Gaussian quadrature [20]. Such quadrature weights and nodes can be obtained in several

different ways; Beylkin et. al. has designed a scheme for finding a sum of exponentials approximation for a given function [2]. In that work, it is indicated that for a smooth function (which we have, on $[\Delta t, T]$) the number of nodes can be minimized using the error tolerance, resulting in $M = O(\log 1/\delta_M + \log N)$. Alternatively, if we define $\chi(t)$ by a contour integration we can use the methods originally proposed by Rokhlin et. al. [27]. Finally, one can take the Laplace transform of $\chi(t)$, and use it to find a sum-of-poles approximation, then invert this latter expression.

In the present work, we proceed by making the substitution $y = \tan\theta$ in equation (4.5), which maps the integrand to a finite domain $0 < \theta < \pi/2$; we then find a generalized Gaussian quadrature in the variable θ. Since (4.23) has to be satisfied for all $t \in [\Delta t, N\Delta t]$, we will sample the interval $[\Delta t, N\Delta t]$ by $P >> N$ points t_p $p = 1, \cdots, P$ and force (4.23) to be satisfied at these P discrete points. Recall now that each $\chi(t_p)$ is represented as a finite integral on a fixed interval with different integrand functions (t_p here is acting as a parameter (or index) for these P functions f_p). However, the crucial observation is that these P functions f_p are not linearly independent numerically. Indeed, by performing a SVD on these P functions, there are only about $2M = O(\log 1/\delta_M + \log N)$ linearly independent basis functions g_m, $m = 1, \cdots, 2M$ above the threshold $\delta_M/100$ (In our actual computation, $P = 200,000$, and $2M = 86$). Finally, we apply the generalized Gaussian quadrature [2],[27] on these $2M$ basis functions and obtain a sum-of-exponential approximation with only M nodes and weights. Once the weights and nodes are obtained, we define the history part of the induced polarization

$$P_{hist} = \frac{\Delta\epsilon}{\tau} \int_0^{t-\Delta t} \sum_{j=1}^{M} w_j e^{-y_j(t-t')/\tau} E(x,t')dt' = \sum_{j=1}^{M} w_j \phi_j, \tag{4.25}$$

where the auxiliary functions satisfy a recurrence relation (viz. $t_{n+1} = (n+1)\Delta t$),

$$\begin{aligned}\phi_j^{n+1} =& \frac{\Delta\epsilon}{\tau}\int_0^{n\Delta t} e^{-y_j[(n+1)h-t'/\tau]}E(x,t')dt' \\ =& \frac{\Delta\epsilon}{\tau}e^{-y_j h}\left(\int_0^{(n-1)\Delta t} + \int_{(n-1)\Delta t}^{n\Delta t}\right) e^{-y_j(nh-t'/\tau)}E(x,t')dt' \\ =& e^{-y_j h}\phi_j^n + \frac{\Delta\epsilon}{\tau}e^{-y_j h}\int_0^{\Delta t} e^{-y_j t'/\tau}E(x,n\Delta t - t')dt'.\end{aligned} \tag{4.26}$$

We point out here that while ϕ_j can also be described using differential equations, these equations will be stiff, since typically $y_j \in [10^{-3}, 10^4]$. Similarly for the weights we have $w_j \in [10^{-5}, 10]$; Figure 4.1 shows a typical distribution of weights and nodes that arise in our problem for $T = 300$. Conversely, this method can be equivalently

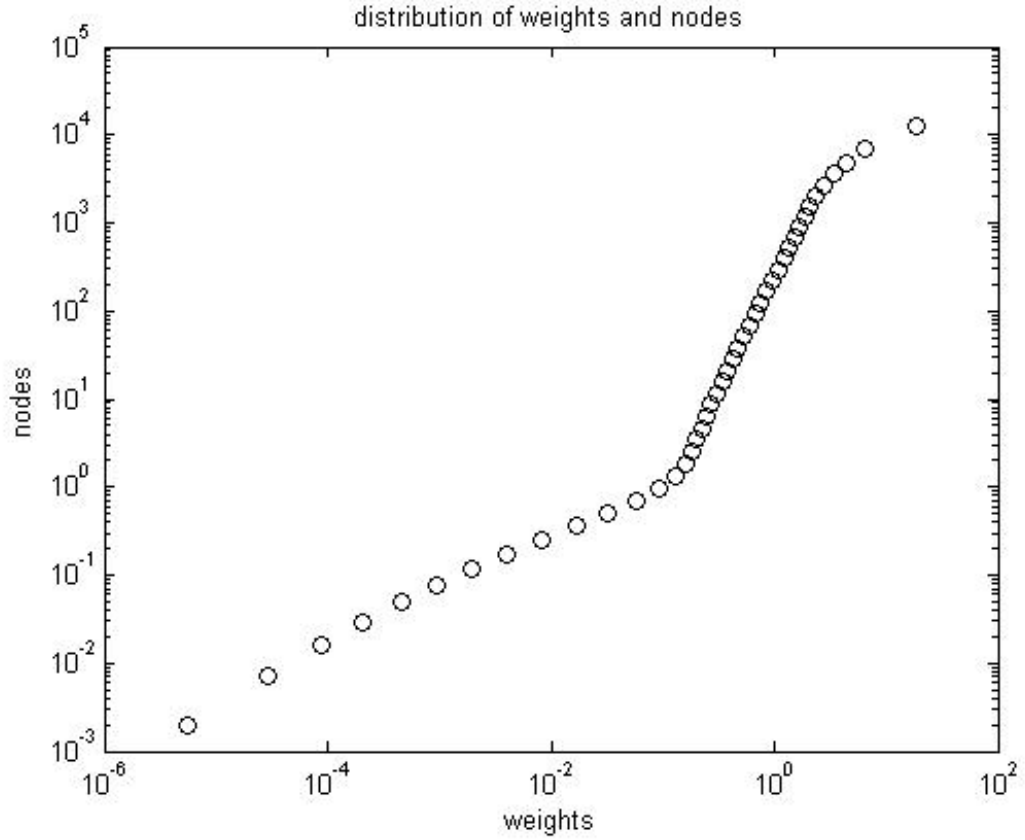

Figure 4.1 A typical distribution of Gaussian weights and nodes for the susceptibility χ. The quadrature is designed using $\Delta t = 5 \times 10^{-4}$, and $\delta_M = 10^{-9}$ for $\alpha = \beta = 0.75$.

derived using exponential time differencing [18]. This final integral can be computed directly if we again approximate E with its linear interpolant across one time step (4.12), which results in

$$\phi_j^{n+1} = e^{-y_j h}\phi_j^n + \Delta\epsilon\left(c_j E^n + d_j E^{n-1}\right), \tag{4.27}$$

from which, after making a substitution $t' = u\tau$, we obtain

$$\begin{aligned} c_j = e^{-y_j h}\int_0^h \left(1-\frac{u}{h}\right)e^{-y_j u}du &= \frac{e^{-y_j h}}{y_j^2 h}\left[\left(e^{-y_j h}-1+y_j h\right)\right], \\ d_j = e^{-y_j h}\int_0^h \frac{u}{h}e^{-y_j u}du &= \frac{e^{-y_j h}}{y_j^2 h}\left[\left(1-e^{-y_j h}(1+y_j h)\right)\right]. \end{aligned} \tag{4.28}$$

4.3 FD-TD Implementation

We now combine the local and history parts of the polarization, to present the full numerical scheme using the staggered space-time mesh of the FD-TD method. We compute E and P at the nodes $(x_m, t_n) = (m\Delta x, n\Delta t)$, and H at the corresponding semi-nodes. This results in the following discrete form of the equations in (4.2),

$$\begin{aligned} \frac{H_{m+1/2}^{n+1/2} - H_{m+1/2}^{n-1/2}}{\Delta t} &= \frac{E_{m+1}^n - E_m^n}{\Delta x}, \\ \epsilon_\infty \frac{E_m^{n+1} - E_m^n}{\Delta t} + \frac{P_m^{n+1} - P_m^n}{\Delta t} &= \frac{H_{m+1/2}^{n+1/2} - H_{m-1/2}^{n+1/2}}{\Delta x}, \end{aligned}$$

which are closed with the discretized induced polarization law (4.4)

$$P_m^{n+1} = \Delta\epsilon\left(aE_m^{n+1} + bE_m^n\right) + \sum_{j=1}^{M} w_j \phi_{jm}^{n+1} \tag{4.29}$$

$$\phi_{jm}^{n+1} = e^{-y_j h}\phi_{jm}^n + \Delta\epsilon\left(c_j E_m^n + d_j E_m^{n-1}\right), \quad j = 1, 2 \ldots M. \tag{4.30}$$

4.3.1 Stability Analysis

We now study the stability of the scheme by constructing the Von Neumann polynomial. Our goal is to determine whether or not the usual CFL stability condition for

the FD-TD method also holds for our scheme. Let

$$(H_m^{n-1/2}, E_m^n, P_m^m, \phi_{1m}^{n+1}, \ldots \phi_{Mm}^{n+1})^T = \vec{U}\rho^n e^{ikm\Delta x}. \tag{4.31}$$

The time index has been shifted for H and $\{\phi_j\}$ for convenience, and will not change the resulting polynomial. Upon substituting into each equation we solve for the characteristic polynomial

$$\Phi(\rho) = \prod_{k=1}^{M} \left(\rho - e^{-y_k h}\right) \left(\Phi_1(\rho) + \frac{\Delta\epsilon}{\epsilon_\infty}\Phi_2(\rho)\right) = 0, \tag{4.32}$$

where

$$\begin{aligned} \Phi_1 =& \rho\left[\rho^2 - 2\left(1 - 2\nu^2 \sin^2\left(\frac{k\Delta x}{2}\right)\right)\rho + 1\right], \\ \Phi_2 =& (\rho-1)^2\left[a\rho + b + \sum_{j=1}^{M} w_j \frac{c_j\rho + d_j}{\rho - e^{-y_j h}}\right], \end{aligned} \tag{4.33}$$

$\nu = c_\infty \Delta t/\Delta x$ is the CFL number, and $c_\infty = 1/\sqrt{\epsilon_\infty \mu_0}$ is the maximum phase velocity in the H-N medium. While Φ_2 is not strictly a polynomial, the denominator terms will cancel when the product is expanded; consequently, $\rho = e^{-y_j h}, j = 1, 2 \ldots M$ will not be eigenvalues of the numerical scheme in general. Although compactly written, $\Phi(\rho)$ is in fact the addition of $M+2$ polynomials of degree $M+3$.

Before characterizing the general behavior of the roots, we first examine a few important limiting cases. When $\Delta\epsilon \to 0$, we see that Φ_2 vanishes. Thus, the roots can be determined analytically as

$$\rho = \left\{0, e^{i\xi}, e^{-i\xi}, e^{-y_1 h}, \ldots, e^{-y_M h}\right\}, \tag{4.34}$$

where the substitution $\sin\frac{\xi}{2} = \nu \sin\frac{k\Delta x}{2}$ is used to define the modes of interest. When $\nu > 1$, there will be a wave number k^* for which $\nu \sin\frac{k^*\Delta x}{2} = 1$. For $k > k^*$, ξ will become complex resulting in one of the roots leaving the unit circle; that is, instability.

For $\nu \leq 1$, the roots will both traverse the unit circle from $\rho = 1$ when $k = 0$, and move to $\rho = e^{\pm i\xi^*}$ when $k\Delta x = \pi$, where $\sin\frac{\xi^*}{2} = \nu$. The remaining modes are stationary for all values of $k\Delta x$, and are simple zeros that lie along the positive real axis and will cluster at the origin for larger values of $y_j h$. The polynomial will be a Schur polynomial [34], leading immediately to stability.

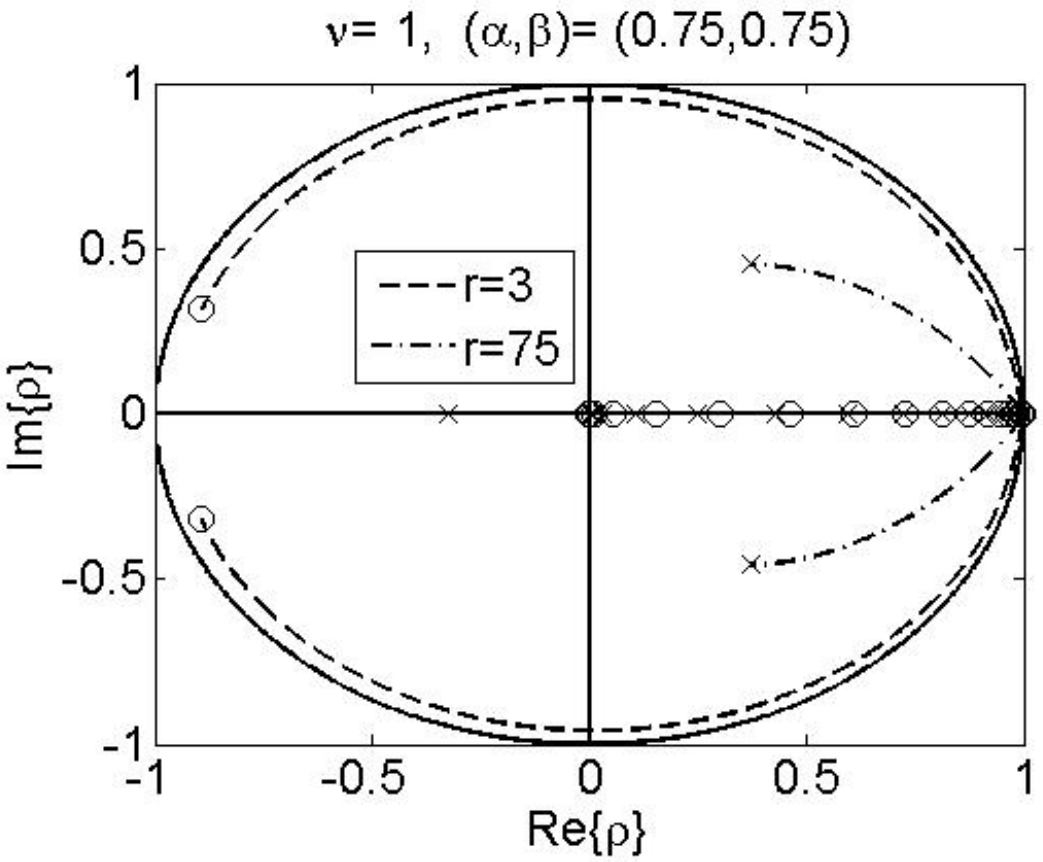

Figure 4.2 Motion of the roots for varying values of $k\Delta x$. When $r = \frac{\epsilon_s}{\epsilon_\infty}$ is small, the roots traverse arcs that approach the unit circle. As r increases, these arcs decrease in magnitude, so the roots always remain inside the unit disk. The values along the real axis remain nearly stationary for all $k\Delta x$, and will not leave the unit disk.

Next we examine the ratio $r = \epsilon_s/\epsilon_\infty \to \infty$; as r becomes large we may neglect Φ_1, but must now deal with a polynomial of degree $M + 3$, where the none of the roots are easily tractable, except the obvious root of multiplicity 2 at $\rho = 1$. Focusing on the remaining polynomial, we wish to think of the roots as being perturbed from

some value that is nearly a root of the polynomial. This happens, for instance when the summation is expanded, and $\rho = e^{-y_\ell h}$ is a zero of all but one of polynomials in the summation. We thus make use of a standard result in perturbation theory [39]:

Consider a polynomial $\Phi(\rho) = f(\rho) + \epsilon g(\rho)$, where ρ_0 is a root of $f(\rho)$ but not of $g(\rho)$. Then, if $\rho(\epsilon) = \rho_0 + \epsilon\rho_1 + \cdots$ is a root of $\Phi(\rho)$, we have $\rho_1 = -g(\rho_0)/f'(\rho_0)$, which is well-behaved if $f'(\rho_0)$ is bounded away from 0. Now for $\rho_0 = e^{-y_\ell h}$

$$\begin{aligned} f &= P_\ell(\rho)\left(a\rho + b + \sum_{j\neq\ell}^{M} w_j \frac{c_j\rho + d_j}{\rho - e^{-y_j h}}\right)(\rho - e^{-y_\ell h}) \\ g &= P_\ell(\rho)(c_\ell\rho + d_\ell) \end{aligned} \tag{4.35}$$

where

$$P_\ell(\rho) = (\rho - 1)^2 \prod_{k\neq\ell}^{M} \left(\rho - e^{-y_k h}\right) \tag{4.36}$$

and $\epsilon = w_\ell$. We can now see that indeed $\rho_0 = e^{-y_\ell h}$ is a root of f but not of g. A simple calculation gives

$$\begin{aligned} g(\rho_0) &= P_\ell(e^{-y_\ell h})\left(c_\ell e^{-y_\ell h} + d_\ell\right) \\ f'(\rho_0) &= P_\ell(e^{-y_\ell h})\left(ae^{-y_\ell h} + b + \sum_{j\neq\ell}^{M} w_j \frac{c_j e^{-y_\ell h} + d_j}{e^{-y_\ell h} - e^{-y_j h}}\right) \end{aligned} \tag{4.37}$$

Thus, $e^{-y_\ell h}$ will be perturbed to first order by an amount

$$\begin{aligned} \rho &= \rho_0 - w_\ell \frac{g(\rho_0)}{f'(\rho_0)} \\ &= e^{-y_\ell h}\left(1 - \frac{w_\ell(c_\ell e^{-y_\ell h} + d_\ell)}{\left(ae^{-y_\ell h} + b + \sum_{j\neq\ell}^{M} w_j \frac{c_j e^{-y_\ell h} + d_j}{e^{-y_\ell h} - e^{-y_j h}}\right)}\right). \end{aligned} \tag{4.38}$$

The second term will always be small and positive. For the weights and nodes corresponding to Figure 4.1, the right term will vary by several orders of magnitude, but remain small as $O(10^{-6}, 10^{-2})$. The larger values of y_j will correspond to a more pronounced contraction from the value ρ_0; for smaller y_j the roots barely change. A

numerical investigation has confirmed these results; for various values of r and $k\Delta x$, the roots all remain on the positive axis and are contained in the unit disk. Similarly, one can show that a root near the origin arises from the coefficients a and b, which will remain on the negative axis, and is bounded below by $-b/a > -1$; as $r \to 1$ ($\Delta\epsilon \to 0$), this root becomes the zero eigenvalue in (4.34).

Finally the double root at $\rho = 1$ will be perturbed and become two complex conjugate roots whose motion is contained in the first and fourth quadrants, respectively. The motion of these roots is illustrated for several values of r in Figure 4.2. Recall, as $r \to \infty$, these roots coalesce at $\rho = 1$, and they will only remain on the unit circle in the case $r = 1$, or equivalently $\Delta\epsilon = 0$. Thus, we have shown that all roots are contained within the unit disk for $\nu \leq 1$, and stability follows immediately.

4.3.2 Phase Error Analysis

In general there will be two sources of error in computing a numerical solution to the system (4.2): the error incurred when approximating the susceptibility $\chi(t)$ for $t \in [0, T = N\Delta t]$, and the typical local truncation error of the FD-TD method. The discretization we presented in Section 4.2 allows full control of the first kind of error that arises from both the local and history part of the polarization law (4.4). This is done by first prescribing the precisions δ_K and δ_M for the local and history portions respectively; then choosing K acording to (4.22) and finding the minimum number of terms M which satisfies (4.23). As long as we set $\delta_K, \delta_M < h^2$ then we are assured that the error introduced over the computational time interval T by the polarization will be smaller than the local truncation error in time for the FD-TD method. The results shown below will hold for the implementation of the H-N, C-C and C-D models.

We study the phase error of our scheme by analyzing the numerical dispersion relation. The numerical wave number $k_h^{K,M}(\omega)$ satisfies

$$\sin^2\left(\frac{k_h^{K,M}\Delta x}{2}\right) = \frac{1}{\nu^2}\sin^2\left(\frac{\omega\Delta t}{2}\right)\left[1+\frac{\Delta\epsilon}{\epsilon_\infty}\hat{\chi}_h^{K,M}(\omega)\right], \tag{4.39}$$

where

$$\hat{\chi}_h^{K,M}(\omega) = \left(a + be^{-i\omega\Delta t} + \sum_{j=1}^{M} w_j \frac{c_j e^{-i\omega\Delta t} + d_j e^{-2i\omega\Delta t}}{1-e^{-(y_j h + i\omega\Delta t)}}\right) \tag{4.40}$$

is the approximate susceptibility, the CFL number is $\nu = c_\infty\Delta t/\Delta x$. Similarly, the

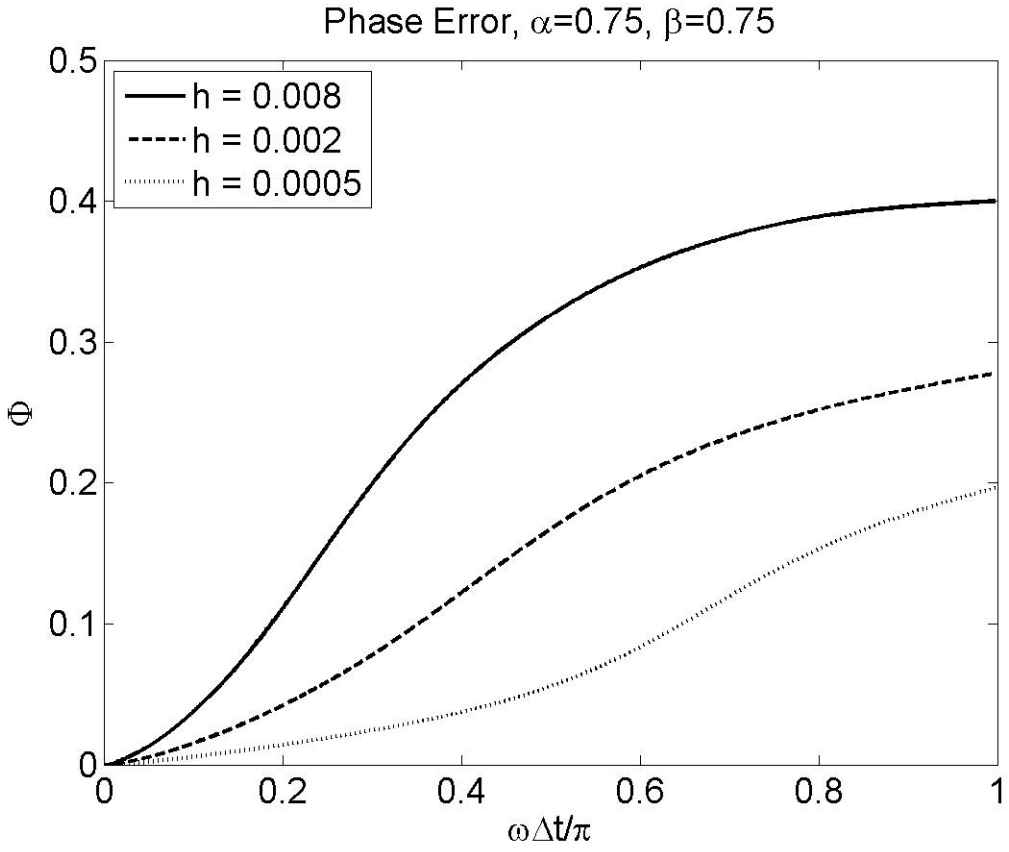

Figure 4.3 The phase error decreases for smaller values of $h = \Delta t/\tau$, which is the dominant source of error made in computing the solution in an H-N medium; that is, the error due to the discretizing the convolution is negligible.

exact dispersion relation is

$$k^2 = \left(\frac{\omega}{c_\infty}\right)^2\left[1+\frac{\Delta\epsilon}{\epsilon_\infty}\hat{\chi}(\omega)\right], \tag{4.41}$$

where

$$\hat{\chi}(\omega) = \frac{1}{(1 + (i\omega\tau)^{\alpha})^{\beta}} \tag{4.42}$$

is the scaled susceptibility (with $\Delta\epsilon = 1$). The phase error $\Phi_h = |k_h^{K,M}/k - 1|$ is plotted for several values of $h = \Delta t/\tau$ in Figures 4.3 and 4.4; the quadrature used in each case is the same, and is designed with $\delta_K = \delta_M = 10^{-9}$ and $\Delta t = 5 \times 10^{-4}$; thus the quadrature should maintain accuracy for $\Delta t \geq 5 \times 10^{-4}$. Figures 4.3 and 4.4 validate this assertion, and show that the error observed is comprised predominantly of the discretization error. If Δt is decreased past the value for which the quadrature

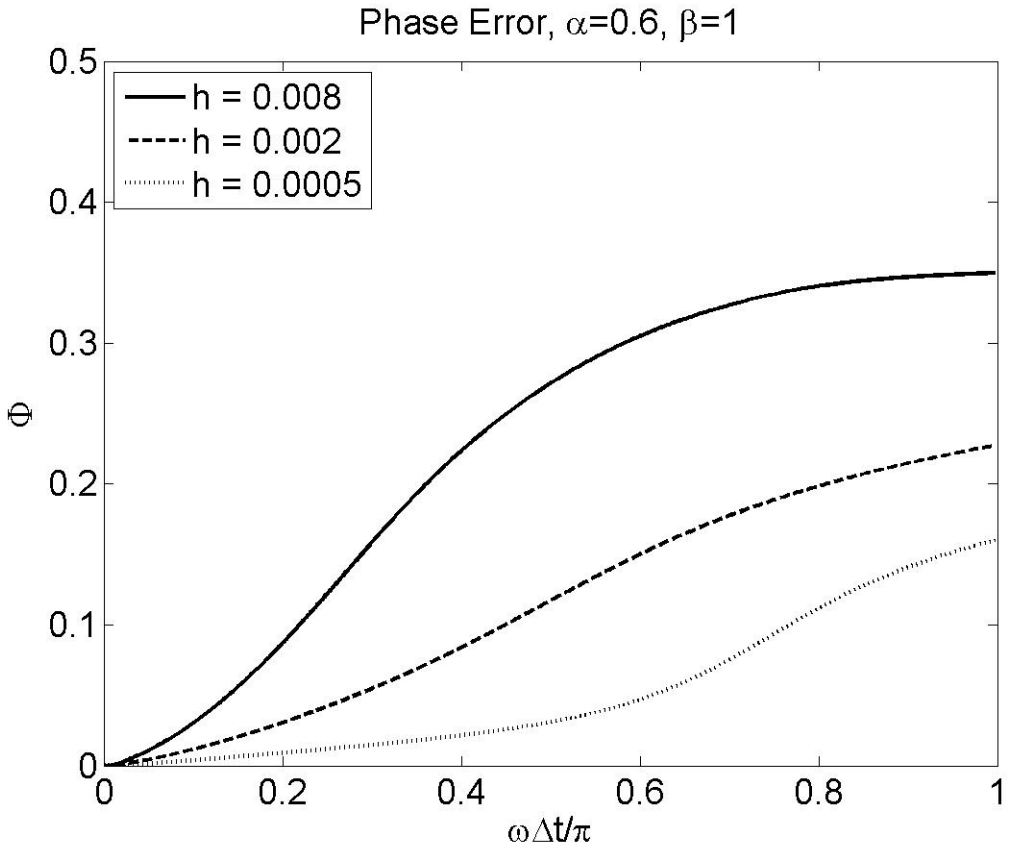

Figure 4.4 The phase error decreases for smaller values of $h = \Delta t/\tau$, which is the dominant source of error made in computing the solution in a C-C medium; that is, the error due to the discretizing the convolution is negligible.

is designed, then the quadrature error will eventually dominate the total error, and further decreasing the step size will not improve the overall accuracy.

We now show the phase error is second-order accurate in Δt and Δx. Using the definitions of a and b in equations (4.15) and (4.16), it can be easily shown that

$$a + be^{-i\omega\Delta t} = \int_0^{\Delta t} \chi(t')L(e^{-i\omega\Delta t})dt' + O(\delta_K + \Delta t^2), \tag{4.43}$$

where $\chi(t)$ is approximated using the small time expansion in (4.10), and

$$L(e^{-i\omega\Delta t}) = 1 + (e^{-i\omega\Delta t} - 1)\frac{t'}{\Delta t} \tag{4.44}$$

is the linear interpolant of $e^{-i\omega t}$ over the interval $[0, \Delta t]$. Similarly, the history portion can be rearranged by invoking the definitions (4.28) of the coefficients, and making use of a geometric series to show that

$$\begin{aligned}
&\sum_{j=1}^{M} w_j \frac{c_j e^{-i\omega\Delta t} + d_j e^{-2i\omega\Delta t}}{1 - e^{-(y_j h + i\omega\Delta t)}} \\
&= \sum_{j=1}^{M} w_j \left(c_j e^{-i\omega\Delta t} + d_j e^{-2i\omega\Delta t}\right) \sum_{n=0}^{\infty} e^{-(y_j nh + i\omega n\Delta t)} \\
&= \sum_{j=1}^{M} w_j \left\{ \int_0^h \left(1 - \frac{u}{h} + \frac{u}{h} e^{-i\omega\Delta t}\right) e^{-(y_j u + i\omega\Delta t)} du \right\} \sum_{n=0}^{\infty} e^{-(y_j nh + i\omega n\Delta t)} \\
&= \int_0^{\Delta t} L\left(e^{-i\omega\Delta t}\right) \sum_{n=0}^{\infty} e^{-i\omega(n+1)\Delta t} \sum_{j=1}^{M} w_j e^{-y_j(nh + t'/\tau)} dt'/\tau \\
&= \sum_{n=1}^{\infty} e^{-i\omega n\Delta t} \int_0^{\Delta t} L(e^{-i\omega\Delta t})\chi(t' + n\Delta t)dt' + O(\delta_M).
\end{aligned} \tag{4.45}$$

Recall that δ_M is the prescribed error used to define the generalized Gaussian nodes, and is therefore the error made in replacing the sum with the true susceptibility. We now make use of the fact that the contribution from a and b in (4.43) is precisely the

$n = 0$ summand, which we combine to obtain

$$\begin{aligned}\hat{\chi}_h^{K,M}(\omega) &\approx \sum_{n=0}^{\infty} e^{-i\omega n\Delta t} \int_0^{\Delta t} L(e^{-i\omega\Delta t})\chi(t' + n\Delta t)dt' + O(\delta_K + \delta_M) \\ &= \sum_{n=0}^{\infty} \int_{n\Delta t}^{(n+1)\Delta t} \chi(t')e^{-i\omega t'}dt' + O(\delta_K + \delta_M + \Delta t^2), \\ &= \int_0^{\infty} \chi(t')e^{-i\omega t'}dt' + O(\Delta t^2), \end{aligned} \tag{4.46}$$

which is immediately recognized as a second order accurate approximation to the Fourier transform $\hat{\chi}$, as is desired. This shows explicitly that for a given choice of $\delta_K, \delta_M < O(\Delta t^2)$, we maintain the second order accuracy of the FD-TD method.

4.4 Numerical Validation

The solution to the system (4.2), (4.4) was computed for signaling data comprised of short and long-duration pulses and for various values of (α, β). The electric field at $x = 0$ is a square impulse of duration $t_d = \tau/100$ (short pulse) or $t_d = \tau$ (long pulse), both with unit area so that the low-frequency spectrum is in agreement. Time traces were recorded at several spatial locations in order to observe the solution. The simulations are terminated prior to the signal reaching the right-hand boundary, so that no reflection is encountered.

We first present a validation of our scheme. In these validations, the exact electric field is calculated independent of the FD-TD scheme, through a numerical evaluation of the inverse Laplace transform, as according to Chapter 2. We must point out here that the exact solution is obtained using different numbers of quadrature points in the inverse Laplace transform, depending on whether a small or large depth solution is sought. The number of quadrature points are increased until a level of accuracy that is better than that of the FD-TD scheme is achieved, so that for all practical purposes, we may call these computations "exact".

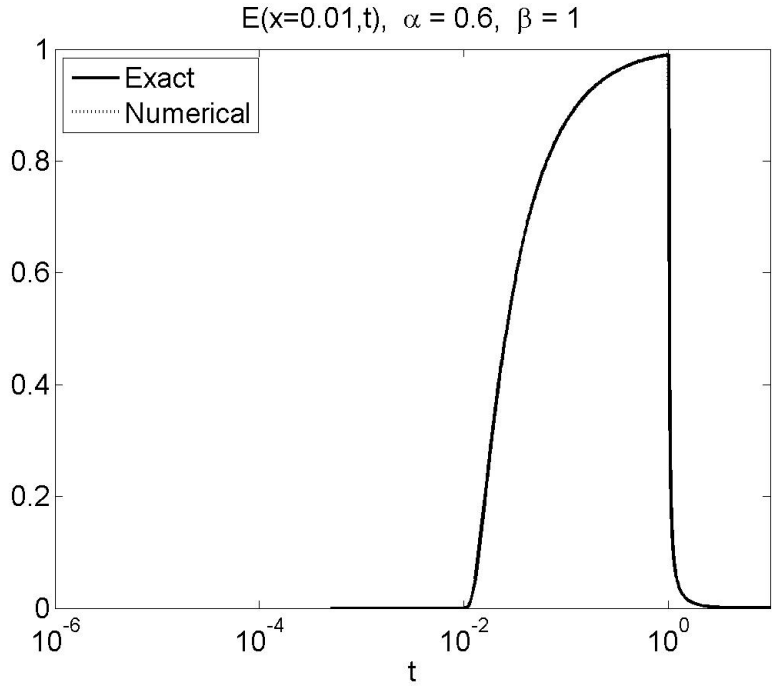

Figure 4.5 Validation of Cole-Cole model for short depth.

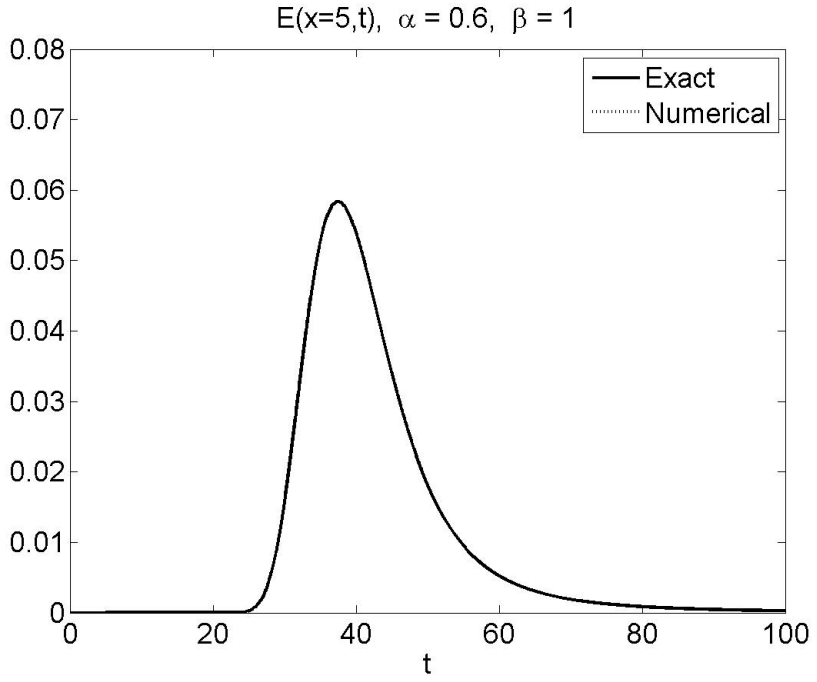

Figure 4.6 Validation of Cole-Cole model for large depth.

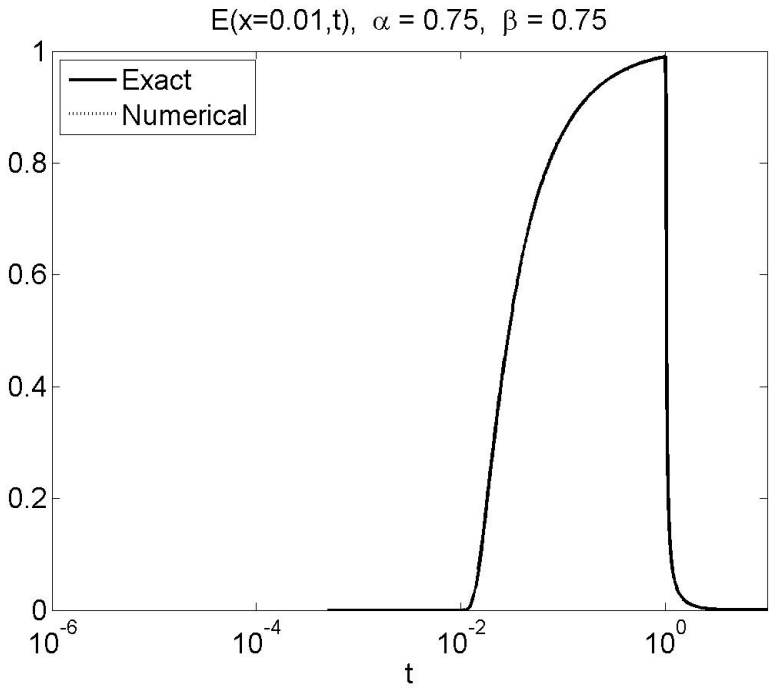

Figure 4.7 Validation of the Havriliak-Negami model at short depth. The program requires no augmentation to run the C-C and H-N models.

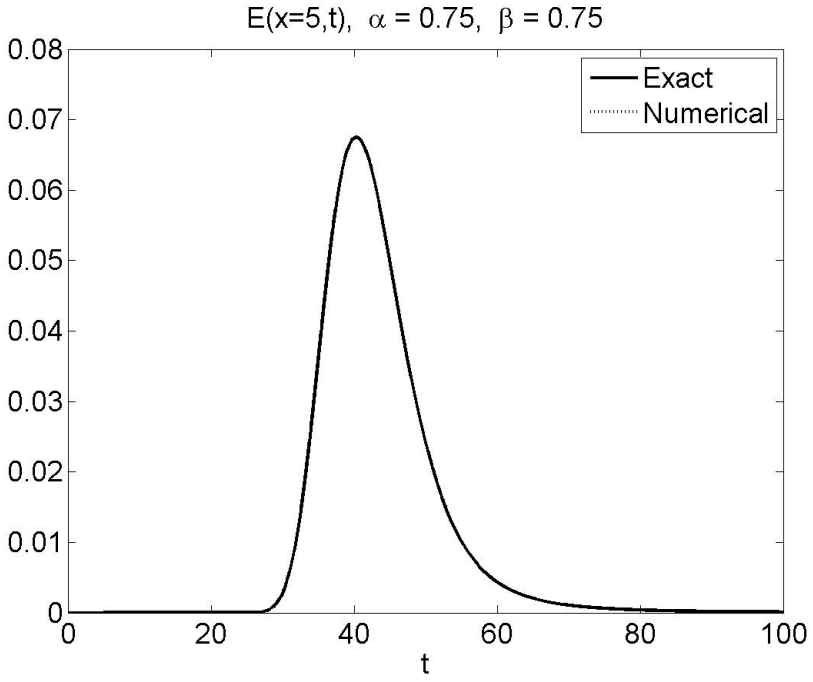

Figure 4.8 Validation of the Havriliak-Negami model at large depth. The program requires no augmentation to run the C-C and H-N models.

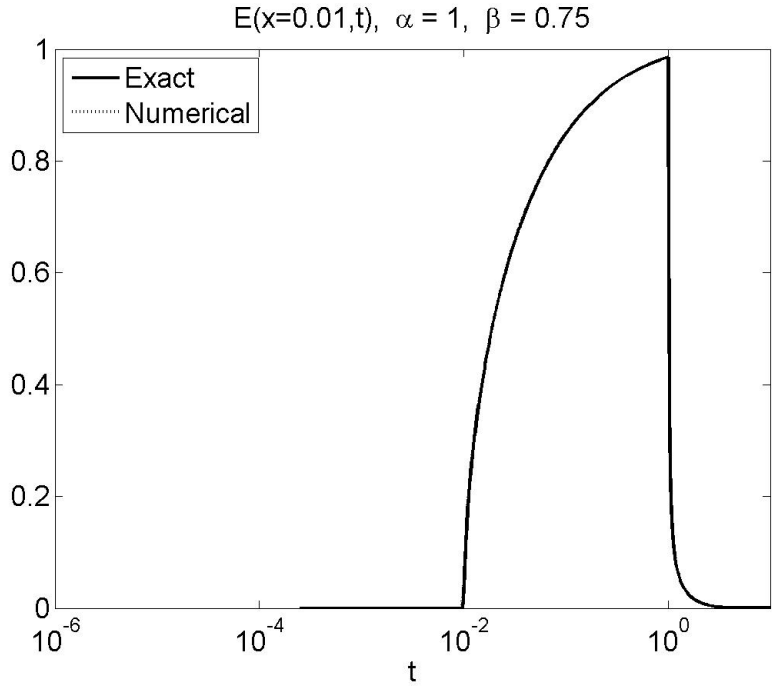

Figure 4.9 Validation of the Cole-Davidson program for short depth.

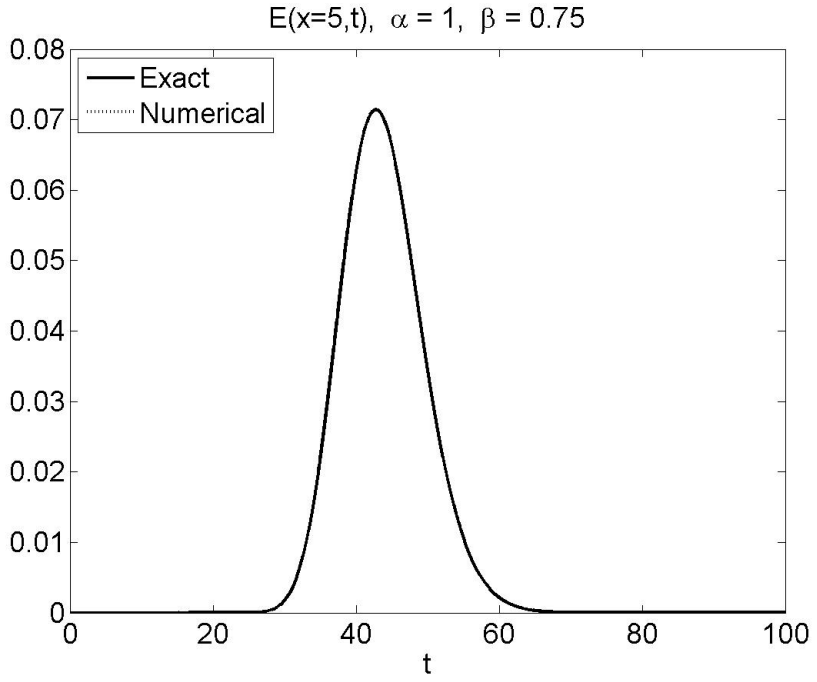

Figure 4.10 Validation of the Cole-Davidson program for large depths.

The solution will exhibit characteristically different behavior at short and large depths away from the left boundary, $x = 0$, of the dielectric half-space; thus we show a validation for each of these spatial regions. The C-C model is validated in Figures 4.5 and 4.6, and the H-N model in Figures 4.7 and 4.8. In both instances the numerical solution is computed with the same code; the only change is in the parameters α and β. This demonstrates that our method can treat both of these dielectric models. When computing the C-D model, we have to change the quadrature accordingly as shown in (4.7); this augmented scheme is validated in Figures 4.9 and 4.10. In all three cases, the agreement is very good.

We next consider the L_2 error, computed over the computational time interval $T = 300$, with respect to the exact solution as computed in Chapter 2, of our model problem. The convergence of this error is plotted in Figures 4.11-4.13, for several values of $h = \Delta t/\tau$, and $\alpha = \beta = 0.75$, at a range of depth spanning four orders of magnitude. The values of these curves are plotted on a log-log scale, and show second order accuracy. The observed convergence rate holds for the C-C and C-D models as well.

In section 4.2, it was shown that for short times, the behavior of the susceptibility was determined as $\chi \sim t^{\alpha\beta-1}$, $t \to 0^+$. This indicates that for different values of α and β we would expect similar short time behavior in the electric field if the product of these is close; this is demonstrated in Figures 4.14-4.17, for the long and short duration pulses, respectively. Despite the fact that left plots depict a C-C medium, and the right an H-N medium, the electric field is nearly indistinguishable. The waveforms shown here capture the transient behavior of the solution, which occurs in the so called time-domain skin-depth [29]. The initial discontinuities rapidly vanish, which can be confirmed with an asymptotic investigation of the electric field [30]. The long pulse will remain constant for a longer duration, and so its spectrum will contain larger amplitudes in the high-frequency regime. Consequently, the larger

frequencies persist longer into the skin-depth for the longer pulse (note the scale of the t-axis). The short pulse more closely approximates a delta function, and

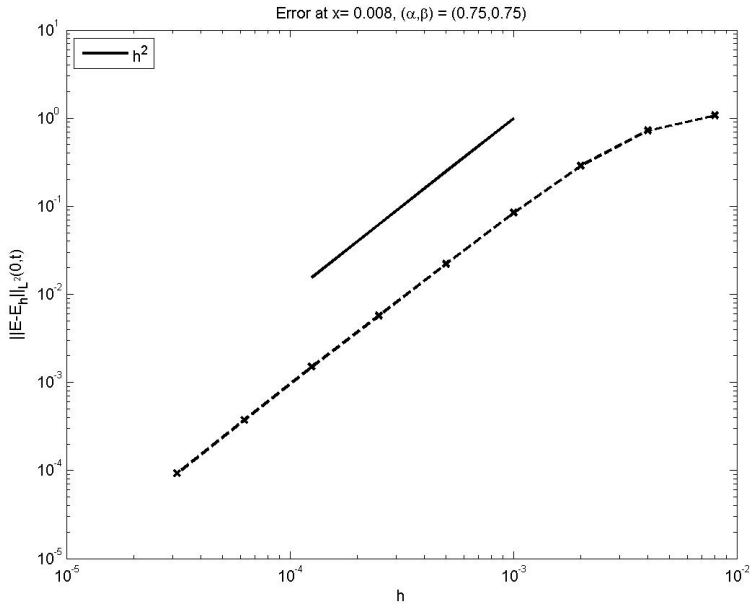

Figure 4.11 L^2-convergence of the electric field at $x = 0.008 c_\infty \tau$.

so is a good approximation to the impulse response of the material. In this region, the waveforms will travel at the infinite frequency speed, $c_\infty = c_0/\sqrt{\epsilon_\infty}$; past the skin-depth we see a transition to the static (zero-frequency) speed $c_s = c_0/\sqrt{\epsilon_s}$, as shown in Figure 4.18. While this transition is sudden and clear in a Debye type medium, the transition is smooth in a general H-N, C-C or C-D medium due to the continuous distribution of relaxation times. Beyond this transition region, the susceptibility will be approximated well by $\chi \sim t^{-\alpha-1}$, $t \to \infty$. This behavior is shown in Figures 4.19 and 4.20 for the same solutions as shown in Figures 4.14, 4.15, 4.16 and 4.17, observed at a deeper spatial location. Now the transient behavior has subsided, and the solution will be a material response, determined by the dielectric parameters; thus, independent of the original signal. The amplitude and shape of the electric field are very close between the short and long pulses, despite the disparate starting amplitudes. This is not terribly surprising, since the spectra of the two

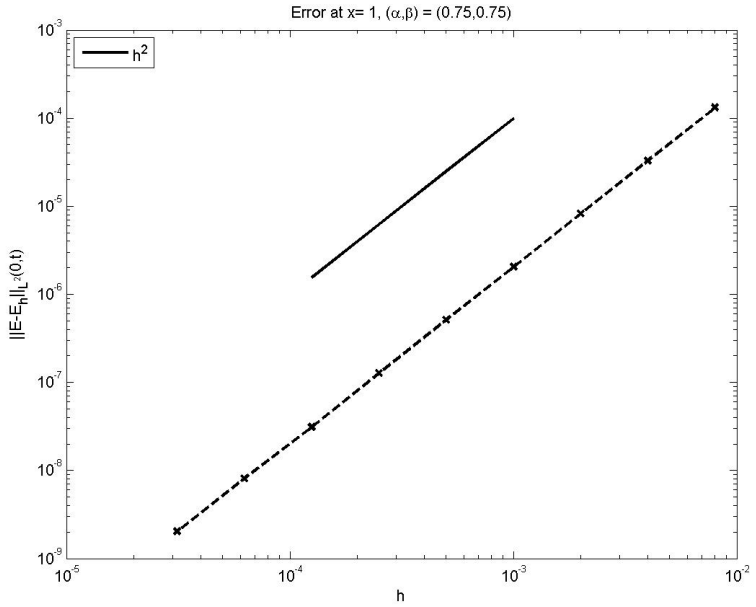

Figure 4.12 L^2-convergence of the electric field at $x = c_\infty \tau$.

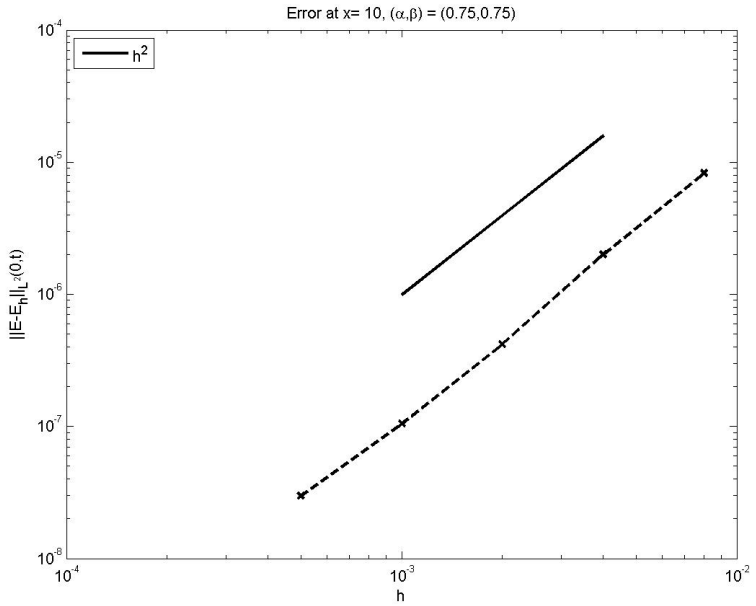

Figure 4.13 L^2-convergence of the electric field at $x = 10c_\infty \tau$.

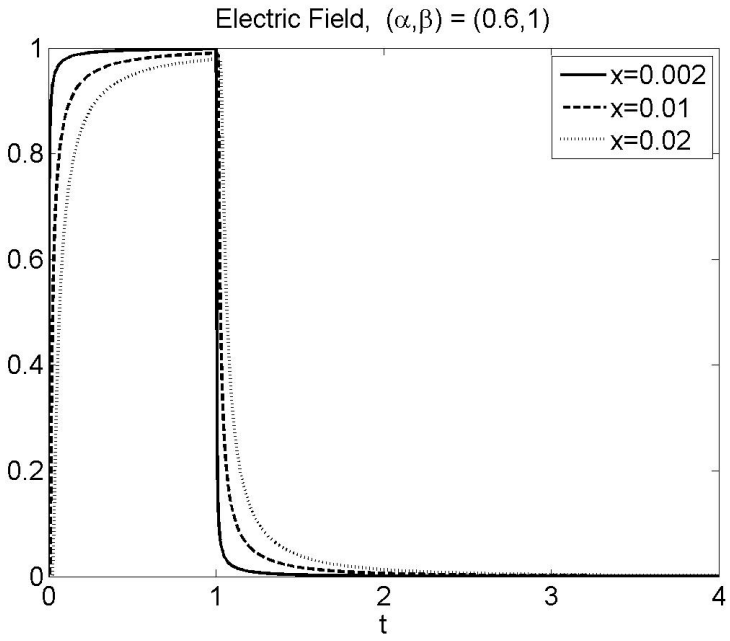

Figure 4.14 A typical short-depth electric field for a Cole-Cole medium. The transient behavior is very much the same as an H-N medium with the same product $\alpha\beta$. The initial pulse duration was $t_d = \tau = 1$, with amplitude 1.

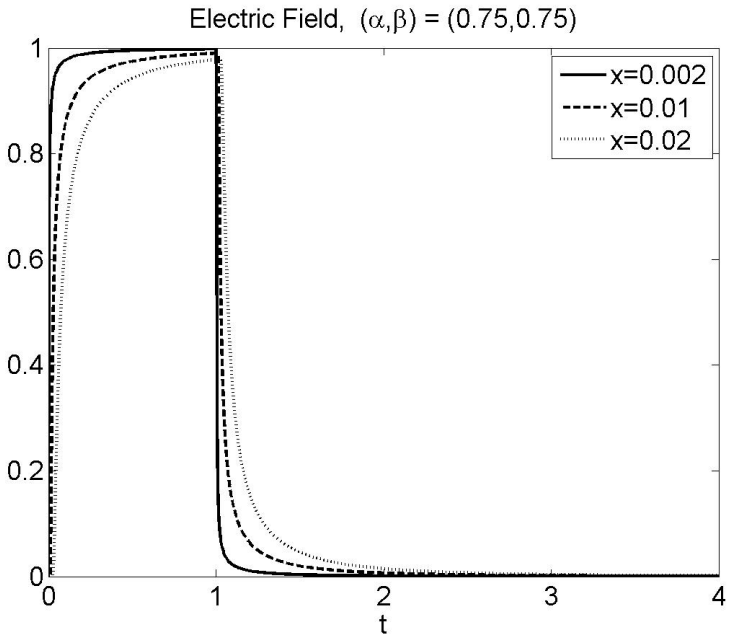

Figure 4.15 A typical short-depth electric field for a Havriliak-Negami medium. The transient behavior is very much the same as a C-C medium with the same product $\alpha\beta$. The initial pulse duration was $t_d = \tau = 1$, with amplitude 1.

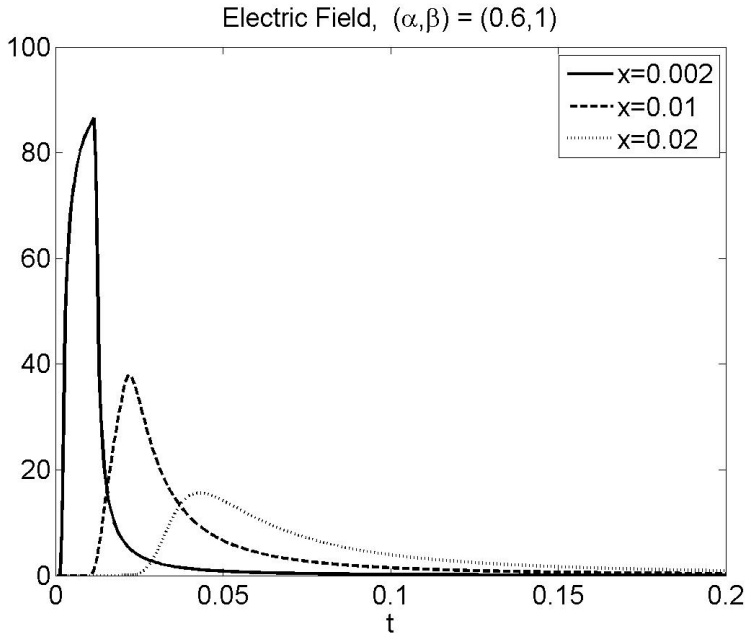

Figure 4.16 For the same C-C medium, the short-depth plots are shown with a pulse that is of duration $t_d = \tau/100$ and amplitude 100.

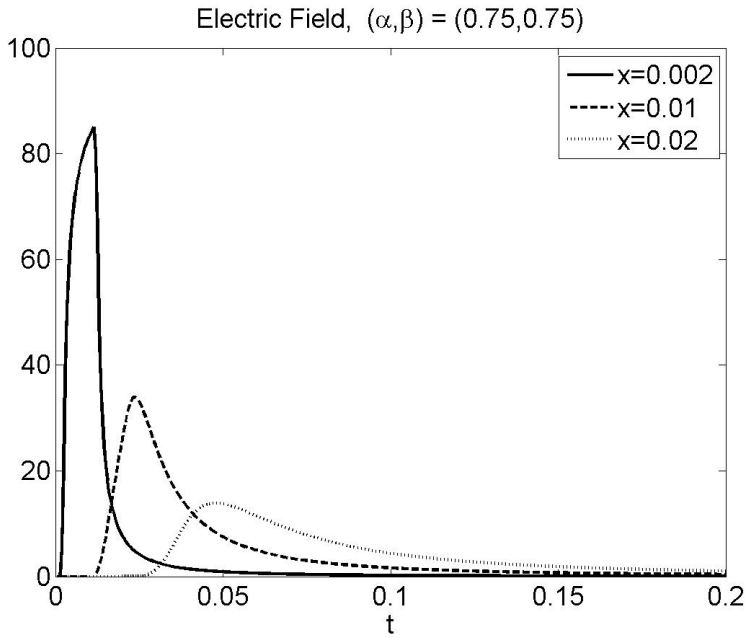

Figure 4.17 For the same H-N medium, the short-depth plots are shown with a pulse that is of duration $t_d = \tau/100$ and amplitude 100.

signals will have very similar low-frequency content. We can also see the effects of α and β as shaping parameters on these characteristic waveforms, which is illustrated in Figures 4.19 and 4.20 by the large depth behavior of the H-N and C-C fields. When α is increased, the asymmetry and tail of the waveform is increased; decreasing β narrows the waveform, and raises the peak slightly.

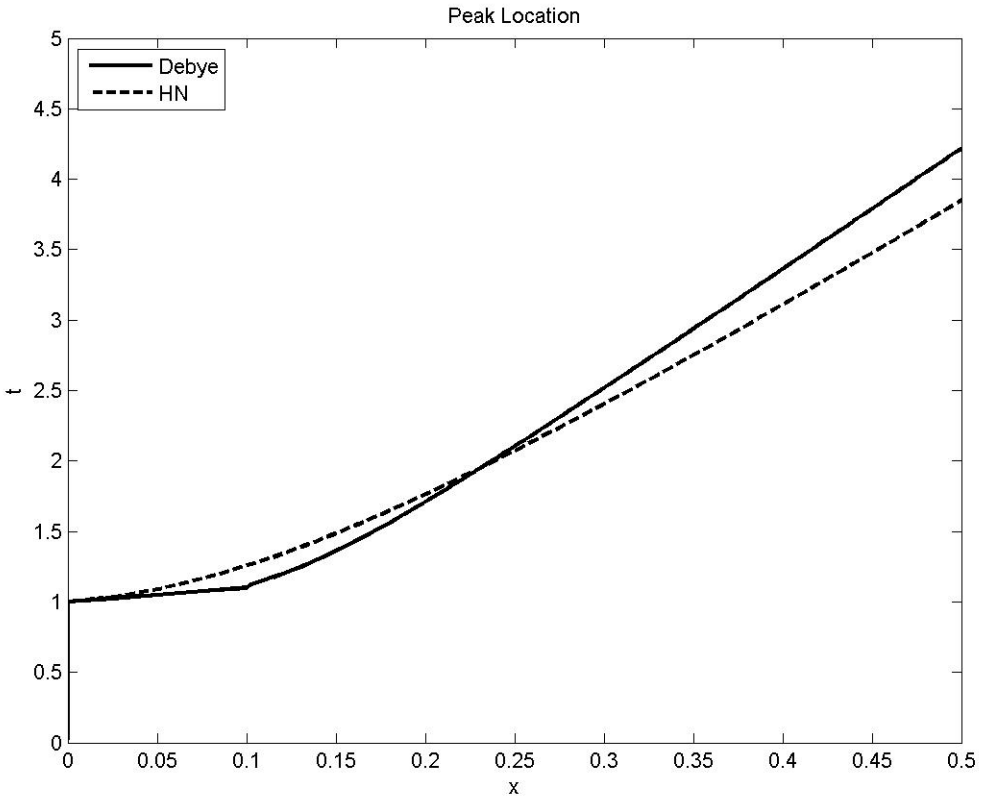

Figure 4.18 The (x, t) location of the peak electric field value is traced for the Debye and H-N models. All modeling parameters are the same, except $\alpha = \beta = 0.75$ in the H-N model. The Debye model undergoes a sudden transition from the ray defined by c_∞ to that of c_s, whereas the transition is smooth in the H-N case.

4.5 Conclusion

In this chapter we have developed a novel method to construct time-domain simulations for the family of anomalously dispersive dielectrics represented by the Havriliak-

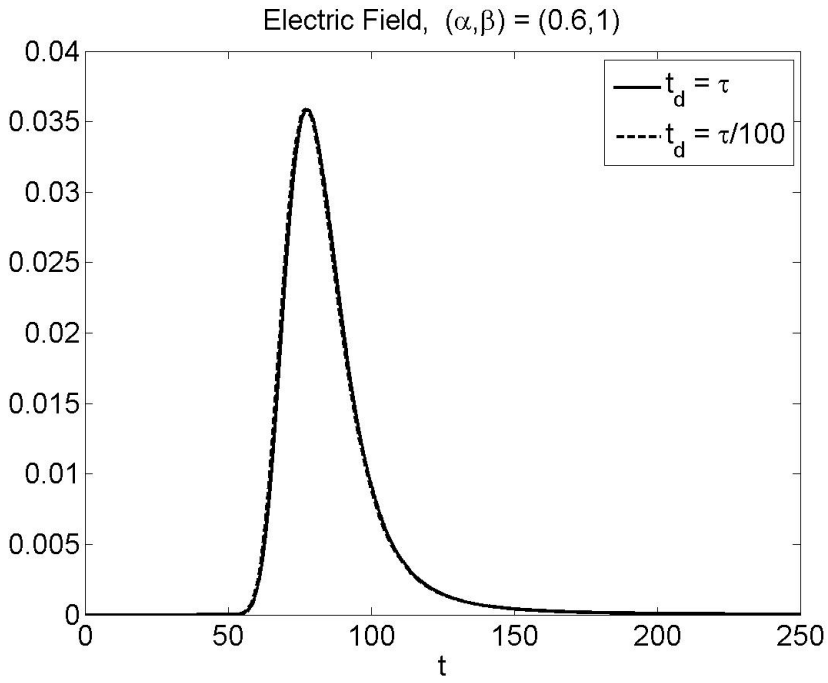

Figure 4.19 A typical large-depth electric field for a Cole-Cole medium. The short and long duration pulses have nearly the same amplitudes at this point in the medium, despite initially differing in amplitude by two orders of magnitude.

Negami induced polarization model. Specifically we have used the FD-TD method, and an efficient approximation of the induced polarization convolution using a sum of exponentials arrived at by applying generalized Gaussian quadratures. The convolution kernel is constructed with a preset level of accuracy that is uniform over a predetermined computational window, and can be set below the expected truncation error, so that the overall error is second order as in the FD-TD scheme. We explicitly addressed the C-C, C-D and general H-N cases when constructing these approximations, and note here that the Debye model can be incorporated as well, simply by omitting the local portion of the approximation across the first time step (which is unnecessary), and updating the history portion only at the single exponential node $y = 1$; this is equivalent to implementing the Debye model using exponential time differencing, or evaluating the recurrence relation as shown in section 4.2. We have also shown using Von Neumann analysis that the overall resulting numerical scheme

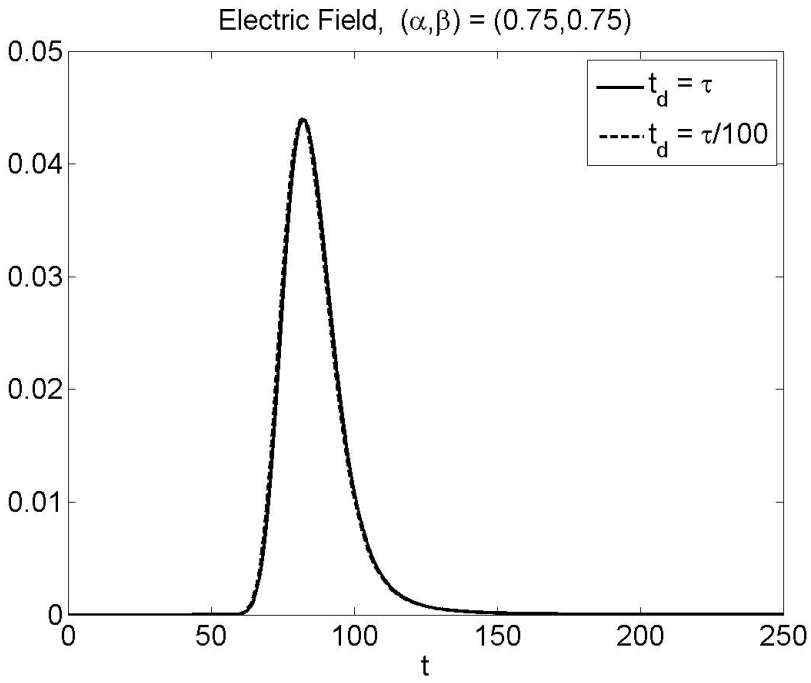

Figure 4.20 A typical large-depth electric field for a Havriliak-Negami medium. The short and long duration pulses have nearly the same amplitudes at this point in the medium, despite initially differing in amplitude by two orders of magnitude.

is stable with no additional restriction placed on the time step other than the typical CFL condition. Numerical simulations confirm the stability and accuracy results, and we validate the numerical solutions via alternate representations of the exact solutions using Laplace transforms.

CHAPTER 5

FUTURE WORK

There are several directions that could be taken in continuing this work. One such direction would be the extension of the H-N model to numerical implementations of higher order; i.e., a fourth-order numerical scheme. Since the polarization law (3.4) is given by a temporal operator, we can again suppress the spatial dependence. The electric field for a typical fourth-order numerical implementation of Maxwell's equations [40] is given by

$$\epsilon_\infty E_m^{n+1} + P_m^{n+1} = \epsilon_\infty E_m^n + P_m^n + \Delta t \left(1 + \frac{\Delta t^2}{24}\delta_t^2\right) \Lambda_x H_m^{n+1/2} \tag{5.1}$$

where we are again computing the TEM propagation as shown in (4.2), and the numerical operators are given as

$$\delta_t^2 H_m^{n+1/2} = \frac{1}{\Delta t^2}\left(H_m^{n+3/2} - 2H_m^{n+1/2} + H_m^{n-1/2}\right), \tag{5.2}$$

$$\Lambda_x H_m^{n+1/2} = \frac{1}{24\Delta x}\left(H_{m-3/2}^{n+1/2} - 27H_{m-1/2}^{n+1/2} + 27H_{m+1/2}^{n+1/2} - H_{m-3/2}^{n+1/2}\right). \tag{5.3}$$

A similar expression will hold for the magnetic field equation, and generalization to higher dimensions follows accordingly. In order to take advantage of the benefits of the higher order accuracy, the polarization equation must also be augmented. This will require treatment of both the local and the history approximation. The former of these follows by replacing the polarization in (3.4) with a cubic polynomial through the points E^n, E^{n-1}, E^{n-2} and E^{n-3}

$$\begin{aligned} E(t_n - u) = E^n &- \frac{u}{6h}(11E^n - 18E^{n-1} + 9E^{n-2} - 2E^{n-3}) \\ &+ \frac{u^2}{6h^2}(6E^n - 15E^{n-1} + 12E^{n-2} - 3E^{n-3}) \\ &- \frac{u^3}{6h^3}(E^n - 3E^{n-1} + 3E^{n-2} - E^{n-3}) + O(h^4) \end{aligned} \tag{5.4}$$

which is valid for $0 < u < 3h$. Substitution into equation (3.4) and integration will yield a multi-step scheme of the form

$$\begin{aligned} P_{Loc}^n = & AE^n - \frac{B}{6}(11E^n - 18E^{n-1} + 9E^{n-2} - 2E^{n-3}) \\ & + \frac{C}{6}(6E^n - 15E^{n-1} + 12E^{n-2} - 3E^{n-3}) \\ & - \frac{D}{6}(E^n - 3E^{n-1} + 3E^{n-2} - E^{n-3}) + O(h^4) \end{aligned} \tag{5.5}$$

with

$$\begin{aligned} A &= \int_0^{3h} \chi(u)du, \\ B &= \int_0^{3h} \frac{u}{h}\chi(u)du, \\ C &= \int_0^{3h} \left(\frac{u}{h}\right)^2 \chi(u)du, \\ D &= \int_0^{3h} \left(\frac{u}{h}\right)^3 \chi(u)du. \end{aligned} \tag{5.6}$$

Similar treatment must be given to the history contribution, which follows from the same application to the integrals

$$\int_{3h}^{nh} e^{-y_j u} E(t_{n+1} - u)du, j = 1, 2 \ldots N. \tag{5.7}$$

The resulting schemes would be multi-step methods, and as such the stability would have to be investigated. Additionally, a Runge-Kutta scheme could be used to approximate the polarization law (3.4).

Another direction that can be pursued is to use the asymptotic investigation of Chapter 2 to obtain parameters for the H-N media from scattering data; i.e., to solve the inverse problem. In [30], it was shown in the case of the Debye model that for large depths, the electric field satisfies an advection-diffusion equation with the zero-frequency speed $c_s = 1/\sqrt{\mu_0\epsilon_0\epsilon_s}$. This results in a symmetric response, whose peak is located along the subcharacteristic ray $t = x/c_s$. But in the Cole-Cole model

[30], the peak was found not to coincide with this ray; rather, it is the mean electric field that does. When $\alpha \to 1$, the peak and mean electric fields coalesce. More importantly, we can compute the time at which the mean electric field occurs using the mean value theorem,

$$\bar{t}(x) = \frac{\int_0^\infty t' E(x,t') dt'}{\int_0^\infty E(x,t') dt'}. \tag{5.8}$$

Upon constructing this quantity, we find that $\bar{t}$ is a linear function of x, with slope $1/c_s$. The intercept can be computed by setting $x = 0$, and doing so provides an alternate expression in terms of the incident pulse

$$\bar{t}(x) = \bar{t}(0) + \frac{x}{c_s} = \frac{\int_0^\infty t' f(t') dt'}{\int_0^\infty f(t') dt'} + \frac{x}{c_s}. \tag{5.9}$$

Note that if we have an experimentally obtained time trace that is recorded at a known x location, we can approximate $\bar{t}$. By setting the two expressions equal, we can then isolate the subcharacteristic speed and in turn obtain ϵ_s

$$\epsilon_s = \frac{(\bar{t}(x) - \bar{t}(0))^2}{x^2 \epsilon_0 \mu_0}. \tag{5.10}$$

This will provide a straightforward manner to compute this model parameter, without

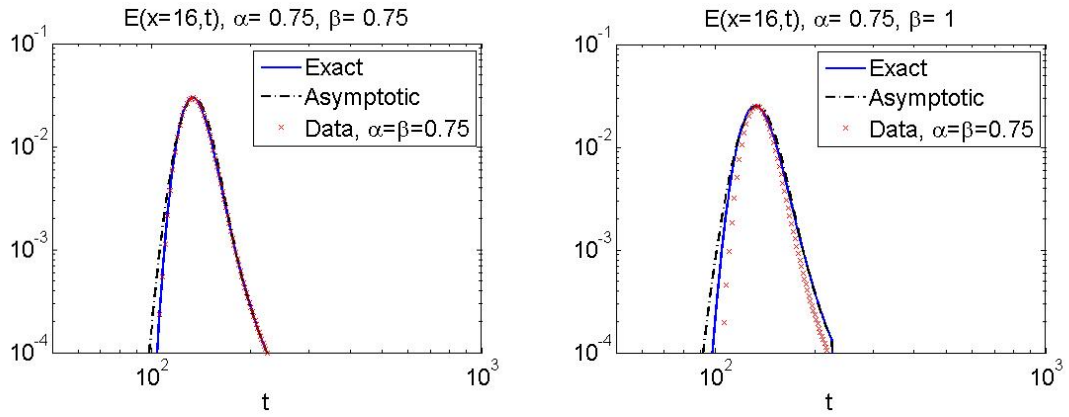

Figure 5.1 Log-log plots comparing large-depth asymptotic approximations of a step-response to a numerically obtained solution, with $\alpha = \beta = 0.75$.

fitting. At this time we are unaware of any analogous procedure to determine the

parameters ϵ_∞, and τ; however the late asymptotic response may be used to determine H-N parameters (α, β). In Figure 5.1, the numerical solution of the electric field with $\alpha = \beta = 0.75$ represents a data set, and is plotted on a log-log scale. The first plot (left panel) shows the fit when the correct parameters are chosen, and the portion of the curves to the right of the peaks match. When the correct value of α is found, but β is not correct, the curves will be parallel in this region, as in right panel. In both panels of Figure 5.2, the value of α is incorrect, and we can clearly see that the curves are not parallel as $t \to \infty$. This is true even in the lower left panel, where β is correct. Thus, we can only proceed with determining β after finding α.

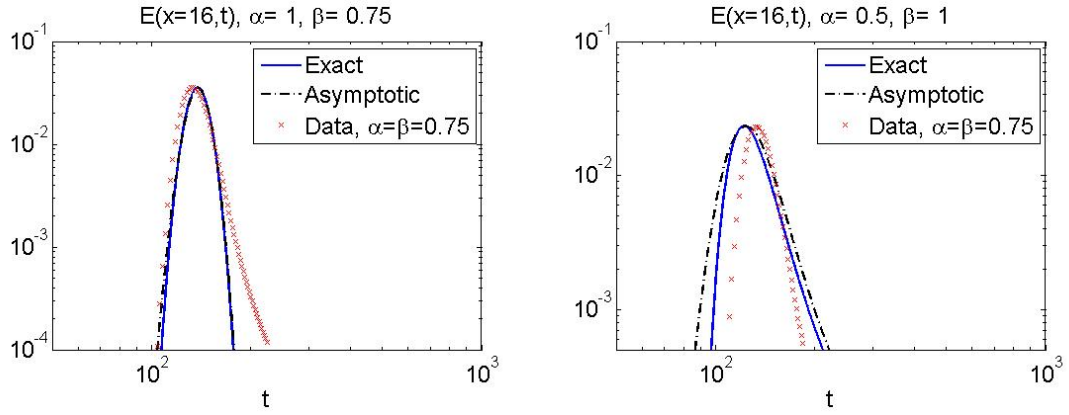

Figure 5.2 Log-log plots comparing large-depth asymptotic approximations of a step-response to a numerically obtained solution, with $\alpha = \beta = 0.75$.

REFERENCES

[1] A. Alegria, L. Goitiandia, I. Telleria, and J. Colmenero. α-relaxation in the glass-transition range of amorphous polymers. 2. influence of physical aging on the dielectric relaxation. *Macromolecules*, (30):3881–3887, 1997.

[2] G. Beylkin and L. Monzón. On approximation of functions by exponential sums. *Appl. Comput. Harmon. Anal.*, 19(1):17–48, 2005.

[3] G. Beylkin and L. Monzón. Approximation by exponential sums revisited. *Appl. Comput. Harmon. Anal.*, 28(2):131–149, 2010.

[4] B. Bidegaray-Fesquet. Von-neumann stability analysis of fdtd methods in complex media. in 7th International Symposium on Electric and Magnetic Fields (EMF 2006), Aussois, 2006.

[5] R. Buchner, S. G. Capewell, G. Hefter, and P. M. May. Ion-pair and solvent relaxation processes in aqueous na2so4 solutions. *J. Phys. Chem. B*, 103(7):1185–1192, 1999.

[6] K. S. Cole and R. H. Cole. Dispersion and absorption in dielectrics i. alternating current characteristics. *J. Chem. Phys.*, 9:341–52, 1941.

[7] J. Cooper, B. Marx, J. Buhl, and V. Hombach. Determination of safety distance limits for a human near a cellular base station antenna, adopting the ieee standard or icnirp guidelines. *Bioelectromagnetics*, 23(6):429–443, 2000.

[8] D. W. Davidson and R. H. Cole. Dielectric relaxation in glycerol, propylene glycol, and n-propanol. *J. Chem. Phys.*, 19:1484–1490, 1951.

[9] P. Debye. *Polar Molecules*. Dover, New York, 1929.

[10] K. Diethelm. Analysis of fractional differential equations. *J. Math. Anal. Appl.*, 265(2):229–248, 2002.

[11] K. Diethelm. An investigation of some nonclassical methods for the numerical approximation of caputo-type fractional derivatives. *Numer. Algor.*, 47(4):361–390, 2008.

[12] C. Gabriel and S. Gabriel. Compilation of the dielectric properties of body tissues at rf and microwave frequencies. *U.S.A.F Armstrong Lab., Brooks AFB, TX, Technical Rep. AL/OE-TR-1996-0037*, 1996.

[13] A. Garcia-Bernabe, R. Diaz Calleja, M.J. Sanchis, A. del Campo, A. Bello, and E. Perez. Amorphous-smectic glassy main chain lcps. ii. dielectric study of the glass transition. *Polymer*, (45):1533–1543, 2004.

[14] W. Gautschi. Quadrature formulae on half-infinite intervals. *BIT*, 31(3):438–446, 1991.

[15] L. Greengard and P. Lin. Spectral approximation of the free-space heat kernel. *Appl. Comput. Harmon. Anal.*, 9:83–97, 2000.

[16] A. Hanyga and J.-F. Lu. Wave field simulation for heterogeneous transversely isotropic porous media with the jkd dynamic permeability. *Comput. Mech.*, 36:196–208, 2005.

[17] S. Havriliak and S. Negami. A complex plane representation of dielectric and mechanical relaxation processes in some polymers. *J. Polym. Sci.*, 8(4):161, 1967.

[18] S. J. Huang. Exponential time differencing algorithm for debye medium in fdtd. *Int. J. Infrared Milli.*, 28(11):1025–1031, 2007.

[19] T. I. Jeon and D. Grischkowsky. Observation of a cole-davidson type complex conductivity in the limit of very low carrier densities in doped silicon. *Appl. Phys. Lett.*, 72(18):2259–2261, 1998.

[20] J. Jiang and L. Greengard. Fast evaluation of nonreflecting boundary conditions for the schrdinger equation in one dimension. *Comput. Math. Appl.*, 47:955–966, 2004.

[21] Y. P. Kalmykov, W. T. Coffey, D. S. F. Crothers, and S. V. Titov. Microscopic models for dielectric relaxation in disordered systems. *Phys. Rev. E*, 70:1–11, 2004.

[22] D. F. Kelley, T. J. Destan, and R. J. Luebbers. Debye function expansions of complex permittivity using a hybrid particle swarm-least squares optimization. *IEEE Trans. Ant. Prop.*, 55(7):1999–2005, 2007.

[23] T. Kim, J. Kim, and J. Pack. Dispersive effect of uwb pulse on human head. Electromagnetic Compatibility, 2007. EMC Zurich 2007. 18th International Zurich Symposium on, 2007.

[24] J. T. Kindt and C. A. Schmuttenmaer. Far-infrared dielectric properties of polar liquids probed by femtosecond terahertz pulse spectroscopy. *J. Phys. Chem.*, 100(24):10373–10379, 1996.

[25] J. Li. A fast time stepping method for evaluating fractional integrals. *SIAM J. Sci. Comput.*, 31(6):4696–4714, 2010.

[26] R. Luebbers, F. P. Hunsberger, K. S. Kunz, R. B. Standler, and M. Schneider. A frequency-dependent finite-difference time-domain formulation for dispersive materials. *IEEE Trans. on Electromagn. Comp.*, 32:222–227, 1990.

[27] J. Ma, V. Rokhlin, and S. Wandzura. Generalized gaussian quadrature rules for systems of arbitrary functions. *SIAM J. Numer. Anal.*, 33(3):971–996, 1996.

[28] P. G. Petropoulos. Stability and phase error analysis of fd-td in dispersive dielectrics. *IEEE Trans. Ant. Prop.*, 42(1):62–69, 1994.

[29] P. G. Petropoulos. The wave hierarchy for propagation in relaxing dielectrics. *Wave Motion*, 21(3):253–262, 1995.

[30] P. G. Petropoulos. On the time-domain response of cole-cole dielectrics. *IEEE Trans. Ant. Prop.*, 53(11):3741–3746, 2005.

[31] I. T. Rekanos and T. G. Papadopoulos. An auxiliary differential equation method for fdtd modeling of wave propagation in cole-cole dispersive media. *IEEE Trans. Ant. Prop.*, 58(11):3666–3674, 2010.

[32] T. Repo and S. Pulli. Application of impedance spectroscopy for selecting frost hardy varieties of english ryegrass. *Ann. Bot.*, (78):605–609, 1996.

[33] T. M. Roberts and P. G. Petropoulos. Asymptotics and energy estimates for electromagnetic pulses in dispersive media. *J. Opt. Soc. Am. A*, 13(6):1204–1217, 1996.

[34] J. C. Strikwerda. *Finite Difference Schemes and Partial Differential Equations*. Chapman and Hall, 1989.

[35] A. Taflove. *Computational Electrodynamics: The Finite-Difference Time-Domain Method*. Artech House, Norwood, MA, 1995.

[36] M. Tofighi. Fdtd modeling of biological tissues cole-cole dispersion for 0.5-30 ghz using relaxation time distribution samples-novel and improved implementations. *IEEE Trans. Microw. Theory*, 57(10):2588–2596, 2009.

[37] F. Torres, P. Vaudon, and B. Jecko. Application of fractional derivatives to the fdtd modeling of pulse propagation in a cole-cole dispersive medium. *Microw. Opt. Tech. Lett.*, 13(5):297–300, 1996.

[38] J. A. C. Weideman and L. N. Trefethen. Parabolic and hyperbolic contours for computing the bromwich integral. *Math. Comput.*, 76(259), 2007.

[39] J. H. Wilkinson. The evaluation of the zeros of ill-conditioned polynomials. *Numerische Mathematik*, 1:150–166, 1959.

[40] Z. Xie, C. Chan, and B. Zhang. An explicit fourth-order staggered finite-difference time-domain method for maxwell's equations, 2002.

[41] N. Yarvin and V. Rohklin. Generalized gaussian quadrature and singular value decompositions of integral operators. *Siam J. Sci. Comput.*, 20(2):699–718, 1998.

[42] L. Yuan and O. P. Agrawal. A numerical scheme for dynamic systems containing fractional derivatives. *J. Vib. Acoust.*, 124:321324, 2002.

[43] R. Zorn. Applicability of distribution functions for the havriliak negami spectral function. *J. Polym. Sci. Pol. Phys.*, 37(10):1043–1044, 1999.